Aalto University
School of Science

Matti Partanen

QUANTUM-LIMITED HEAT CONDUCTION OVER MACROSCOPIC DISTANCES

Master's thesis submitted in partial fulfillment of the requirements for the degree of Master of Science in Technology in the Degree Programme in Engineering Physics and Mathematics.

Espoo, November 18, 2014

Supervisor: Prof. Matti Kaivola

Instructor: Dr. Mikko Möttönen

Aalto University

AALTO UNIVERSITY SCHOOL OF SCIENCE P.O. BOX 11000, FI-00076 AALTO http://www.aalto.fi	ABSTRACT OF THE MASTER'S THESIS

Author: Matti Partanen

Title: Quantum-limited heat conduction over macroscopic distances

Degree programme: Engineering Physics and Mathematics

Major subject: Engineering Physics

Chair (code): Tfy-125

Supervisor: Prof. Matti Kaivola

Instructor: Dr. Mikko Möttönen

Abstract:

Quantum mechanics sets a fundamental upper limit for single-channel heat conductance, known as the quantum of thermal conductance. In this thesis, the quantum of thermal conductance is experimentally investigated at macroscopic length scales for the first time. The studied system consists of two normal-metal islands connected by a superconducting transmission line.

The methods studied in this thesis can potentially be applied in the emerging field of quantum nanoelectronics as they provide a solution for remote temperature reduction of critical components. Photonic heat conduction is perhaps the only feasible option for efficiently transferring heat to a distant cold reservoir, which is vital for the operation of many quantum devices of practical interest.

We observe the photonic heat conduction to be the dominating heat conduction mechanism between the normal-metal islands. The experimental results support the theoretical model according to which the photonic heat conduction is close to the theoretical upper limit. The longest distance, over which the photonic heat conduction is observed in this thesis, is one meter, long enough for all current applications in quantum nanoelectronics.

Date: 18.11.2014	Language: English	Number of pages: 6 + 96

Keywords: heat conductivity, quantum of thermal conductance, NIS junction, microwave resonator

Aalto University

AALTO-YLIOPISTO PERUSTIETEIDEN KORKEAKOULU PL 11000, 00076 AALTO http://www.aalto.fi	DIPLOMITYÖN TIIVISTELMÄ

Tekijä: Matti Partanen

Työn nimi: Kvanttimekaniikan rajoittama lämmönjohtavuus makroskooppisessa mittakaavassa

Tutkinto-ohjelma: Teknillinen fysiikka ja matematiikka

Pääaine: Teknillinen fysiikka

Opetusyksikön koodi: Tfy-125

Valvoja: Prof. Matti Kaivola

Ohjaaja: TkT Mikko Möttönen

Tiivistelmä:

Kvanttimekaniikan avulla voidaan johtaa lämmönjohtavuuskvanttina tunnettu yläraja yksittäisen kanavan lämmönjohtavuudelle. Tässä diplomityössä tutkitaan lämmönjohtavuuskvanttia kokeellisesti ensimmäistä kertaa makroskooppisessa mittakaavassa. Tutkittava systeemi koostuu kahdesta suprajohtavalla siirtolinjalla yhdistetystä normaalimetallisaarekkeesta.

Tässä työssä tutkittuja menetelmiä voidaan mahdollisesti soveltaa uudella kvanttinanoelektroniikan alalla, sillä ne mahdollistavat kriittisten komponenttien jäähdyttämisen etäältä. Fotonien aiheuttama lämmönjohtavuus on kenties ainoa käypä vaihtoehto tehokkaaseen kylmäsäiliöön tapahtuvaan lämmönsiirtoon, joka on välttämätöntä monien kvanttimekaanisten laitteiden toiminnan kannalta.

Työssä havaitaan fotonien aiheuttaman lämmönjohtavuuden olevan hallitseva lämmönsiirtymismekanismi normaalimetallisaarekkeiden välillä. Kokeelliset tulokset tukevat teoreettista mallia, jonka mukaan fotonien aiheuttama lämmönsiirto on lähellä teoreettista ylärajaa. Pisin etäisyys, jonka yli fotonien aiheuttamaa lämmönsiirtoa havaitaan tässä työssä, on yksi metri, joka riittää kaikkiin nykyisiin sovelluksiin kvanttinanoelektroniikan alalla.

Päivämäärä: 18.11.2014	Kieli: englanti	Sivumäärä: 6 + 96

Avainsanat: lämmönjohtavuus, lämmönjohtavuuskvantti, NIS-liitos, mikroaaltovärähtelijä

Preface

The work for this master's thesis was carried out in the Quantum Computing and Devices research group in the Department of Applied Physics of Aalto University. Firstly, I would like to thank my supervisor Prof. Matti Kaivola for supervising this thesis. In addition, I would like to express my gratitude to my instructor Dr. Mikko Möttönen for giving me the opportunity to work on this topic and for his guidance throughout this thesis.

This thesis would not have been possible without the help of the other current and previous members of the research group. Especially, I would like to thank the other experimentalists Dr. Kuan Yen Tan, Dr. Russell Lake, M.Sc. Joonas Govenius, and M.Sc. Tuomo Tanttu for the cooperation and help with the device fabrication and measurements as well as for the insightful conversations. In addition, the other people who have contributed to the experimental part of this work in the cleanroom deserve to be thanked.

Finally, I would like to thank my family and friends most warmly for all their support.

Espoo, November 18, 2014

Matti Partanen

Contents

1 Introduction

According to the laws of thermodynamics, two objects with different temperatures exchange net heat when they are in thermal contact until a thermal equilibrium is reached. This is a very intuitive result which we often encounter in case of macroscopic objects but it is also valid near the microscopic scale where quantum phenomena may dominate. In fact, there is an upper bound for the heat conduction given by quantum mechanics [1]. The upper bound is valid for a single channel which corresponds to a degree of freedom such as a polarisation state of electromagnetic radiation [1]. The total heat conduction between the objects occurs through separate channels. In order to observe the upper limit, it is beneficial to consider systems with reduced dimensions at low temperatures, thus having very few parallel channels. Quantum-limited heat conduction has previously been observed for phonons [2], electromagnetic heat transfer [3,4], and electrons [5]. The length scales were below 100 μm in these experiments performed at cryogenic temperatures. Nevertheless, it is possible to study single-channel heat conduction at the macroscopic scale.

The understanding of heat conduction mechanisms at low temperatures [6] is essential in order to operate superconducting quantum bits, qubits, in a quantum computer [7], which is an example of the promising applications in the field of quantum nanoelectronics [8]. A qubit can have a value of 0 or 1 such as a classical bit but, in addition, it can also be in a superposition state, i.e., in both 0 and 1 state at the same time. A quantum computer can, in principle, solve certain problems significantly faster than a conventional computer, and hence, the research related to them has been intense during the last two decades [9]. Perhaps the most famous problem which can be effectively solved by a quantum computer [10] is the factorisation of large numbers used in several contemporary data encryption protocols. The superconducting qubits provide one of the most promising architectures for a quantum computer [9, 11].

The qubit must be controllable but at the same its evolution needs to be coherent, which is obtainable by decoupling it from the environment [12]. In addition, the qubits need to interact during the computation, for instance, by means of circuit quantum electrodynamics (cQED) [12]. The control of the environment of the qubits can be realised by cooling and heating with photons transmitted over superconducting transmission lines [13] and, in addition, superconducting quantum interference devices (SQUIDs) can provide an in-situ tunable coupling strength, vital for quantum computation [14–16].

In this thesis, we experimentally investigate quantum-limited heat conduction over macroscopic distances. We study heat conduction between two normal-metal islands terminating a superconducting waveguide at different ends. In this scenario, the implemented length of the waveguide is 1 m at maximum, and the heat is dominantly carried by photons travelling in the waveguide in a broad frequency band. Superconducting microwave resonators provide also an opportunity to study single photon heat conduction, in which the heat is mostly carried by single photons in the lowest cavity mode [13]. Although the studied system may find applications in quantum computing as discussed above, the work in this thesis is also inspired by purely scientific interests.

The structure of this thesis is as follows: The theoretical background is presented in Chapter 2. Firstly, the quantum of thermal conductance is introduced. Secondly, the relevant theory for transmission lines is reviewed, and transmission coefficients are calculated. Thirdly, the photonic heat transfer as well as other heat transfer mechanisms present in superconducting mesoscopic devices are discussed. The chapter is concluded by presenting a thermal model for the studied system. The design and analysis methods of the experimental samples are presented in Chapter 3, including a coplanar waveguide (CPW) structure with coupling capacitances. Furthermore, we introduce the quality factor, which is a useful parameter characterising resonators. In addition, the methods for island temperature simulations are briefly discussed. Chapter 4 focuses on the fabrication methods of the samples. In addition, the measurement setups are presented for the experiments at temperatures of 4 K and below 1 K. Experimental results are presented in Chapter 5, and the results are compared with simulations. Both the control samples and the actual samples are studied. Finally, conclusions are drawn in Chapter 6.

2 Theoretical background

In this chapter, the theoretical background of the thesis is discussed. Firstly, the concept of the quantum of thermal conductance is reviewed. Secondly, transmission lines are analysed both classically and quantum mechanically. Here, the derivations follow rather closely Ref. [17] starting from general transmission lines. After the general cases, the photonic transmission coefficient for the experimentally studied system is presented. Thirdly, the properties of superconducting devices at the mesoscopic scale are discussed, and various heat conduction mechanisms are presented. The understanding of these mechanisms is essential in order to analyse the heat currents in the sample. Finally, we present a thermal model of the studied system.

2.1 Quantum of thermal conductance

Heat transfer through a single channel is fundamentally limited, which has been shown already three decades ago by J. B. Pendry [1]. He studied information, entropy, and energy flows through individual channels. A single channel corresponds to one of the variables specifying the flow, and it can be for example a polarisation state or a momentum state [1]. In this thesis we study a single channel of electromagnetic waves in a CPW transmission line.

The quantum of thermal conductance can be derived using Landauer theory according to which the heat conduction between two reservoirs may be written as [18]

$$\dot{Q} = \int_0^\infty \frac{dk}{2\pi} E(k)v(k)\{f_R[E(k), \mu_R, T_R] - f_L[E(k), \mu_L, T_L]\}, \tag{1}$$

where k is the wave vector of the heat-mediating particles, $E(k)$ is their energy, $v(k)$ their group velocity, and $f_{R/L}$ is the particle distribution function of the right and left reservoir. The temperature and the chemical potential of the right and left reservoir are denoted by $T_{R/L}$ and $\mu_{R/L}$, respectively. Here, we have assumed ballistic transport of particles through one channel. If the particles are fermions, the particles obey Fermi–Dirac statistics and the distribution function is given by

$$f_{\mathrm{FD}}(E, \mu, T) = \frac{1}{e^{\beta(E-\mu)} + 1}, \tag{2}$$

where $\beta = 1/(k_B T)$, and k_B is Boltzmann's constant. Bosonic particles obey Bose–Einstein statistics with a distribution function

$$f_{\mathrm{BE}}(E, \mu, T) = \frac{1}{e^{\beta(E-\mu)} - 1}. \tag{3}$$

Changing the integration variable k to E introduces a function dk/dE into the integral. The group velocity is given in one dimension by $v = \hbar^{-1} dE/dk$, and thus, it cancels the function dk/dE [18]. Here, $\hbar = h/(2\pi)$ is the reduced Planck constant. Consequently, the integral becomes

$$\dot{Q} = \int_{E(0)}^{\infty} \frac{dE}{2\pi\hbar} E[f_R(E, \mu_R, T_R) - f_L(E, \mu_L, T_L)]. \tag{4}$$

Assuming a linear response to the temperature and the chemical potential, the thermal current from the left to the right reservoir can be written as [18]

$$\delta\dot{Q} = \left(\frac{\partial \dot{Q}}{\partial \mu}\right)_T \delta\mu + \left(\frac{\partial \dot{Q}}{\partial T}\right)_\mu \delta T, \tag{5}$$

where $\delta\mu = \mu_R - \mu_L$ is the potential difference and $\delta T = T_R - T_L$ the temperature difference between the two reservoirs. The transport coefficients are obtained in the limit $\delta T \to 0$, $\delta\mu \to 0$ [18]. The derivations in Eq. (5) can be performed with respect to either reservoir if the sign is taken into account.

Setting the potential difference between the reservoirs to zero, we are left with the latter term in Eq. (5), which defines the quantum of thermal conductance [18]. Using Eqs. (5), (4), and (2) or (3), we obtain that the heat conductance $\dot{Q} = G_Q \delta T$ is given by the quantum of thermal conductance [18]

$$G_Q = \frac{\partial \dot{Q}}{\partial T} = \frac{\pi k_B^2}{6\hbar} T, \tag{6}$$

where $T = (T_R + T_L)/2$. This result is valid for both fermions and bosons. In fact, it is valid for even more general distribution functions [18]. We derive this result for photons in Sec. 2.8. The quantum of thermal conductance gives the upper bound to thermal conductance through a single channel. In case of multiple channels, the thermal conductance is limited by an integer multiple of the quantum of thermal conductance.

Similarly, one may calculate the electric current from [18]

$$I = \int_0^{\infty} \frac{dk}{2\pi} v(k)\{f_R[E(k), \mu_R, T_R] - f_L[E(k), \mu_L, T_L]\}, \tag{7}$$

and assuming linear response, one may write [18]

$$\delta I = \left(\frac{\partial I}{\partial \mu}\right)_T \delta\mu + \left(\frac{\partial I}{\partial T}\right)_\mu \delta T. \tag{8}$$

Here, the latter term vanishes [18]. For electrons, the electric conductance can be calculated from Eqs. (8), (7), and (2), and thus, the quantum of electric conductance is given by [18]

$$G_I = \frac{\partial I}{\partial \mu} = \frac{e^2}{h}. \tag{9}$$

In contrast to the thermal conductance, the electric conductance is not statistics independent.

2.2 Classical transmission line

Transmission lines are used for transmitting electrical signals in a variety of practical applications ranging from consumer electronics to industrial scale electronic devices. In this thesis, we consider transmission lines with a CPW structure, which is described in Chapter 3. A transmission line can be analysed using a lumped element model [19, 20]. In the model, a lumped element is defined as an electrical component with spatial dimensions significantly smaller than the wavelength.

The lumped element model of a transmission line is presented in Fig. 1. The transmission line is divided into segments of length Δx. The corresponding capacitance between the conductor line and the ground plane is given by $C = C_l \Delta x$, where C_l is the capacitance per unit length. Similarly, the inductance of the segment is given by $L = L_l \Delta x$. The capacitance and the inductance are assumed constant along the line. The current along the transmission line at point k is denoted by I_k, and the potential by V_k. We denote the total charge to the left of point k by Q_k. Here, we assume the transmission line to be infinitely long.

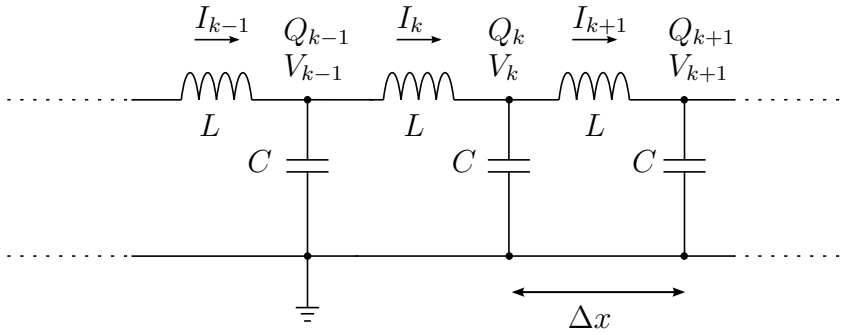

Figure 1: Lumped element model of an infinite transmission line. The voltage at point k over capacitor C is denoted by V_k, the current through inductor L is denoted by I_k, and the total cumulative charge to the left of point k (including point k) is denoted by Q_k. The length of a single segment is Δx.

The potential difference across the capacitor is given by

$$V_k = \frac{Q_k - Q_{k-1}}{C}. \tag{10}$$

At the continuum limit $\Delta x \to 0$ we obtain

$$V(x,t) = \frac{1}{C_l}\partial_x Q(x,t). \tag{11}$$

There is no charge transfer through the capacitors. Therefore, if the charge on the left side is reduced, the current along the transmission line is positive. Thus, the current can be written at the continuum limit as

$$I(x,t) = -\partial_t Q(x,t). \tag{12}$$

The energy of the inductors corresponds to the kinetic energy of the system, and the energy of the capacitors to the potential energy. Thus, the Lagrangian of the system can be written in the form

$$\begin{aligned} L &= \int dx \left\{ \frac{1}{2} L_l I(x,t)^2 - \frac{1}{2C_l} V(x,t)^2 \right\} \\ &= \int dx \left\{ \frac{L_l}{2} [\partial_t Q(x,t)]^2 - \frac{1}{2C_l} [\partial_x Q(x,t)]^2 \right\}. \end{aligned} \tag{13}$$

From Eq. (13), we identify the Lagrangian density

$$\mathcal{L} = \frac{L_l}{2} [\partial_t Q(x,t)]^2 - \frac{1}{2C_l} [\partial_x Q(x,t)]^2. \tag{14}$$

The Euler–Lagrange equation

$$\frac{\partial \mathcal{L}}{\partial Q} - \frac{\partial}{\partial t}\frac{\partial \mathcal{L}}{\partial \frac{\partial Q}{\partial t}} - \frac{\partial}{\partial x}\frac{\partial \mathcal{L}}{\partial \frac{\partial Q}{\partial x}} = 0, \tag{15}$$

can be simplified to

$$L_l \frac{\partial^2 Q(x,t)}{\partial t^2} - \frac{1}{C_l}\frac{\partial^2 Q(x,t)}{\partial x^2} = 0, \tag{16}$$

which is a wave equation for waves with velocity

$$v = \frac{1}{\sqrt{L_l C_l}}. \tag{17}$$

The canonically conjugated variable Π_Q can be obtained from Eq. (14):

$$\Pi_Q(x,t) = \frac{\partial \mathcal{L}}{\partial(\partial_t Q)} = L_l \partial_t Q(x,t) = -L_l I(x,t). \tag{18}$$

Thus, the Lagrangian density can be written using variables Π_Q and Q as

$$\mathcal{L} = \frac{1}{2L_l}[\Pi_Q(x,t)]^2 - \frac{1}{2C_l}[\partial_x Q(x,t)]^2. \tag{19}$$

The Hamiltonian of the system is given by the Legendre transform of the Lagrangian as

$$\begin{aligned} H &= \int dx \left\{[\partial_t Q(x,t)]\Pi_Q(x,t) - \mathcal{L}\right\} \\ &= \int dx \left\{\frac{1}{2L_l}\Pi_Q(x,t)^2 + \frac{1}{2C_l}[\partial_x Q(x,t)]^2\right\} \\ &= \int dx \left[\frac{1}{2}L_l I(x,t)^2 + \frac{1}{2}C_l V(x,t)^2\right]. \end{aligned} \tag{20}$$

The Hamiltonian gives the total energy in the transmission line since the system is conservative.

The solution of Eq. (16) can be presented by left- and right-moving waves [17, 21],

$$Q(x,t) = Q_L(t + x/v) + Q_R(t - x/v), \tag{21}$$

where v is given by Eq. (17). The left-moving waves can be rewritten using the inverse Fourier transform as

$$Q_L(t + x/v) = \frac{1}{2\pi}\int_{-\infty}^{\infty} d\omega Q_{L,\omega} e^{i\omega(t+x/v)}. \tag{22}$$

Since the charge is real, we have $Q_{L,\omega} = Q^*_{L,-\omega}$, and

$$Q_L(t + x/v) = \frac{1}{2\pi}\int_0^\infty d\omega Q_{L,\omega} e^{i\omega(t+x/v)} + \text{c.c.}, \tag{23}$$

where c.c. denotes the complex conjugate. Furthermore, using Eqs. (11) and (12), we obtain left-moving voltage and current waves

$$V_L(t + x/v) = \frac{1}{2\pi}\int_0^\infty d\omega V_{L,\omega} e^{i\omega(t+x/v)} + \text{c.c.}, \tag{24}$$

$$I_L(t + x/v) = \frac{1}{2\pi}\int_0^\infty d\omega I_{L,\omega} e^{i\omega(t+x/v)} + \text{c.c.}, \tag{25}$$

where $V_{L,\omega} = \frac{i\omega}{vC_l} Q_{L,\omega}$ and $I_{L,\omega} = -i\omega Q_{L,\omega}$. Analogously, we obtain for the right-moving waves

$$Q_R(t - x/v) = \frac{1}{2\pi}\int_0^\infty d\omega Q_{R,\omega} e^{i\omega(t-x/v)} + \text{c.c.}, \tag{26}$$

$$V_R(t - x/v) = \frac{1}{2\pi}\int_0^\infty d\omega V_{R,\omega} e^{i\omega(t-x/v)} + \text{c.c.}, \tag{27}$$

$$I_R(t - x/v) = \frac{1}{2\pi}\int_0^\infty d\omega I_{R,\omega} e^{i\omega(t-x/v)} + \text{c.c.}, \tag{28}$$

where $V_{R,\omega} = -\frac{i\omega}{vC_l} Q_{R,\omega}$ and $I_{R,\omega} = -i\omega Q_{R,\omega}$. We may now define the characteristic impedance or wave impedance as

$$Z_0 = \frac{V_{R,\omega}}{I_{R,\omega}} = \frac{-V_{L,\omega}}{I_{L,\omega}} = \sqrt{\frac{L_l}{C_l}}. \tag{29}$$

2.3 Quantisation of the transmission line

In canonical quantisation, the variables Q and Π_Q are replaced by operators $\hat{Q}$ and $\hat{\Pi}_Q$, which obey the commutation relations [17, 21]

$$\left[\hat{Q}(x,t), \hat{Q}(x',t)\right] = 0, \tag{30}$$

$$\left[\hat{\Pi}_Q(x,t), \hat{\Pi}_Q(x',t)\right] = 0, \tag{31}$$

$$\left[\hat{Q}(x,t), \hat{\Pi}_Q(x',t)\right] = i\hbar\delta(x - x'). \tag{32}$$

The operators are in the Heisenberg picture, that is, they depend on time. After the operator replacements, the Hamiltonian is given by

$$\begin{aligned}\hat{H} &= \int dx \left\{ \frac{1}{2L_l}\hat{\Pi}_Q(x,t)^2 + \frac{1}{2C_l}[\partial_x \hat{Q}(x,t)]^2 \right\} \\ &= \int dx \left\{ \frac{1}{2}L_l[\partial_t \hat{Q}(x,t)]^2 + \frac{1}{2C_l}[\partial_x \hat{Q}(x,t)]^2 \right\}. \end{aligned} \tag{33}$$

The Heisenberg equations of motion can be written in the form [17]

$$\begin{aligned}\partial_t \hat{Q}(x,t) &= -\frac{i}{\hbar}[\hat{Q}(x,t), \hat{H}] \\ &= \frac{1}{L_l}\hat{\Pi}_Q(x,t), \end{aligned} \tag{34}$$

$$\begin{aligned}\partial_t \hat{\Pi}_Q(x,t) &= -\frac{i}{\hbar}[\hat{\Pi}_Q(x,t), \hat{H}] \\ &= \frac{1}{C_l}\partial_x^2 \hat{Q}(x,t). \end{aligned} \tag{35}$$

These equations can be combined to give a wave equation similar to Eq. (16) [17]

$$L_l \frac{\partial^2 \hat{Q}(x,t)}{\partial t^2} - \frac{1}{C_l}\frac{\partial^2 \hat{Q}(x,t)}{\partial x^2} = 0. \tag{36}$$

The solution can be written as a combination of left- and right-moving waves as in the classical case:

$$\hat{Q}(x,t) = \hat{Q}_L(t + x/v) + \hat{Q}_R(t - x/v). \tag{37}$$

Consequently, using the Fourier transform, we obtain [17, 21]

$$\hat{Q}_L(t + x/v) = \sqrt{\frac{\hbar}{4\pi Z_0}} \int_0^\infty d\omega \frac{1}{\sqrt{\omega}} \hat{A}_{L,\omega} e^{-i\omega(t+x/v)} + \text{H.c.}, \tag{38}$$

$$\hat{Q}_R(t - x/v) = -\sqrt{\frac{\hbar}{4\pi Z_0}} \int_0^\infty d\omega \frac{1}{\sqrt{\omega}} \hat{A}_{R,\omega} e^{-i\omega(t-x/v)} + \text{H.c.}, \tag{39}$$

where Z_0 is the characteristic impedance defined in Eq. (29), the operators $\hat{A}_{L,\omega}$ and $\hat{A}_{R,\omega}$ are the annihilation operators for left- and right-moving photons, and H.c. denotes the Hermitian conjugate. Here we have used the fact that the operators corresponding to physical observables are Hermitian. The prefactor and the minus sign are chosen to simplify the equations below [17].

The annihilation operators satisfy the commutation relations [21]

$$\left[\hat{A}_{\alpha,\omega}, \hat{A}_{\alpha',\omega'}\right] = 0, \tag{40}$$

$$\left[\hat{A}_{\alpha,\omega}, \hat{A}^{\dagger}_{\alpha',\omega'}\right] = \delta(\omega-\omega')\delta_{\alpha,\alpha'}, \tag{41}$$

where $\alpha, \alpha' \in \{L, R\}$. The Hermitian conjugates of the annihilation operators are the corresponding creation operators.

Using the annihilation and creation operators, the Hamiltonian (33) can be simplified to the form [17]

$$\hat{H} = \int_0^\infty d\omega \hbar\omega \left(\hat{A}^{\dagger}_{L,\omega}\hat{A}_{L,\omega} + \hat{A}^{\dagger}_{R,\omega}\hat{A}_{R,\omega}\right) + \text{const.} \tag{42}$$

The current and voltage operators for left- and right-moving waves can be calculated from $\hat{Q}_{L/R}$ using Eqs. (11) and (12) as in the classical case:

$$\hat{V}_L(t+x/v) = -i\sqrt{\frac{\hbar Z_0}{4\pi}}\int_0^\infty d\omega\sqrt{\omega}\hat{A}_{L,\omega}e^{-i\omega(t+x/v)} + \text{H.c.}, \tag{43}$$

$$\hat{V}_R(t-x/v) = -i\sqrt{\frac{\hbar Z_0}{4\pi}}\int_0^\infty d\omega\sqrt{\omega}\hat{A}_{R,\omega}e^{-i\omega(t-x/v)} + \text{H.c.}, \tag{44}$$

$$\hat{I}_L(t+x/v) = i\sqrt{\frac{\hbar}{4\pi Z_0}}\int_0^\infty d\omega\sqrt{\omega}\hat{A}_{L,\omega}e^{-i\omega(t+x/v)} + \text{H.c.}, \tag{45}$$

$$\hat{I}_R(t-x/v) = -i\sqrt{\frac{\hbar}{4\pi Z_0}}\int_0^\infty d\omega\sqrt{\omega}\hat{A}_{R,\omega}e^{-i\omega(t-x/v)} + \text{H.c.} \tag{46}$$

2.4 Transmission line of a finite length

The wave equation (16) obtained in the case of an infinitely long transmission line is valid also in the case of a transmission line of a finite length. Nevertheless, the finite length results in important properties including a characteristic frequency and a phase shift which are discussed here.

2.4.1 Characteristic frequency

We consider a transmission line which is open at both ends of the line. The current obeys the wave equation (16), and it is given by Eqs. (25) and (28).

It can be written as

$$I(x,t) = I_{L,\omega}(t + x/v) + I_{R,\omega}(t - x/v)$$
$$= \int_0^\infty \frac{d\omega}{\pi} \Big\{ |I_{L,\omega}| \sin\Big[\omega\Big(t + \frac{x}{v}\Big) + \varphi_{L,\omega}\Big] + |I_{R,\omega}| \sin\Big[\omega\Big(t - \frac{x}{v}\Big) + \varphi_{R,\omega}\Big] \Big\}, \quad (47)$$

where $\varphi_{L,\omega}$ and $\varphi_{R,\omega}$ are constant phase shifts. Here, we have used the property $a + a^* = 2\mathrm{Re}(a)$ valid for a complex number a. In addition, we have used $\mathrm{Re}\left[\exp(ia)\right] = \cos(a) = \sin(a + \pi/2)$, and included the complex phases of the amplitudes in $\varphi_{L,\omega}$ and $\varphi_{R,\omega}$.

Since the transmission line is open at both ends, the current must vanish at the end points $x = 0$ and $x = s$. These boundary conditions restrict the frequencies, and only frequencies

$$f_n = n f_0 \quad (48)$$

are possible. Here, the characteristic frequency can be written as

$$f_0 = \frac{v}{2s} = \frac{1}{2s} \frac{1}{\sqrt{L_l C_l}}, \quad (49)$$

where we have also used Eq. (17). The corresponding angular frequencies are defined as

$$\omega_n = 2\pi f_n. \quad (50)$$

Consequently, the current assumes the form

$$I(x,t) = \sum_{n=1}^{\infty} I_n \cos(\omega_n t) \sin\Big(\frac{\omega_n x}{v}\Big), \quad (51)$$

where I_n corresponds to $2|I_{L,\omega}| = 2|I_{R,\omega}|$, which are of the form of the Dirac delta function. Here, the time $t = 0$ is fixed so that the phase disappears. The solution has a form of a standing wave.

2.4.2 Phase shift

We study left-moving voltage waves without boundary conditions. The voltage wave for a single frequency component ω can be written using Eq. (24) as

$$V_L(x,t,\omega) = \mathrm{Re}\left[\tilde{V}_{L,\omega} e^{i(kx+\omega t)}\right], \quad (52)$$

where $\tilde{V}_{L,\omega}$ is the amplitude, and $k = \omega/v$ is the wave number. The voltage wave has different phases at different positions at a fixed time due to the exponent ikx. In fact, the complex phase can be included in the amplitude. Therefore, if the amplitude is $\tilde{V}_{L,\omega}$ at the origin, it is $e^{iks}\tilde{V}_{L,\omega}$ at $x = s$. Similarly, we obtain for the right-moving waves from Eq. (27)

$$V_R(x,t,\omega) = \mathrm{Re}\left[\tilde{V}_{R,\omega}e^{-(ikx+\omega t)}\right], \tag{53}$$

where $\tilde{V}_{R,\omega}$ is the amplitude, and the phase shift is opposite to the phase shift for the left-moving voltage waves. If the amplitude is $\tilde{V}_{R,\omega}$ at the origin, it is $e^{-iks}\tilde{V}_{R,\omega}$ at $x = s$. The phase shift is equal also for the current and charge.

In the quantum-mechanical case, the annihilation operator obtains an analogous phase shift. Therefore, if the operator is $\hat{A}_L$ at the origin, it is $e^{iks}\hat{A}_L$ at $x = s$. The creation operator is given by the Hermitian conjugate of the annihilation operator.

2.5 Modelling resistor as a transmission line

A physical resistor always produces voltage fluctuations. Therefore, it can be presented as an ideal resistor connected to a voltage source, as shown in Fig. 2(a). The voltage V_0 is given by

$$V_0 = V + RI_0. \tag{54}$$

The resistor can be modelled as a semi-infinite transmission line [17]. The analogous transmission line is shown in Fig. 2(b). The current at the end of the transmission line is given by [17]

$$I_0 = I_R - I_L = \frac{V_R - V_L}{Z_0} = \frac{V_0 - 2V_L}{Z_0}, \tag{55}$$

where $V_0 = V_R + V_L$. This can be rewritten in the form [17]

$$V_0 = 2V_L + Z_0 I_0, \tag{56}$$

which is analogous to Eq. (54). Thus, the resistor can be modelled as a transmission line with characteristic impedance equal to R, and the fluctuation voltage divided by two needs to be replaced by the left-moving voltage amplitude. Thus, the fluctuations induce the left-moving waves and the factor

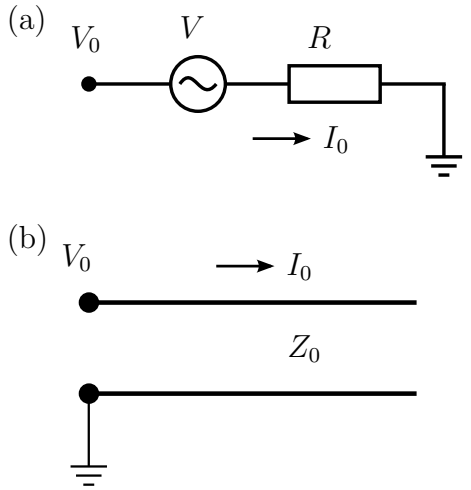

Figure 2: (a) Physical resistor can be presented as a series circuit of an ideal fluctuation-free resistor R and a voltage source V. The current through the resistor is denoted by I_0. (b) A semi-infinite transmission line with characteristic impedance Z_0. The voltage at the end of the line is denoted by V_0 and the current to the right by I_0.

of two can be explained by the fact that half of the voltage drop in a matched circuit will be across the resistor and the other half radiates into the transmission line.

The model of a resistor as a transmission line transforms a nonconservative system into a conservative one. The energy dissipated at a resistor is represented by waves which travel into the semi-infinite transmission line and never return.

2.6 Classical reflection and transmission coefficients

Classical reflection coefficients for two systems of particular interest are derived in Appendix A. The systems are two connected transmission lines and a transmission line terminated by an impedance. Here, we present an alternative method to derive the same results. This method is analogous with the one used in the quantum-mechanical case in Sec. 2.7.

It is feasible to study an impedance-terminated transmission line by modelling the real part of the impedance as a semi-infinite transmission line, and the imaginary part as inductive and capacitive lumped elements at the posi-

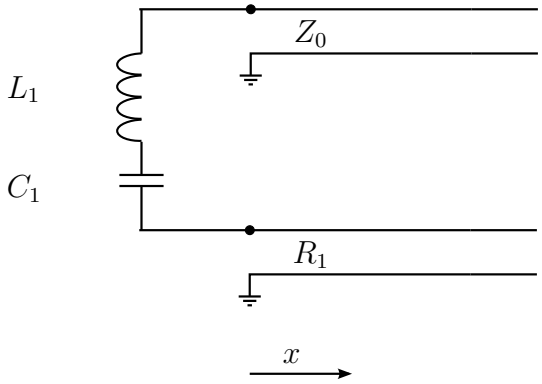

Figure 3: Transmission line terminated by an impedance presented as a combination of two semi-infinite transmission lines, a capacitor, and an inductor.

tion $x = 0$. In the most general case, an infinite number of these components are required to present the impedance. Here, we focus on a system consisting of two transmission lines with charge $Q(x)$, $x > 0$, in the line with a characteristic impedance Z_0, and $Q_1(x)$ in the line with a characteristic impedance R_1, combined with an inductance L_1 and a capacitance C_1 at $x = 0$. The system is presented in Fig. 3.

The Lagrangian density of the system can be written as [17]

$$\begin{aligned}\mathcal{L}(x) &= \delta(x)\left[\frac{L_1}{2}\dot{Q}_1(x)^2 - \frac{1}{2C_1}Q_1(x)^2\right] \\ &\quad +\theta(x)\left\{\frac{L_{1,l}}{2}\dot{Q}_1(x)^2 - \frac{1}{2C_{1,l}}[\partial_x Q_1(x)]^2\right\} \\ &\quad +\theta(x)\left\{\frac{L_l}{2}\dot{Q}(x)^2 - \frac{1}{2C_l}[\partial_x Q(x)]^2\right\}, \end{aligned} \tag{57}$$

and the Hamiltonian density as

$$\begin{aligned}\mathcal{H}(x) &= \delta(x)\left[\frac{L_1}{2}\dot{Q}_1(x)^2 + \frac{1}{2C_1}Q_1(x)^2\right] \\ &\quad +\theta(x)\left\{\frac{L_{1,l}}{2}\dot{Q}_1(x)^2 + \frac{1}{2C_{1,l}}[\partial_x Q_1(x)]^2\right\} \\ &\quad +\theta(x)\left\{\frac{L_l}{2}\dot{Q}(x)^2 + \frac{1}{2C_l}[\partial_x Q(x)]^2\right\}, \end{aligned} \tag{58}$$

where $\delta(x)$ is the Dirac delta function and $\theta(x)$ is the Heaviside step function

defined as

$$\Theta(x) = \begin{cases} 0, & \text{if } x < 0, \\ 1, & \text{if } x \geq 0. \end{cases} \tag{59}$$

The wave equation must be valid in both semi-infinite transmission lines. The boundary condition at $x = 0$ is given by Kirchhoff's laws. Thus, we obtain equations [17]

$$\ddot{Q}(x,t) = v^2 \partial_x^2 Q(x,t), \tag{60}$$

$$\ddot{Q}_1(x,t) = v_1^2 \partial_x^2 Q_1(x,t), \tag{61}$$

$$\frac{1}{C_l}\partial_x Q(x,t)|_{x=0} = \frac{1}{C_{1,l}}\partial_x Q_1(x,t)|_{x=0} - \frac{1}{C_1} Q_1(0,t) - L_1 \ddot{Q}_1(0). \tag{62}$$

Here, the velocity in the transmission line modelling the resistor can be chosen to be equal to the velocity in the physical transmission line, $v_1 = v$, since we have two free parameters, $C_{1,l}$ and $L_{1,l}$, which can simultaneously satisfy both conditions: $Z_0 = \sqrt{L_{1,l}/C_{1,l}}$ and $v = 1/\sqrt{C_{1,l}L_{1,l}}$ [17]. The solutions for the two transmission lines can again be written as a combination of left- and right-moving waves [17]:

$$Q(x,t) = \int_{-\infty}^{\infty} d\omega A_{L\omega} e^{i\omega(t+x/v)} - A_{R\omega} e^{i\omega(t-x/v)}, \tag{63}$$

$$Q_1(x,t) = \int_{-\infty}^{\infty} d\omega A_{1L\omega} e^{i\omega(t+x/v)} - A_{1R\omega} e^{i\omega(t-x/v)}. \tag{64}$$

Thus, using Eq. (62), one obtains [17]

$$Z_0(A_{L\omega} + A_{R\omega}) = Z_1(\omega)^* A_{1L\omega} + Z_1(\omega) A_{1R\omega}, \tag{65}$$

where $Z_0 = 1/(C_l v)$, $Z_1(\omega) = R_1 + i\omega L_1 + 1/(i\omega C_1)$, and $R_1 = 1/(C_{1,l} v)$. The value for the charge at point $x = 0$ can be chosen arbitrarily since it has no physical meaning [17]. Thus, we can set

$$Q(0,0) = -Q_1(0,0), \tag{66}$$

which gives [17]

$$A_{L\omega} - A_{R\omega} = -A_{1L\omega} + A_{1R\omega}. \tag{67}$$

Using these equations and Eq. (11), and setting $A_{1L\omega} = 0$, we obtain the same voltage reflection coefficient as in Eqs. (A.3) and (A.13):

$$\Gamma_V = \frac{A_{R\omega}}{A_{L\omega}} = \frac{Z_1(\omega) - Z_0}{Z_1(\omega) + Z_0}. \tag{68}$$

Similarly, the voltage transmission coefficient is given by

$$T_V = \frac{R_1 A_{1R\omega}}{Z_0 A_{L\omega}}. \tag{69}$$

Assuming Z_0 is real, and neglecting C_1 and L_1, we obtain

$$T_V = 1 + \Gamma_V, \tag{70}$$

which is the same as Eq. (A.5).

2.7 Quantum-mechanical reflection and transmission coefficients

In this section, quantum-mechanical reflection and transmission coefficients are calculated for two different systems. One of them is the same as in the previous section: two connected transmission lines. The other consists of a transmission line terminated by two resistors, a system corresponding to the fabricated samples.

2.7.1 Two connected transmission lines

Let us study a system consisting of two semi-infinite transmission lines that are combined with an inductor and a capacitor at position $x = 0$. This system is analogous to the system where a semi-infinite transmission line is terminated by an impedance and the resistance is modelled as a transmission line, which is presented in Fig. 3. The Hamiltonian operator can be obtained from the classical Hamiltonian in Eq. (58). The operator replacements are similar to the case of an infinite transmission line. In the original transmission line, the charge operator is denoted by $\hat{Q}$, and in the transmission line representing the resistor by $\hat{Q}_1$.

Again, the wave equation must be valid in both transmission lines and, consequently, the solution can be written as a combination of left- and right-moving waves [17]:

$$\hat{Q} = \int_0^\infty d\omega \sqrt{\frac{\hbar}{4\pi Z_0 \omega}} \left[\hat{A}_{L,\omega} e^{-i\omega(t+x/v)} - \hat{A}_{R,\omega} e^{-i\omega(t-x/v)} + \text{H.c.}\right], \tag{71}$$

$$\hat{Q}_1 = \int_0^\infty d\omega \sqrt{\frac{\hbar}{4\pi R_1 \omega}} \left[\hat{A}_{1L,\omega} e^{-i\omega(t+x/v)} - \hat{A}_{1R,\omega} e^{-i\omega(t-x/v)} + \text{H.c.}\right]. \tag{72}$$

The boundary conditions are also analogous to the classical case [17]. The condition

$$\hat{Q} = -\hat{Q}_1 \tag{73}$$

at position $x = 0$ results in equation

$$\frac{1}{\sqrt{Z_0}}(\hat{A}_{L\omega} - \hat{A}_{R\omega}) = \frac{1}{\sqrt{R_1}}(-\hat{A}_{1L\omega} + \hat{A}_{1R\omega}), \tag{74}$$

and the condition

$$\frac{1}{C_l}\partial_x \hat{Q}(x,t)|_{x=0} = \frac{1}{C_{1,l}}\partial_x \hat{Q}_1(x,t)|_{x=0} - \frac{1}{C_1}\hat{Q}_1(0,t) - L_1\ddot{\hat{Q}}_1(0), \tag{75}$$

results in equation

$$\sqrt{Z_0}(\hat{A}_{L\omega} + \hat{A}_{R\omega}) = \frac{1}{\sqrt{R_1}}\left[Z_1(\omega)\hat{A}_{1L\omega} + Z_1(\omega)^*\hat{A}_{1R\omega}\right]. \tag{76}$$

If we assume that $\hat{A}_{1L\omega} = 0$, we obtain [17]

$$\hat{A}_{R\omega} = \frac{Z_1(\omega)^* - Z_0}{Z_1(\omega)^* + Z_0}\hat{A}_{L\omega}. \tag{77}$$

This is analogous to the classical voltage reflection coefficient, and it can be written in terms of creation operators as [17]

$$\Gamma_V = \frac{\hat{A}^\dagger_{R\omega}}{\hat{A}^\dagger_{L\omega}} = \frac{Z_1(\omega) - Z_0}{Z_1(\omega) + Z_0}. \tag{78}$$

2.7.2 Resistors connected by a transmission line

We study a system consisting of two resistors connected to each other via a transmission line. The resistors are also connected to the ground potential. We model the system as two semi-infinite transmission lines that are connected to a transmission line of a finite length. Dimensionless inductive and capacitive components are included in the model at the two junctions, as shown in Fig. 4.

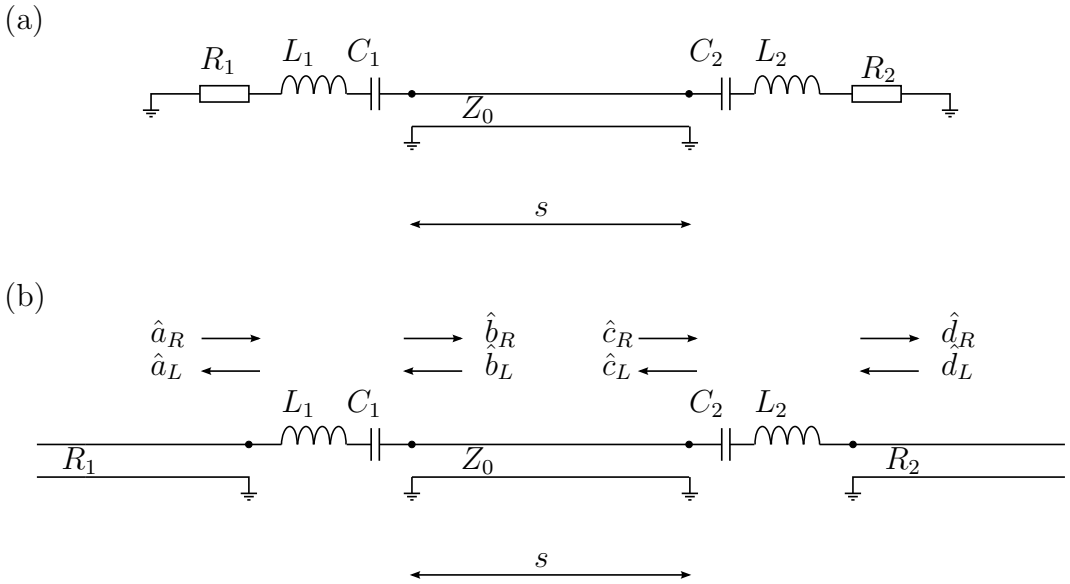

Figure 4: (a) Two grounded resistors are connected to a transmission line of a finite length s. In addition, inductors and capacitors are placed to the ends of the transmission line. (b) The two resistors connected by the transmission line presented as a system of three connected transmission lines. The annihilation operators for the left- and right-moving waves at the different points of the system are denoted by $\hat{a}_i, \hat{b}_i, \hat{c}_i$, and $\hat{d}_i$, $i \in \{L, R\}$.

The equations connecting the annihilation operators at different points of the system (see Fig. 4) are given by the boundary conditions and can be written as

$$\frac{1}{\sqrt{Z_0}}(\hat{b}_L - \hat{b}_R) = -\frac{1}{\sqrt{R_1}}(\hat{a}_R - \hat{a}_L), \tag{79}$$

$$\frac{1}{\sqrt{Z_0}}(\hat{c}_R - \hat{c}_L) = -\frac{1}{\sqrt{R_2}}(\hat{d}_L - \hat{d}_R), \tag{80}$$

$$\sqrt{Z_0}(\hat{b}_L + \hat{b}_R) = \frac{1}{\sqrt{R_1}}(Z_1\hat{a}_R + Z_1^*\hat{a}_L), \tag{81}$$

$$\sqrt{Z_0}(\hat{c}_R + \hat{c}_L) = \frac{1}{\sqrt{R_2}}(Z_2\hat{d}_L + Z_2^*\hat{d}_R), \tag{82}$$

$$\hat{c}_R = e^{i\phi}\hat{b}_R, \tag{83}$$

$$\hat{b}_L = e^{i\phi}\hat{c}_L, \tag{84}$$

where $\phi = \omega s/v$, $Z_1 = R_1 + 1/(i\omega C_1) + i\omega L_1$ and $Z_2 = R_2 + 1/(i\omega C_2) + i\omega L_2$. Since we have eight unknown operators and six equations, we can solve operators $\hat{a}_L$, $\hat{b}_L$, $\hat{b}_R$, $\hat{c}_L$, $\hat{c}_R$, and $\hat{d}_R$ as functions of $\hat{a}_R$, and $\hat{d}_L$.

In this circuit, the photons are noninteracting, which allows us to study separately photons coming from the left and from the right. The case of no photons coming from the right corresponds to the situation where the resistor R_1 is at finite temperature and the resistor R_2 is at zero temperature. The reflection and transmission coefficients can be solved using the boundary conditions. Similarly, one can solve the situation where no photons are coming from the left. The total heat transfer can then be solved by combining the two solutions.

Therefore, assuming no photons coming from the left, $\hat{d}_L = 0$, we obtain

$$\hat{a}_L = \frac{e^{2i\phi}(Z_1+Z_0)(Z_0-Z_2^*)+(Z_1-Z_0)(Z_0+Z_2^*)}{e^{2i\phi}(Z_0-Z_1^*)(Z_0-Z_2^*)-(Z_0+Z_1^*)(Z_0+Z_2^*)}\hat{a}_R, \tag{85}$$

$$\hat{b}_L = \frac{2e^{2i\phi}\sqrt{Z_0R_1}(Z_0-Z_2^*)}{e^{2i\phi}(Z_0-Z_1^*)(Z_0-Z_2^*)-(Z_0+Z_1^*)(Z_0+Z_2^*)}\hat{a}_R, \tag{86}$$

$$\hat{b}_R = -\frac{2\sqrt{Z_0R_1}(Z_0+Z_2^*)}{e^{2i\phi}(Z_0-Z_1^*)(Z_0-Z_2^*)-(Z_0+Z_1^*)(Z_0+Z_2^*)}\hat{a}_R, \tag{87}$$

$$\hat{c}_L = -\frac{i\sqrt{Z_0R_1}(Z_0-Z_2^*)}{IZ_0(Z1^*+Z_2^*)\cos(\phi)+(Z_0^2+Z_1^*Z_2^*)\sin(\phi)}\hat{a}_R, \tag{88}$$

$$\hat{c}_R = \frac{i\sqrt{Z_0R_1}(Z_0+Z_2^*)}{iZ_0(Z_1^*+Z_2^*)\cos(\phi)+(Z_0^2+Z_1^*Z_2^*)\sin(\phi)}\hat{a}_R, \tag{89}$$

$$\hat{d}_R = \frac{2i\sqrt{R_2R_1}Z_0}{iZ_0(Z_1^*+Z_2^*)\cos(\phi)+(Z_0^2+Z_1^*Z_2^*)\sin(\phi)}\hat{a}_R. \tag{90}$$

The reflection coefficient for the annihilation operators $r(\omega)$ is given by Eq. (85) and the transmission coefficient $t(\omega)$ by Eq. (90),

$$r(\omega) = \frac{e^{2i\phi}(Z_1+Z_0)(Z_0-Z_2^*)+(Z_1-Z_0)(Z_0+Z_2^*)}{e^{2i\phi}(Z_0-Z_1^*)(Z_0-Z_2^*)-(Z_0+Z_1^*)(Z_0+Z_2^*)}, \tag{91}$$

$$t(\omega) = \frac{2i\sqrt{R_2R_1}Z_0}{iZ_0(Z_1^*+Z_2^*)\cos(\phi)+(Z_0^2+Z_1^*Z_2^*)\sin(\phi)}. \tag{92}$$

The phase shift ϕ depends on the frequency.

We may study the special case with no lumped capacitances and inductances between the transmission lines, $Z_1 = R_1$ and $Z_2 = R_2$. The simplified model is presented in Fig. 5. Thus, the reflection and transmission coefficients can be simplified to

$$r_s(\omega) = \frac{e^{2i\phi}(R_2-Z_0)(R_1+Z_0)+(-R_1+Z_0)(R_2+Z_0)}{e^{2i\phi}(R_1-Z_0)(-R_2+Z_0)+(R_1+Z_0)(R_2+Z_0)}, \tag{93}$$

$$t_s(\omega) = \frac{2i\sqrt{R_1R_2}Z_0}{i(R_1+R_2)Z_0\cos(\phi)+(R_1R_2+Z_0^2)\sin(\phi)}. \tag{94}$$

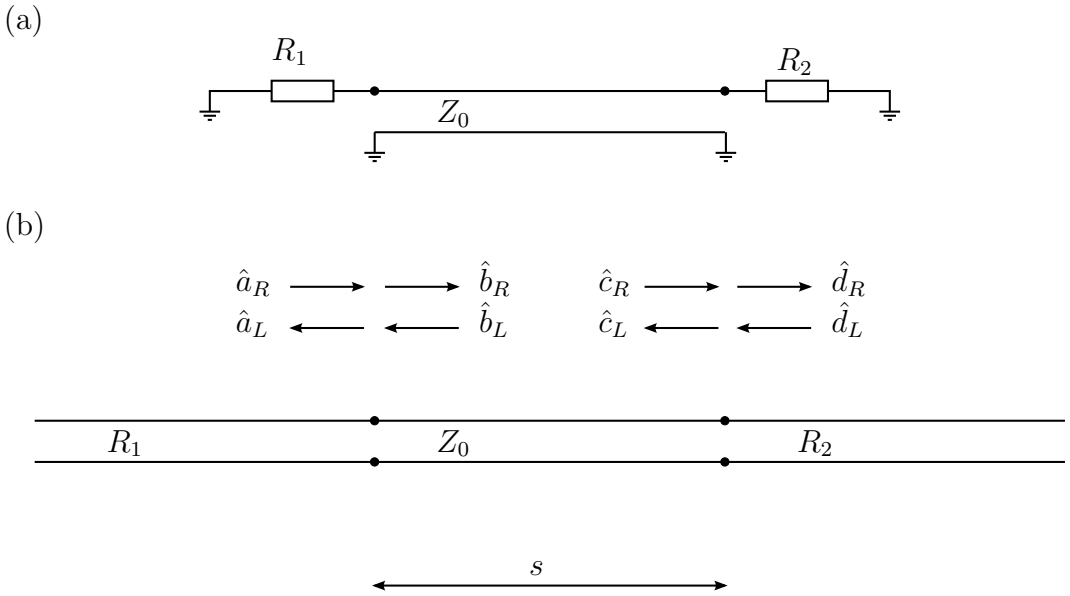

Figure 5: (a) Transmission line with characteristic impedance Z_0 is terminated by resistors R_1 and R_2. (b) The two resistors connected by a transmission line presented as a system of three connected transmission lines. The annihilation operators for the left- and right-moving waves at the different points of the system are denoted by $\hat{a}_i, \hat{b}_i, \hat{c}_i$, and $\hat{d}_i$, $i \in \{L, R\}$.

Energy conservation yields

$$|r(\omega)|^2 + |t(\omega)|^2 = 1. \tag{95}$$

The squared modulus of the simplified transmission coefficient obtains the form

$$|t_s(\omega)|^2 = \frac{2}{1 + \frac{R_1^2+R_2^2}{2R_1R_2} + \frac{R_1^2R_2^2+Z_0^4-R_1^2Z_0^2-R_2^2Z_0^2}{2R_1R_2Z_0^2}\sin^2(\phi)}. \tag{96}$$

Thus, a full transmission, $|t_s(\omega)|^2 = 1$, is obtained if $R_1 = R_2 = Z_0$. Furthermore, the transmission coefficient is symmetric with respect to the change of the resistances R_1 and R_2, as expected. Therefore, it is enough to consider only the case $\hat{d}_L = 0$ since the case $\hat{a}_R = 0$ is obtained by symmetry.

2.8 Photonic heat conduction between two resistors

Energy dissipation at the resistor R_2 is given by the average number of photons travelling to the right in transmission line R_2 multiplied by the energy

carried by a single photon. Therefore, the power per unit frequency is given by

$$\begin{aligned} P_{\rightarrow,\omega} &= \langle \hbar\omega \hat{d}_R^\dagger \hat{d}_R \rangle \\ &= \hbar\omega |t(\omega)|^2 \langle \hat{a}_R^\dagger \hat{a}_R \rangle \\ &= \hbar\omega |t(\omega)|^2 \frac{1}{\exp(\frac{\hbar\omega}{k_B T_1}) - 1}, \end{aligned} \tag{97}$$

since the number of photons coming from the left is given in thermal equilibrium by the Bose–Einstein distribution. By symmetry, the power transfer to the other direction is given by

$$P_{\leftarrow,\omega} = \hbar\omega |t(\omega)|^2 \frac{1}{\exp(\frac{\hbar\omega}{k_B T_2}) - 1}. \tag{98}$$

The net photonic power transfer from R_1 to R_2 can be expressed as

$$\begin{aligned} P_\Gamma &= \int_0^\infty \frac{d\omega}{2\pi} (P_{\rightarrow,\omega} - P_{\leftarrow,\omega}) \\ &= \int_0^\infty \frac{d\omega}{2\pi} \hbar\omega |t(\omega)|^2 \left(\frac{1}{\exp(\frac{\hbar\omega}{k_B T_1}) - 1} - \frac{1}{\exp(\frac{\hbar\omega}{k_B T_2}) - 1} \right). \end{aligned} \tag{99}$$

In the special case of full transmission, the power simplifies to

$$\begin{aligned} P_{\max} &= \int_0^\infty \frac{d\omega}{2\pi} \hbar\omega \left(\frac{1}{\exp(\frac{\hbar\omega}{k_B T_1}) - 1} - \frac{1}{\exp(\frac{\hbar\omega}{k_B T_2}) - 1} \right) \\ &= \frac{\pi k_B^2}{12\hbar} (T_1^2 - T_2^2) \\ &= \frac{\pi k_B^2 T}{6\hbar} (T_1 - T_2), \end{aligned} \tag{100}$$

where we have defined $T = (T_1 + T_2)/2$. Thus, in the case of full transmission, the thermal conductance is given by

$$\begin{aligned} G &= \frac{P_{\max}}{T_1 - T_2} \\ &= \frac{\pi k_B^2 T}{6\hbar} \\ &= G_Q, \end{aligned} \tag{101}$$

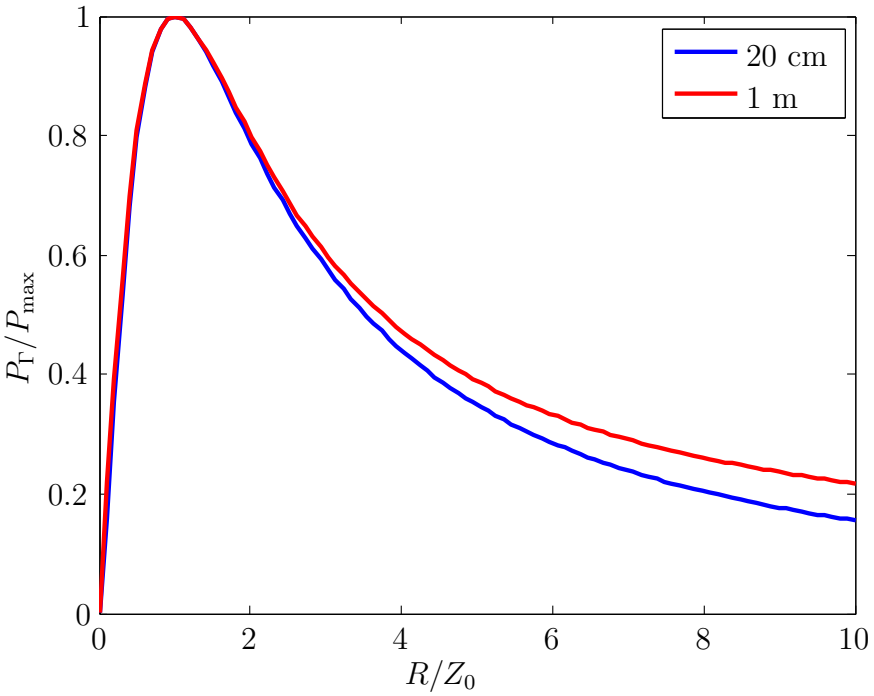

Figure 6: Photonic power as a function of the island resistance $R = R_1 = R_2$ for the distances of 20 cm and 1 m. The resistor temperatures are $T_1 = 250$ mK and $T_2 = 200$ mK. Here, P_Γ is the photonic power calculated with Eq. (99), where $|t(\omega)|^2$ is calculated according to Eq. (96), and $P_{\max}$ is the maximum heat transfer given by the quantum of thermal conductance according to Eq. (100). The phase velocity is calculated according to Eq. (17), and the characteristic impedance according to Eq. (29) with $C_l = 1.5 \times 10^{-10}$ Fm^{-1} and $L_l = 4.1 \times 10^{-7}$ Hm^{-1}. These values correspond to the experimental samples.

where $G_Q = \frac{\pi k_B^2 T}{6\hbar}$ is the quantum of thermal conductance presented in Sec. 2.1.

In a more general case, the power can be solved numerically from Eq. (99) with $t(\omega)$ given by Eq. (92), and in the simplified case with $t_s(\omega)$ given by Eq. (94). The conductance of a single channel is limited by the quantum of thermal conductance, and the maximum power transfer between two resistors is obtainable if the resistors have resistances equal to the characteristic impedance of the transmission line.

The photonic heat transfer depends on the matching between the resistors and the transmission line as shown in Fig. 6. Photonic heat conduction P_Γ ob-

tains its maximum value $P_{\max}$ given by the quantum of thermal conductance for $Z_0 = R_1 = R_2$. The photonic power is more than 90 % of its maximum value if $R/Z_0 \in [0.62, 1.60]$ in case of a 1-m distance. Here, $R = R_1 = R_2$. For a 20-cm-long transmission line, the ratio $P_\Gamma/P_{\max}$ is slightly below that of a 1-m-long transmission line.

The result in Eq. (100) is the same as in Ref. [4], where it is derived from Johnson–Nyquist noise [22, 23] using formula [24]

$$P = \int_0^\infty \frac{d\omega}{2\pi} \frac{4R_1R_2}{|Z(\omega)|^2} \hbar\omega \left(\frac{1}{\exp(\frac{\hbar\omega}{k_B T_1}) - 1} - \frac{1}{\exp(\frac{\hbar\omega}{k_B T_2}) - 1} \right), \tag{102}$$

and assuming perfect matching $R_1 = R_2$, $Z(\omega) = R_1 + R_2$, the quantum of thermal conductance is retrieved.

2.9 Normal-metal–insulator–superconductor junction

In this section, we study a structure where normal-metal (N) and superconducting (S) electrodes are connected through an insulator layer (I) forming an NIS junction. This NIS structure can be further connected to form a symmetric SINIS structure, which is shown schematically in Fig. 7. First, some general properties of superconductors are discussed. After that, the principles of thermometry and refrigeration by NIS junctions are presented.

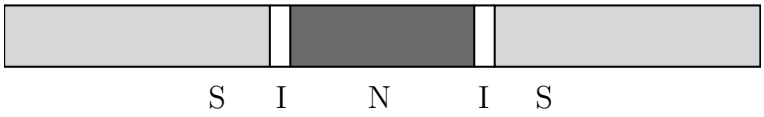

Figure 7: SINIS structure consists of two superconducting leads (S) and a normal-metal block (N) connected through insulating barriers (I).

2.9.1 Superconductivity

Superconductivity is a quantum phenomenon typically observed at low temperatures. It has many important features such as vanishing electrical resistance and perfect diamagnetism. The microscopic theory for superconductivity was formulated by Bardeen, Cooper and Schrieffer (BCS) in 1957 [25]. Here, two electrons with opposite momenta form a Cooper pair due to a weak

attractive interaction caused, for example, by lattice vibrations, phonons. Electrons are fermions, and therefore only one electron can occupy one state. Cooper pairs have integer spin and, thus, there is no limitation to the occupation number of a single state at the relevant scale.

The energy of a Cooper pair is lower than that of two unpaired electrons. The energy difference is denoted by 2Δ, because in order to brake a Cooper pair, both electrons need at least Δ of energy. At zero temperature, the energy gap is given by [26]

$$E_g = 2\Delta = 3.5 k_B T_C, \tag{103}$$

where T_C is the critical temperature defined as the transition temperature between the normal state and the superconducting state. The number of exited electrons, quasiparticles, is given by the Fermi–Dirac distribution function in Eq. (2).

The density of quasiparticle states in a superconductor can be presented by a semiconductor model [26]. The BCS density of states can be written as [26]

$$n_S(E) = N_0 \frac{|E|}{\sqrt{|E| - \Delta}} \Theta(|E| - \Delta), \tag{104}$$

where N_0 denotes the normal-state density of states, and θ is the Heaviside step function.

Since there are no states in the gap, there cannot exist electric current at vanishing temperature if the voltage difference over the NIS junction is zero. Nevertheless, a supercurrent can flow in a superconductor without a voltage difference. However, in real junctions a subgap current can be observed. This subgap current can be modelled by the Dynes density of states [27],

$$n_S(E) = N_0 \left| \mathrm{Re} \frac{E/\Delta + i\gamma}{\sqrt{(E/\Delta + i\gamma)^2 - 1}} \right|, \tag{105}$$

where γ is a parameter. Typically, γ is of the order 10^{-4} in high-quality aluminium–aluminium-oxide–normal-metal junctions. A heat current is possible through an NIS junction if there is a temperature difference across the junction.

2.9.2 Thermometer

NIS junctions can be used as secondary thermometers [28]. An electric current through an NIS junction is possible due to the fact that electrons can tunnel through the insulator. The tunnelling rate Γ^+ from the N electrode to the S electrode depends on the occupation number of the N electrode, which is given by the Fermi–Dirac distribution f_{FD} in Eq. (2). It also depends on the number of free states in the S electrode, which is proportional to $1 - f_{\mathrm{FD}}$. The occupation numbers are multiplied with the density of states functions in order to obtain the number of electrons at a given energy. We assume that the density of states is constant in the normal metal. The Fermi levels of the N and S electrodes can be shifted with respect to one another by applying a bias voltage $V = V_N - V_S$. With this definition, the current from N to S is positive at positive voltages. The total tunnelling rates are obtained by integrating over all energy states. The tunnelling rate Γ^- from the S electrode to the N electrode is calculated similarly. Thus, the tunnelling rates are given by [29, 30]

$$\Gamma^{\pm} = \frac{1}{e^2 R_T N_0} \int_{-\infty}^{\infty} n_S(E) f_{\mathrm{FD}}(E \pm eV, T_N)[1 - f_{\mathrm{FD}}(E, T_S)]dE, \qquad (106)$$

where R_T is the normal-state tunnelling resistance of the junction, and T_N and T_S are the electron temperatures of the N and S electrodes, respectively. The charging energy of the normal-metal island is neglected since the island is connected to the ground plane in the actual device by an NS contact without an insulating barrier.

The electric current can be calculated from the tunnelling rates, and it simplifies to [29, 31]

$$\begin{aligned} I &= -e(\Gamma^+ - \Gamma^-) \\ &= \frac{1}{eR_T N_0} \int_0^{\infty} n_S(E)[f_{\mathrm{FD}}(E - eV, T_N) - f_{\mathrm{FD}}(E + eV, T_N)]dE. \end{aligned} \qquad (107)$$

The current does not depend on the temperature of the superconductor, except weakly through $n_S(E)$, and hence it can be used as a thermometer for the electrons in the normal metal.

Two NIS junctions can be combined to an SINIS structure. If the junctions are similar, the voltage difference across a single NIS junction is half of the total voltage. Therefore, the voltage in Eq. (107) needs to be divided by 2.

2.9.3 Refrigeration

An NIS junction can be used for refrigeration of the normal metal since the electric current transfers also heat [28]. The amount of energy transferred by each electron is given by $E-eV$. Here, the potential is defined as $V = V_N - V_S$. The total heat currents can be calculated the same way as the tunnelling rates in Eq. (106), and they can be expressed as [29]

$$\dot{Q}^+ = \frac{1}{e^2 R_T N_0} \int_{-\infty}^{\infty} n_S(E)[E-eV] f_{\mathrm{FD}}(E-eV, T_N)[1-f_{\mathrm{FD}}(E, T_S)]dE, \quad (108)$$

$$\dot{Q}^- = \frac{1}{e^2 R_T N_0} \int_{-\infty}^{\infty} n_S(E)[E-eV] f_{\mathrm{FD}}(E, T_S)[1-f_{\mathrm{FD}}(E-eV, T_N)]dE. \quad (109)$$

By combining these, we obtain the refrigeration power [28]

$$\begin{aligned} P_{\mathrm{refr}}(V) = & \quad \dot{Q}^- - \dot{Q}^+ \\ & = \frac{1}{e^2 R_T N_0} \int_{-\infty}^{\infty} n_S(E)[E-eV][f_{\mathrm{FD}}(E-eV, T_N) - f_{\mathrm{FD}}(E, T_S)]dE. \end{aligned} \quad (110)$$

In contrast to the electric current, the power depends on the temperature of the S electrode. In a symmetric SINIS structure, the power needs to be multiplied by 2 and the voltage divided by 2. The principle of the SINIS refrigeration is shown in Fig. 8. In addition to refrigeration, the NIS junctions may be used as thermal diodes [32]. In case of small temperature differences and without applied voltages, the thermal rectification is of limited importance [32].

2.10 Electron–phonon coupling

Thermal energy of the atoms in a solid crystal produces lattice vibrations. The vibrations are analysed with a phonon model in which the vibrations have particle-like properties. The phonons can transfer energy and momentum in the lattice.

The electrons and phonons in the normal metal may have different temperatures. The heat transfer between the electrons and phonons at the normal-metal island $i = 1, 2$ (see Fig. 9) can be calculated according to the formula [4]

$$P_{\mathrm{ep},i} = \Sigma_{\mathrm{AuPd}} \Omega_i (T_0^5 - T_i^5). \quad (111)$$

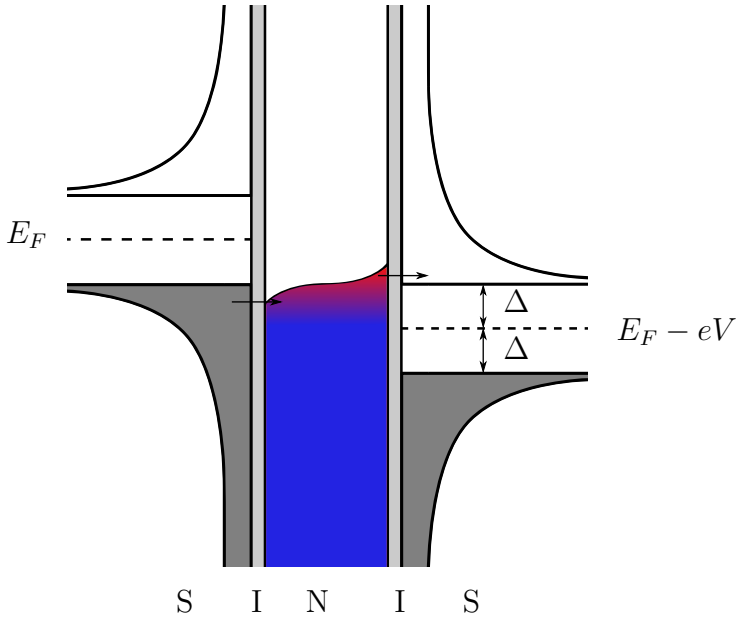

Figure 8: SINIS structure and the cooling mechanism. Cold electrons tunnel from the left superconductor to the normal metal, and hot electrons tunnel from the normal metal to the superconductor. Consequently, the electron temperature of the normal metal is reduced.

Here, $\Sigma_{\mathrm{AuPd}} = 3.0 \times 10^9$ $\mathrm{WK^{-5}m^{-3}}$ is a material parameter of AuPd [6], which is used as the normal metal, and Ω_i is the volume of the normal-metal block i. The fabricated samples have identical island volumes, $\Omega_1 = \Omega_2 = \Omega$.

2.11 Quasiparticle heat conduction

Cooper pairs in a superconductor do not transfer heat by the usual diffusion mechanism but the quasiparticles do [33]. The quasiparticle heat conduction into the island 1 (see Fig. 9) from the superconducting line can be described by the formula [4]

$$P_{\mathrm{qp},1} = \kappa_S A T'(x_1), \tag{112}$$

and out of the island 2 into the superconducting line by

$$P_{\mathrm{qp},2} = \kappa_S A T'(x_2), \tag{113}$$

where κ_S is the heat conductivity of the superconductor, A the cross-sectional area of the line, and $T'(x_i)$ the derivative of the temperature at x_i, $i = 1, 2$.

The island 1 is at $x_1 = 0$ and the island 2 at $x_2 = s$. Superconductor heat conductivity is given by [4, 34]

$$\kappa_S = \gamma(T_0)\kappa_N, \tag{114}$$

where γ is a suppression factor

$$\gamma(T_0) = \frac{3}{2\pi^2}\int_{\Delta/k_B T_0}^{\infty} \frac{t^2}{\cosh^2(t/2)} dt, \tag{115}$$

and κ_N is the normal-state heat conductivity of the line, which is obtained from the Wiedemann–Franz law as

$$\kappa_N = \frac{l}{A}\frac{L_0 T(x)}{R_l}. \tag{116}$$

Here, R_l is the normal-state electric resistance of the line, l is the length of the line, and $L_0 = 2.44 \times 10^{-8}$ WΩK^{-2} is the Lorenz number.

The temperature profile of the line can be calculated according to the heat diffusion equation [4]

$$\frac{d}{dx}\left(-\kappa_S \frac{dT}{dx}\right) = \alpha\Sigma_{\mathrm{Al}}[T_0^5 - T^5(x)], \tag{117}$$

where $\Sigma_{\mathrm{Al}} = 0.3 \times 10^9$ WK^{-5}m^{-3} is a material parameter of Al [6], which is used as the superconducting material. The heat source term on the right-hand side describes the electron–phonon coupling in the superconducting line, and it is suppressed by a factor [35]

$$\alpha \approx 0.98 e^{-\Delta/k_B T_0}, \tag{118}$$

with respect to the normal state.

If the distance between the normal-metal islands connected by a superconductor is large, the quasiparticles will be thermalised in the superconductor. At low temperatures the relaxation length of the quasiparticles can be large, and typically, the quasiparticle distribution thermalises over millimeter distances [36]. Nevertheless, the quasiparticles can thermalise in the normal-metal shadows which are present in the fabricated samples due to the fabrication method. The normal-metal shadows act as quasiparticle traps [37]. Thus, the quasiparticles transfer heat between the two normal-metal islands weakly.

In the limiting case with $\alpha = 0$, the temperature profile is linear, and the derivative of the temperature profile assumes the form $(T_2 - T_1)/s$. Therefore, the quasiparticle heat conduction in the studied samples is more than three orders of magnitude weaker than in samples where the length of the superconducting line is of the order of 50 μm as in Ref. [4]. Thus, it is of little importance in the thermal conductance between the islands. However, the normal-metal shadows that are in the vicinity of the islands may have an important contribution to the individual island temperatures.

2.12 Thermal model

In this section, the temperatures of the two normal-metal islands resistively terminating the transmission line (see Fig. 5) are analysed in a steady state. The thermal model of the system is presented in Fig. 9. The temperature of the island 1 is controlled by adjusting the refrigeration power P_{refr}. The temperature of the island 2 is then altered due to the heat conduction between the resistors. The heat conduction can be photon transmitted, P_{Γ}, or it can be transmitted by quasiparticles through the center conductor, which is thermally connected to the phonon bath. The quasiparticle heat conductions between the resistors and the center conductor are denoted by $P_{\mathrm{qp},i}$, $i = 1, 2$. The electron–phonon coupling between the electronic excitations in the resistors and the phonon bath are denoted by $P_{\mathrm{ep},i}$, and that between the center conductor and the phonon bath by $P_{\mathrm{ep,Al}}$. Thermometers need also be considered in the thermal model, and their powers are denoted by $P_{\mathrm{therm},i}$. They are calculated similarly to the refrigeration power, but a current bias is used instead of a voltage bias.

The observed refrigeration is not ideal, which can be modelled by a backflow power [37]

$$P_{\mathrm{bf},\beta} = \beta(IV + P_{\mathrm{refr}}), \tag{119}$$

where β is typically between 0.01 and 0.1. This power is assumed to be a consequence of the overheating of the superconducting lines [37]. Here, a constant portion of the total electric power is assumed to flow into the island [37].

An additional constant heating is included in the model. The constant heating powers $P_{\mathrm{const,i}}$ account for heat leaks from a high-temperature environment, and they result in saturating island temperatures at very low phonon temperatures.

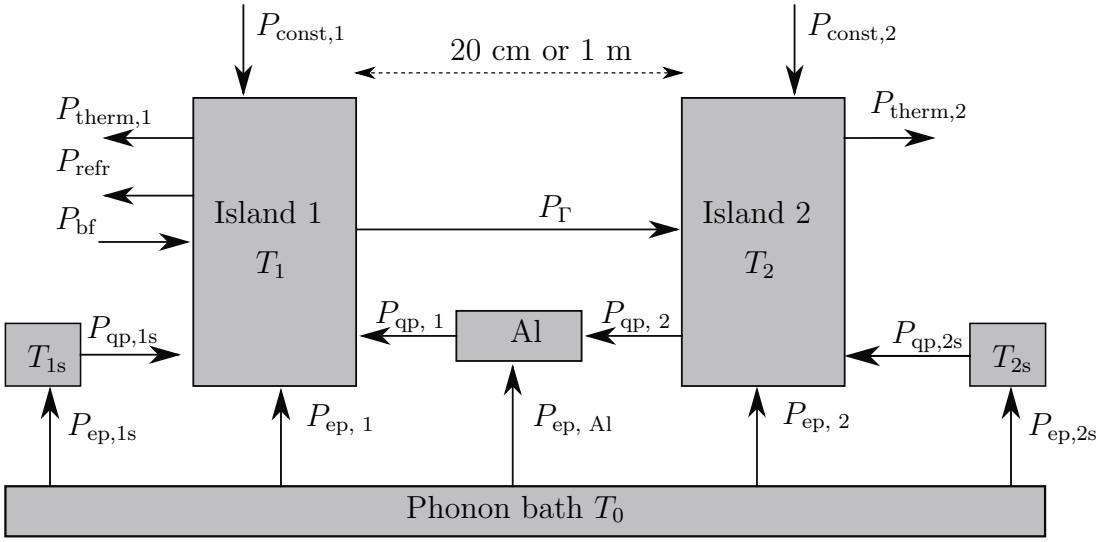

Figure 9: Thermal model of two normal-metal islands terminating a superconducting transmission line at temperatures T_1 and T_2 with additional normal-metal blocks at temperatures $T_{1\mathrm{s}}$ and $T_{2\mathrm{s}}$. The different powers included in the model are refrigeration P_{refr}, photonic heat conduction P_{Γ}, electron–phonon coupling $P_{\mathrm{ep},1}$, $P_{\mathrm{ep},2}$, $P_{\mathrm{ep,Al}}$, $P_{\mathrm{ep},1s}$, $P_{\mathrm{ep},2s}$, quasiparticle heat conduction $P_{\mathrm{qp},1}$, $P_{\mathrm{qp},2}$, $P_{\mathrm{qp},1s}$, $P_{\mathrm{qp},2s}$, thermometer powers $P_{\mathrm{therm},2}$, $P_{\mathrm{therm},2}$, backflow power P_{bf}, and constant heating powers $P_{\mathrm{const},1}$, $P_{\mathrm{const},2}$. The arrows indicate the directions of the positive heat flows.

The quasiparticle heat conduction between the normal-metal islands and the normal-metal shadows is taken into account. Instead of modelling the complex geometry of the structures near the islands in the fabricated samples, we use a phenomenological approach by considering additional normal-metal blocks of effective volume ν connected to both ends of the actual normal-metal islands. For simplicity, only one additional block connected to each island is drawn in Fig. 9. We denote the powers due to this quasiparticle heat conduction by $P_{\mathrm{qp},1\mathrm{s}}$ and $P_{\mathrm{qp},2\mathrm{s}}$ and the temperatures of the additional blocks by $T_{1\mathrm{s}}$ and $T_{2\mathrm{s}}$. In the simulations, these additional blocks are assumed to be connected to the actual islands through superconducting leads with cross-sectional area $A_l = (200 \times 100)$ nm^2, and length $l = 4$ μm, which correspond to the realised sample geometry. The normal-state resistivity of the leads is 1.5×10^{-8} Ωm [38]. The electron–phonon coupling in the superconducting leads is very weak and, therefore, it is neglected. We assume that the temperature of the leads used in Eq. (115) is approximately the same as the temperature of the normal-metal island. The additional blocks transfer heat with the phonon bath by electron–phonon coupling, which is denoted by

$P_{\mathrm{ep,1s}}$ and $P_{\mathrm{ep,2s}}$. This phenomenological approach can also account for the weak electron–phonon coupling in the superconducting ground planes and the center conductor.

Steady-state equations for both normal-metal islands and the additional normal-metal blocks are obtained by combining the different powers as

$$\begin{aligned} P_{\mathrm{refr}} - P_{\mathrm{bf}} + P_{\mathrm{therm,1}} + P_{\Gamma} - P_{\mathrm{ep,1}} - P_{\mathrm{qp,1}} - P_{\mathrm{const,1}} - P_{\mathrm{qp,1s}} &= 0, \quad (120) \\ P_{\mathrm{therm,2}} - P_{\Gamma} - P_{\mathrm{ep,1}} + P_{\mathrm{qp,2}} - P_{\mathrm{const,2}} - P_{\mathrm{qp,2s}} &= 0, \quad (121) \\ P_{\mathrm{qp,1s}} - P_{\mathrm{ep,1s}} &= 0, \quad (122) \\ P_{\mathrm{qp,2s}} - P_{\mathrm{ep,2s}} &= 0. \quad (123) \end{aligned}$$

The temperatures of the islands are given by these equations. Here, the effect of two junctions in an SINIS structure instead of a single NIS junction is included in the powers.

3 Sample design and analysis methods

In this chapter, the structure of the studied coplanar waveguide is presented followed by coupling capacitance simulations. Subsequently, the sample design is discussed as well as the concept of the quality factor. Finally, we discuss analysis methods for the quality factor and the thermometry.

3.1 Coplanar waveguide

A CPW transmission line consists of a center conductor and two ground planes on both sides of the center conductor. The structure of the CPW transmission line is schematically presented in Fig. 10. In the studied structure, the width of the center conductor is $w = 10$ μm, the width of the gap is $g = 5$ μm, the thickness of the metal is $t = 200$ nm, the thickness of the silicon substrate is $h_1 = 550$ μm, and the thickness of the oxide layer is $h_2 = 300$ nm. The relative permittivity of the silicon substrate is $\varepsilon_1 = 11.6$ [39], and the relative permittivity of the silicon oxide layer is $\varepsilon_2 = 3.78$ [39].

A CPW transmission line may support several different modes [40]. In a fundamental even mode, the potential of the center conductor oscillates with respect to the ground potential [40], as shown in Fig. 11(a). The fundamental even mode corresponds to quasi transverse electromagnetic (quasi-TEM) waves, and it is also known as the CPW mode [40, 41]. In a fundamental odd mode, the potentials of the two ground planes oscillate with respect to one another [40, 41], which is shown in Fig. 11(b). The properties of the fundamental odd mode depend on the finite width of the ground planes, and it can be suppressed by bonding the left part of the ground plane to the right part [40]. The fundamental odd mode is also known as the slot-line mode [40, 41]. The electric field of the CPW mode is confined to a smaller volume than that of the slot line mode, and the dispersion is lower in the CPW mode [40]. In addition to these modes, the CPW structure may support parasitic modes including a parasitic even mode where the potential of the ground planes and the center conductor oscillates with respect to the potential of the metallic shield surrounding the sample [40]. The CPW mode is the most important at low frequencies, whereas the other modes become important at higher frequencies depending on the geometry [41].

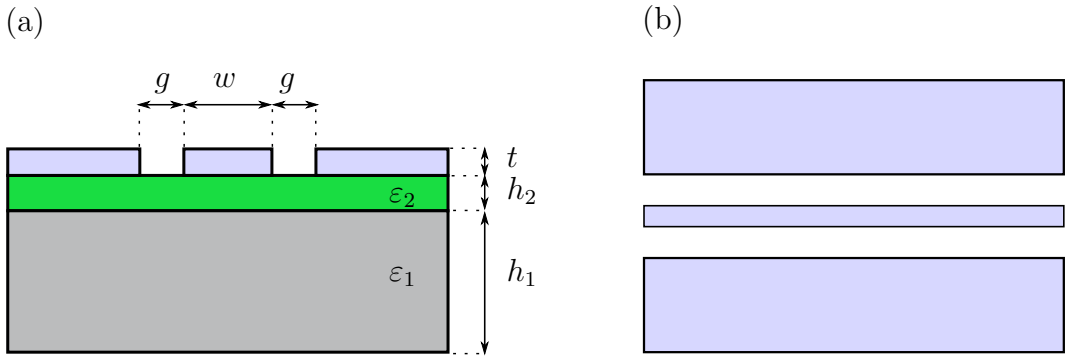

Figure 10: (a) Cross-section of a CPW transmission line. A layer of SiO_2 with permittivity ϵ_2 and thickness h_2 is formed on a Si wafer with ϵ_1 and thickness h_1. The metal layer has a thickness of t. The width of the center conductor is denoted by w, and the separation between the center conductor and the ground plane by g. (b) Top view of a CPW showing the center conductor and the ground plane. The relative dimensions are not to scale in these drawings.

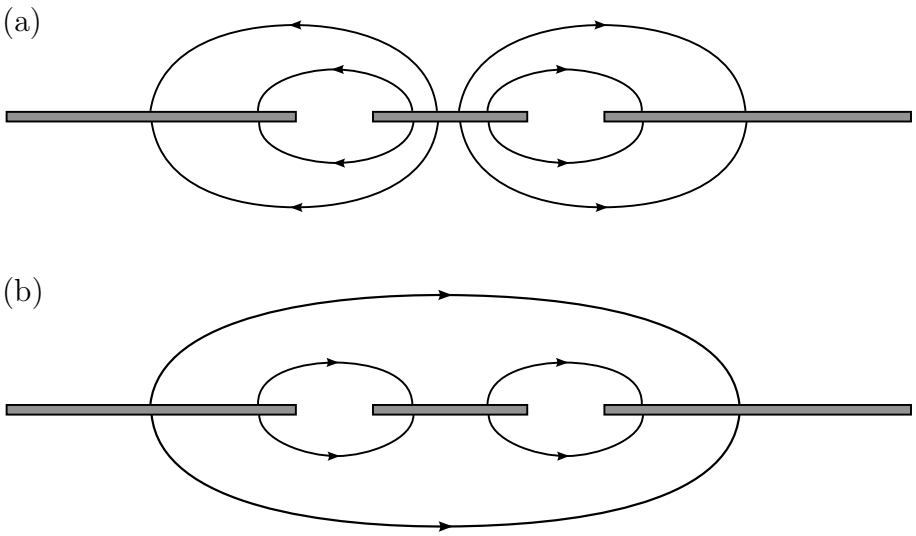

Figure 11: Schematically presented cross-section of the electric field lines of (a) a CPW mode, and (b) a slot line mode.

The phase velocity of the electromagnetic waves in a CPW transmission line is given by [39, 40]

$$v = \frac{c}{\sqrt{\varepsilon_{\text{eff}}}}, \tag{124}$$

where c is the velocity of light in vacuum and ε_{eff} is the effective permittivity. The effective permittivity for quasi-TEM modes can be calculated analytically as [42]

$$\varepsilon_{\text{eff}} = 1 + q_1(\varepsilon_1 - 1) + q_2(\varepsilon_2 - \varepsilon_1), \tag{125}$$

where the partial filling factors are given by

$$q_1 = \frac{1}{2}\frac{K(k_1)}{K(k_1')}\frac{K(k_0')}{K(k_0)}, \tag{126}$$

$$q_2 = \frac{1}{2}\frac{K(k_2)}{K(k_2')}\frac{K(k_0')}{K(k_0)}. \tag{127}$$

Here K denotes the complete elliptic integral of the first kind,

$$k_0 = \frac{w}{w+2s}, \tag{128}$$

$$k_1 = \frac{\sinh(\frac{\pi w}{4h_1})}{\sinh(\frac{\pi w}{4h_1} + \frac{\pi g}{gh_1})}, \tag{129}$$

$$k_2 = \frac{\sinh(\frac{\pi w}{4h_2})}{\sinh(\frac{\pi w}{4h_2} + \frac{\pi g}{gh_2})}. \tag{130}$$

and

$$k_i' = \sqrt{1 - k_i^2}, \tag{131}$$

where $i = 0, 1, 2$. The capacitance and inductance per unit length can be calculated as [39, 42, 43]

$$C_l = 4\varepsilon_0\varepsilon_{\text{eff}}\frac{K(k_0)}{K(k_0')}, \tag{132}$$

$$L_l = \frac{\mu_0}{4}\frac{K(k_0')}{K(k_0)}, \tag{133}$$

where ε_0 is the vacuum permittivity, and μ_0 vacuum permeability. These equations are valid for unshielded samples with vanishing metal film thickness. The characteristic impedance and the fundamental frequency are related to these by Eqs. (29) and (49). One can also calculate C_l numerically, and then obtain L_l using Eqs. (132) and (133) [39].

The total inductance per unit length for a superconducting CPW is given as a sum of the geometric inductance in Eq. (133) and kinetic inductance [41]. The kinetic inductance accounts for the magnetic energy within the conductor, and it originates from the inertia of the Cooper pairs, whereas the geometric

inductance accounts for the magnetic energy external to the conductor [41]. Analytical expressions for the kinetic inductance can be derived yielding results with rather good agreement with experimental measurements [44,45]. However, the kinetic inductance is approximately two orders of magnitude lower than the geometric inductance in CPWs with dimensions close to the ones studied in this thesis [39, 45]. Therefore, the kinetic inductance can be neglected, and the total inductance is assumed to be equal to the geometric inductance L_l given in Eq. (133).

3.2 Coupling capacitance

The transmission line is terminated at both ends by coupling capacitors. The capacitances of the capacitors vary according to their structure. Gap capacitors with a gap length ranging from 5 to 50 μm are studied. An example of such a structure is shown in Fig. 12. In addition, we study interdigital capacitors with the number of fingers ranging from 1+1 to 16+16. The length of the fingers is between 50 and 200 μm, and their width and separation are 5 μm. An optical micrograph of a finger capacitor is shown in Fig. 13. All the samples have identical capacitors at both ends of the resonator.

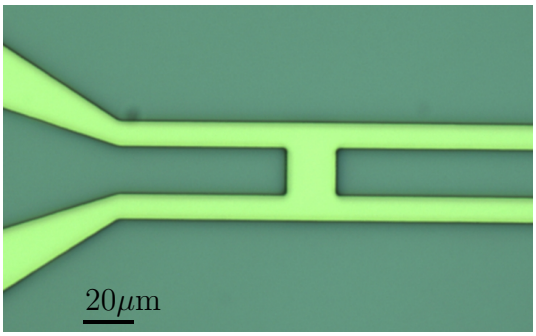

Figure 12: Optical micrograph of a coupling capacitor with 20 μm gap. The dark regions in the figure are metal in the fabricated sample.

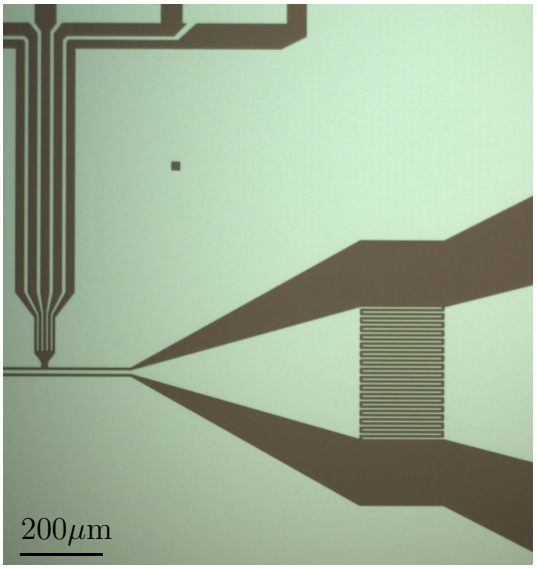

Figure 13: Optical micrograph of a sample with a 16+16 finger coupling capacitor. The width of the fingers and the gap between the fingers are both 5 μm, and the length of the fingers is 200 μm. In the upper left corner, part of the bonding pads is visible. No resistors are fabricated to this device. Metal appears bright in this image.

The capacitances are calculated with Comsol Multiphysics, which is a simulation program based on the finite element method (FEM). The capacitances can be calculated with analytical formulae [19] but we prefer simulations since that way the capacitor design and the surroundings can accurately be taken into account. The simulation results are presented in Table 1.

In the simulations, the simulated volume is spherical with a diameter of 500 μm in order to avoid electric field bending near the corners. The elements in the FEM simulation are tetrahedral. The size of the elements is limited to 2 μm in the region near the capacitors, and they are larger further away from the capacitors where the electric field is more uniform. Figure 14 shows the computational mesh, and Fig. 15 shows the resulting electric potential in an example case of a 4+4 finger capacitor.

Table 1: Capacitances obtained from FEM simulations for different coupling capacitor structures. The gap length is varied in the gap capacitors, whereas the number of fingers and the finger length are varied in finger capacitors. An example of a gap capacitor is shown in Fig. 12, and an example of a finger capacitor in Fig. 13.

Structure	Capacitance (fF)
50 μm gap	0.052
20 μm gap	0.18
10 μm gap	0.34
5 μm gap	0.53
50 μm finger, 1+1	2.35
100 μm finger, 1+1	4.28
100 μm finger, 2+2	13.3
100 μm finger, 3+3	22.8
100 μm finger, 4+4	32.3
100 μm finger, 6+6	51.7
100 μm finger, 8+8	70.7
200 μm finger, 8+8	136
100 μm finger, 10+10	89.7
200 μm finger, 10+10	172
200 μm finger, 16+16	279

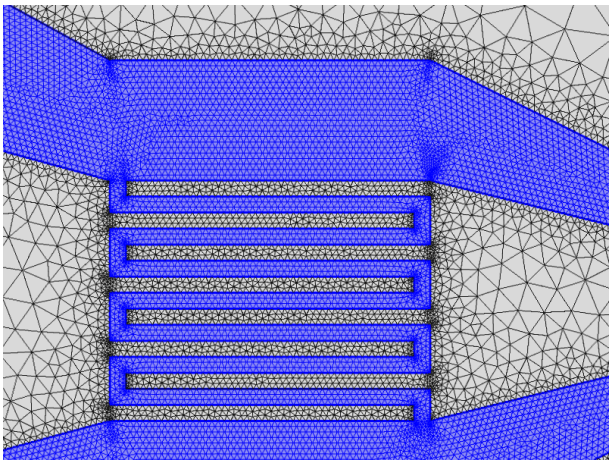

Figure 14: An example of coupling capacitance simulation mesh with a 4+4 finger capacitor. The fingers have a length of 100 μm and a width of 5 μm. Grey colour in the figure denotes metal.

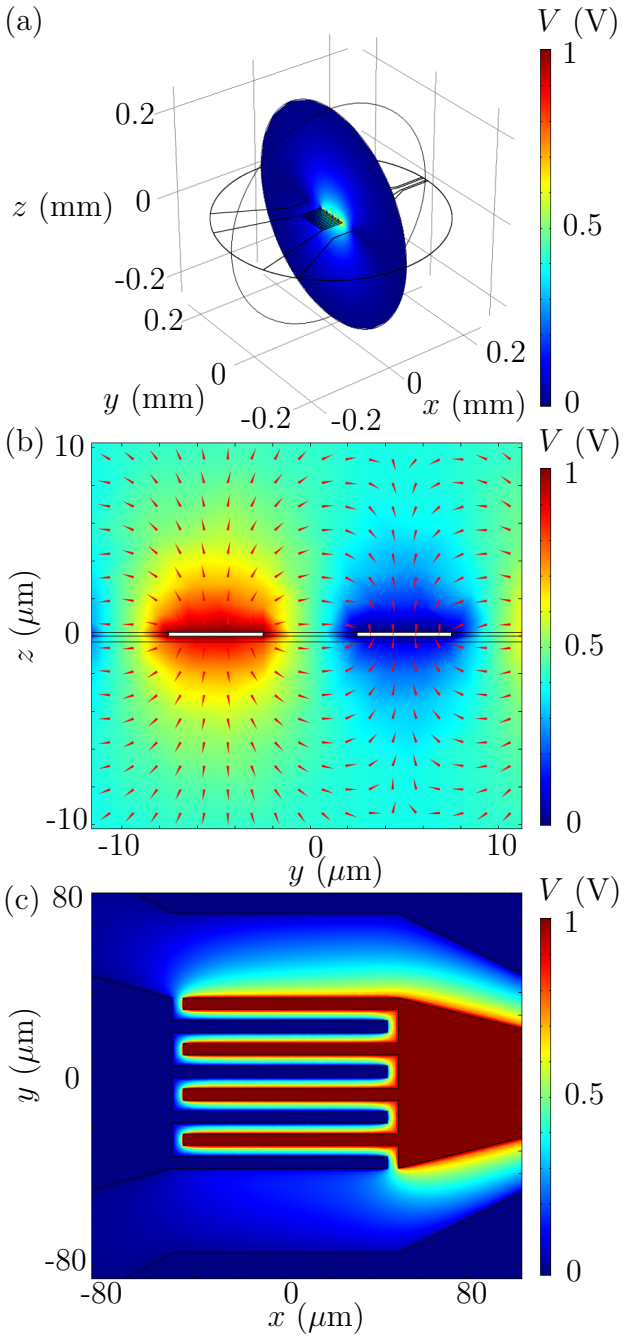

Figure 15: Example of coupling capacitance simulation results with a 4+4 finger capacitor. (a) Electric potential on an $x = 0$ plane. The center conductor is set to 1 V potential which is shown by the red colour while the blue colour indicates zero potential. (b) Close view of the potential on the $x = 0$ plane. The arrows indicate the direction of the electric field, and the white regions are the cross sections of the fingers. (c) Top view of the electric potential on a $z = 0$ plane.

3.3 Sample layout design

The samples are designed using Layout Editor software. Samples with two different resonator lengths are designed and fabricated. The shorter ones have a length of 19.26 cm $\approx$ 20 cm, and the longer ones 104.34 cm $\approx$ 1 m.

The design of the 20-cm sample is presented in Fig. 16. Superconducting CPWs with resembling double spiral structures can be used as wideband amplifiers [46], and as delay lines [47]. Here, the 20-cm resonator forms a double spiral structure with 14 full rotations. The distance between the adjacent CPW lines is 250 μm, and the S-shaped part in the center of the resonator consists of two arcs with a radius of 137.5 μm. The size of the chip is 1×1 cm^2. The 1-m sample is similar to the 20-cm sample but it has 35 full

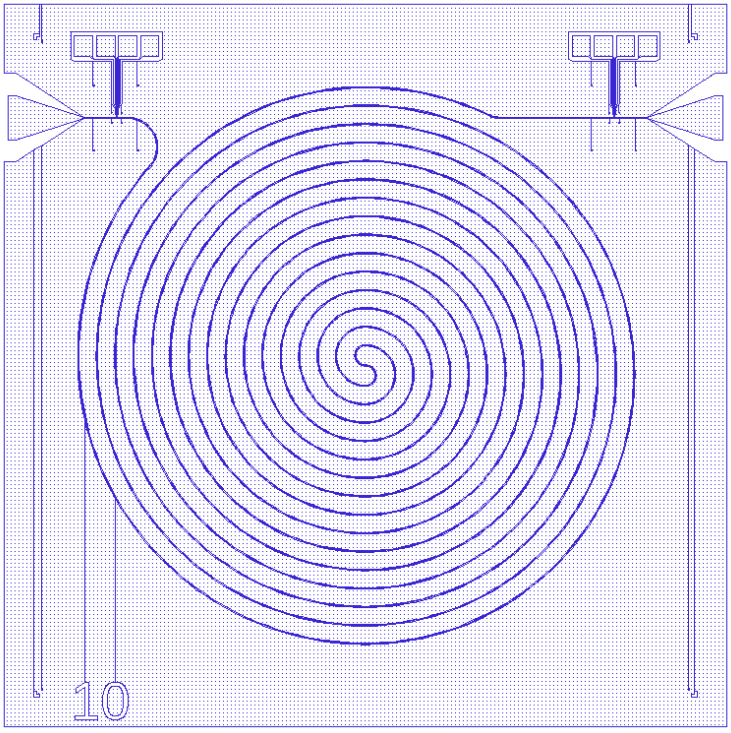

Figure 16: Sample design of a 20-cm resonator forming a double spiral structure. This design is utilised in the fabrication of a mask in the optical lithography. The marks at the corners enable alignment for fine-structure fabrication. Here, the resonator is terminated at both ends by 10-μm gap capacitors.

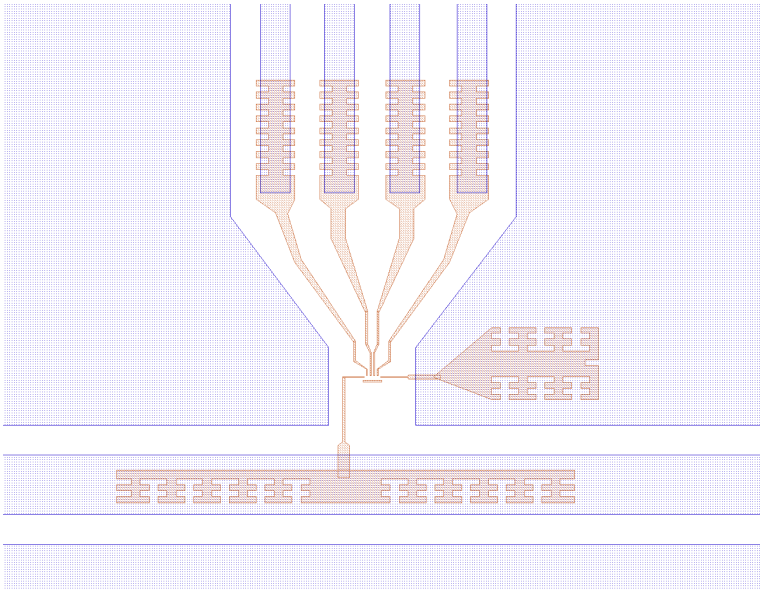

Figure 17: Mask design used for EBL. The red regions are drawn with EBL on top of the blue regions that have previously been fabricated by optical lithography.

rotations, and the chip size is 2×2 cm^2. The width of the center conductor is 10 μm, and the width of the gap between the center conductor and the ground plane is 5 μm in both 20-cm and 1-m samples.

The SINIS fine structures are fabricated with electron-beam lithography (EBL) near the ends of the resonator, and their design is shown in Fig. 17. The center conductor is terminated by the normal-metal blocks to the ground plane.

3.4 Quality factor and scattering parameters

There is always some loss in microwave resonators. It can be described by a quality factor Q defined as

$$Q = \omega_0 \frac{W_s}{P_l}, \tag{134}$$

where ω_0 is the angular frequency at the resonance, W_s the average energy stored in the resonator, and P_l the power loss [20]. The higher the Q factor, the longer is the time required to damp the signal.

An N-port microwave network presented in Fig. 18 can be analysed by studying scattering parameters S_{ij}. The scattering parameters are defined as matrix elements relating the in- and out-going voltage wave amplitudes V_i^+ and V_i^- for port i, respectively, as [20]

$$\begin{bmatrix} V_1^- \\ V_2^- \\ \vdots \\ V_N^- \end{bmatrix} = \begin{bmatrix} S_{11} & S_{12} & \cdots & S_{1N} \\ S_{21} & S_{22} & \cdots & S_{2N} \\ \vdots & \vdots & & \vdots \\ S_{N1} & S_{N2} & \cdots & S_{NN} \end{bmatrix} \begin{bmatrix} V_1^+ \\ V_2^+ \\ \vdots \\ V_N^+ \end{bmatrix}. \tag{135}$$

The scattering matrix depends on the frequency. In case of a 2-port network, it is a 2×2 matrix, where S_{11} gives the voltage reflection, and S_{21} the transmission.

Since the power is proportional to the squared amplitude of the voltage, it is also proportional to the squared amplitude of the scattering parameters. We define band width $\Delta\omega$ as the frequency range, outside which the power is reduced to one half or a smaller fraction of its maximum value. If $\omega_0 \gg \Delta\omega$, the quality factor can be expressed as [20]

$$Q = \frac{\omega_0}{\Delta\omega}. \tag{136}$$

Therefore, if the quality factor is very high, the peak in S_{21} as a function of frequency is narrow and the resonator is sensitive only to a small band of frequencies around the resonance frequency.

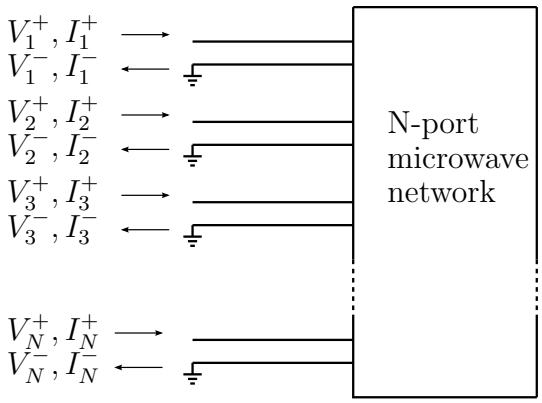

Figure 18: N-port network with in- and out-going current waves I_i^+, I_i^- and voltage waves V_i^+, V_i^-.

3.5 Scattering parameter analysis

In this section, we present the ABCD matrix method, which can be used for analysing the scattering parameters defined in Sec. 3.4. In addition, we describe several methods for extracting the quality factor from the measured scattering parameters.

3.5.1 ABCD matrix

The properties of the superconducting CPW resonator are simulated with Matlab. The scattering parameters of the system as functions of frequency are calculated using the ABCD matrix formalism [20,39]. The ABCD matrix is a transmission matrix of a two-port system [20]. It is defined as

$$\begin{bmatrix} V_1 \\ I_1 \end{bmatrix} = \begin{bmatrix} A & B \\ C & D \end{bmatrix} \begin{bmatrix} V_2 \\ I_2 \end{bmatrix}, \tag{137}$$

where the currents I_1, I_2 and the voltages V_1, V_2 are defined in Fig. 19. If the network consists of several components in series, the total ABCD matrix can be obtained as matrix product of the ABCD matrices of the components. Some ABCD matrices for simple two-port networks are listed in Ref. [20]. Thus, the ABCD matrix method is a very straightforward approach to calculating the total transmission and reflection coefficients for two-port systems consisting of several connected simpler two-port systems.

The scattering parameters can be obtained from the ABCD matrix by formulae [20]

$$S_{11} = \frac{A + B/Z_0 - CZ_0 - D}{A + B/Z_0 + CZ_0 + D}, \tag{138}$$

$$S_{12} = \frac{2AD - 2BC}{A + B/Z_0 + CZ_0 + D}, \tag{139}$$

$$S_{21} = \frac{2}{A + B/Z_0 + CZ_0 + D}, \tag{140}$$

$$S_{22} = \frac{-A + B/Z_0 - CZ_0 + D}{A + B/Z_0 + CZ_0 + D}. \tag{141}$$

The ABCD matrix of the CPW resonator can be calculated as [39]

$$\begin{bmatrix} A & B \\ C & D \end{bmatrix} = \begin{bmatrix} 1 & Z_{\text{in}} \\ 0 & 1 \end{bmatrix} \begin{bmatrix} t_{11} & t_{12} \\ t_{21} & t_{22} \end{bmatrix} \begin{bmatrix} 1 & Z_{\text{out}} \\ 0 & 1 \end{bmatrix}, \tag{142}$$

Figure 19: ABCD matrix representation of a two-port network with total currents I_1, I_2 and voltages V_1, V_2.

where

$$t_{11} = \cosh(\gamma s), \tag{143}$$
$$t_{12} = Z_0 \sinh(\gamma s), \tag{144}$$
$$t_{21} = \frac{1}{Z_0} \sinh(\gamma s), \tag{145}$$
$$t_{22} = \cosh(\gamma s), \tag{146}$$

and the coupling impedances are given by [39]

$$Z_{\text{in}} = Z_{\text{out}} = \frac{1}{i\omega C_\kappa}. \tag{147}$$

Here, the coefficient for wave propagation is given by

$$\gamma = \alpha + i\beta, \tag{148}$$

where α describes the damping of the signa, and β is the phase constant. In a lossless line,

$$\gamma = i\beta = ik = i\omega\sqrt{L_l C_l}, \tag{149}$$

where k is a wavenumber. There are no normal-metal resistors in this system.

The reflection and transmission coefficients obtained with the ABCD matrix method are identical to the ones in Eqs. (91) and (92) calculated with photonic creation and annihilation operators in case of vanishing damping. The ABCD matrix method allows taking the damping into account in a straightforward way.

3.5.2 RLC approximation

The experimental control samples consist of a transmission line Z_0 connected through coupling capacitors C_κ to external lines with characteristic

impedances R_L as shown in Fig. 20(a). Near the nth resonance, the CPW resonator can be modelled as a parallel RLC resonator, as shown in Fig. 20(b), where [39]

$$R = \frac{Z_0}{\alpha s}, \tag{150}$$

$$L = \frac{2L_l s}{n^2\pi^2}, \tag{151}$$

$$C = \frac{C_l s}{2}. \tag{152}$$

The angular frequency of the nth resonance is given by $\omega_n = n\omega_0$. The external transmission lines can be presented as resistors with resistances equal to the characteristic impedance. The coupling capacitors C_κ and the resistances of the lines R_L can be combined to a Norton equivalent parallel circuit [see Fig. 20(c)] yielding [39]

$$C^* = \frac{C_\kappa}{1+\omega_n^2 C_\kappa^2 R_L^2}, \tag{153}$$

$$R^* = \frac{1+\omega_n^2 C_\kappa^2 R_L^2}{\omega_n^2 C_\kappa^2 R_L}. \tag{154}$$

Energy dissipation of the whole circuit is characterised by a loaded quality factor Q_L. Assuming $C \gg C^*$, the loaded quality factor Q_L can be written as [39]

$$\frac{1}{Q_L} = \frac{1}{Q_{\text{int}}} + \frac{1}{Q_{\text{ext}}}, \tag{155}$$

where the internal quality factor is

$$Q_{\text{int}} = \frac{n\pi}{2\alpha s}, \tag{156}$$

and the external quality factor

$$Q_{\text{ext}} = \frac{\omega_n R^* C}{2}. \tag{157}$$

The Q_{int} factor describes the losses of the actual resonator, and Q_{ext} describes the losses of the other parts of the circuit. Combining Eqs. (152), (154)–(157) with Eqs. (48)–(50) and (124) we obtain

$$Q_L = \frac{n}{\dfrac{2\alpha s}{\pi} + \dfrac{4C_\kappa^2 R_L c\pi}{C_l s^2\sqrt{\varepsilon_{\text{eff}}}}n^2}. \tag{158}$$

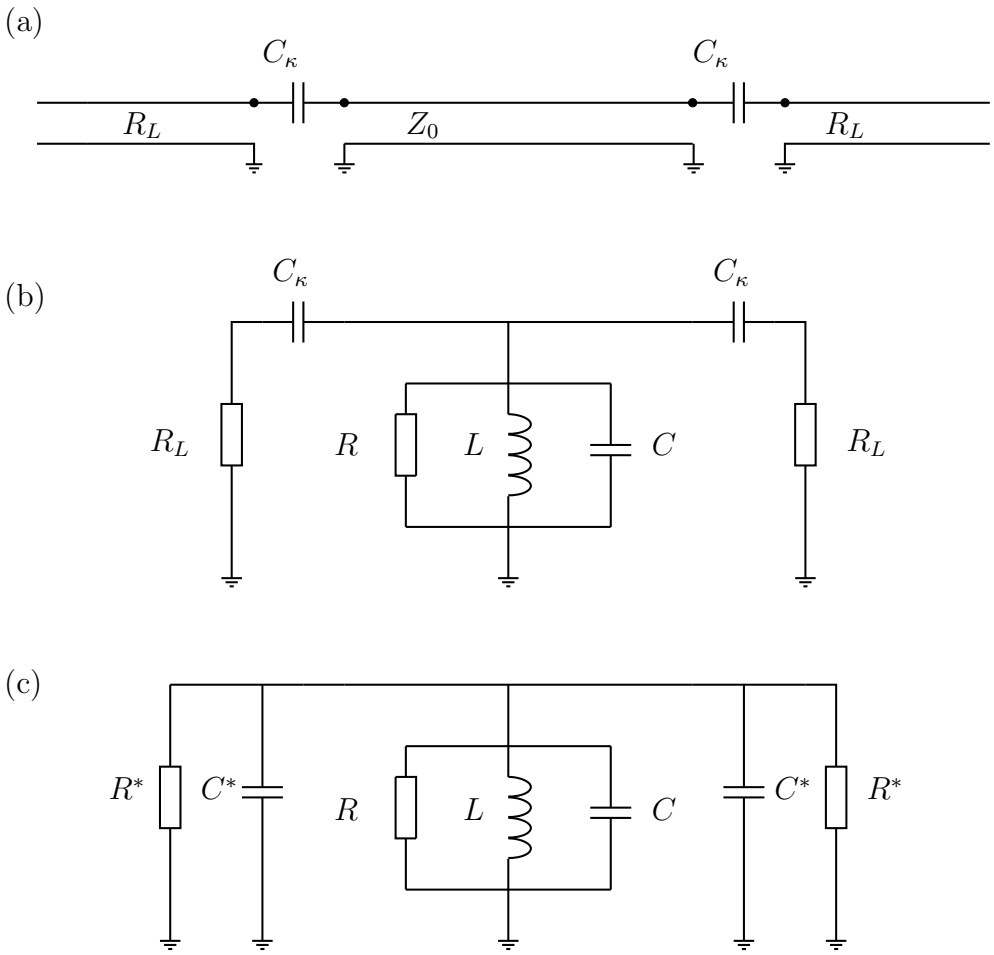

Figure 20: (a) Transmission line with a characteristic impedance Z_0 connected through coupling capacitances C_κ to external lines with characteristic impedances R_L. (b) The transmission line is modelled as a parallel RLC circuit, and the external lines as resistors. (c) The coupling capacitances and the resistances of the lines are presented as a Norton equivalent circuit with resistances R^* and capacitances C^*.

3.5.3 Q factor analysis

The samples are measured with a vector network analyser (VNA), which gives the scattering parameters of the samples as functions of frequency. The loaded quality factor Q_L is then obtained from the scattering parameters with various methods, as discussed below, following Ref. [48].

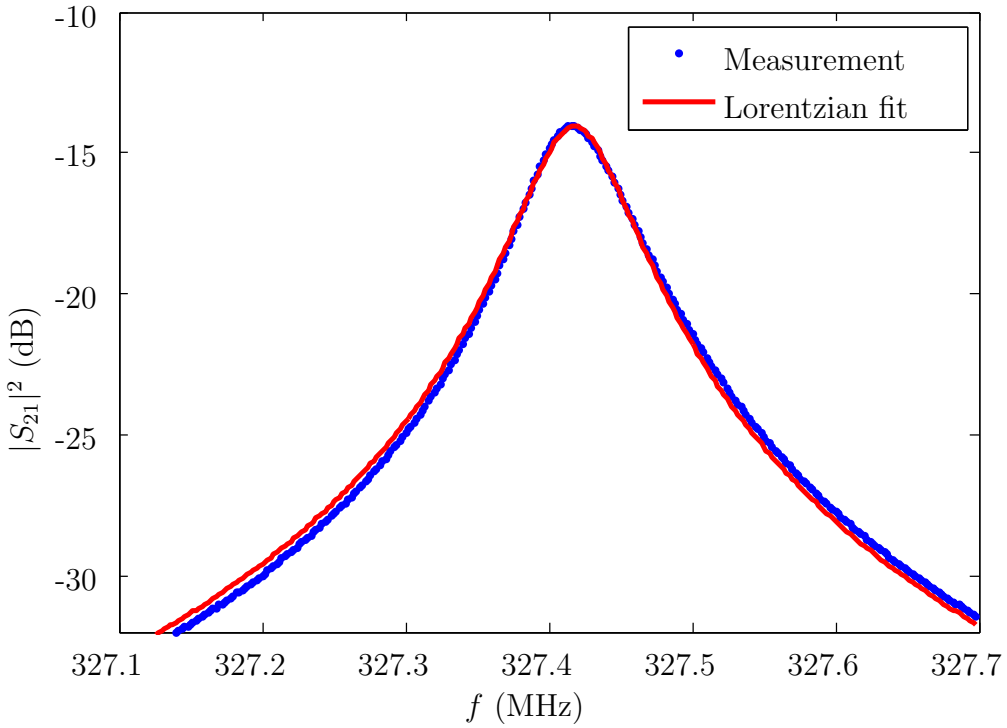

Figure 21: Lorentzian fit to a resonance peak $|S_{21}|^2$ as a function of frequency. The Lorentzian curve is symmetric whereas the measurement data shows asymmetric features. The measured resonator has a length of 20 cm and 8+8 coupling capacitors with a 200-μm finger length.

The first method is to calculate the Q factor according to Eq. (136), where ω_0 is the frequency at which the resonance occurs, and $\Delta\omega$ is the full width of the peak at which the power is reduced to one half. This method is very simple and it gives rather accurate results. However, if higher accuracy is required, more sophisticated methods are beneficial.

The second method is to calculate the Q factor from a Lorentzian fit to the resonance peak. The complex valued scattering parameter S_{21} is given by [48]

$$S_{21}(f) = \frac{\max(|S_{21}|)}{1 + iQ\left(\frac{f}{f_0} - 1\right)}. \tag{159}$$

This equation is based on the lumped element model, and it is valid near the resonance $f \approx f_0$. The squared magnitude of $S_{21}(f)$ has a Lorentzian shape

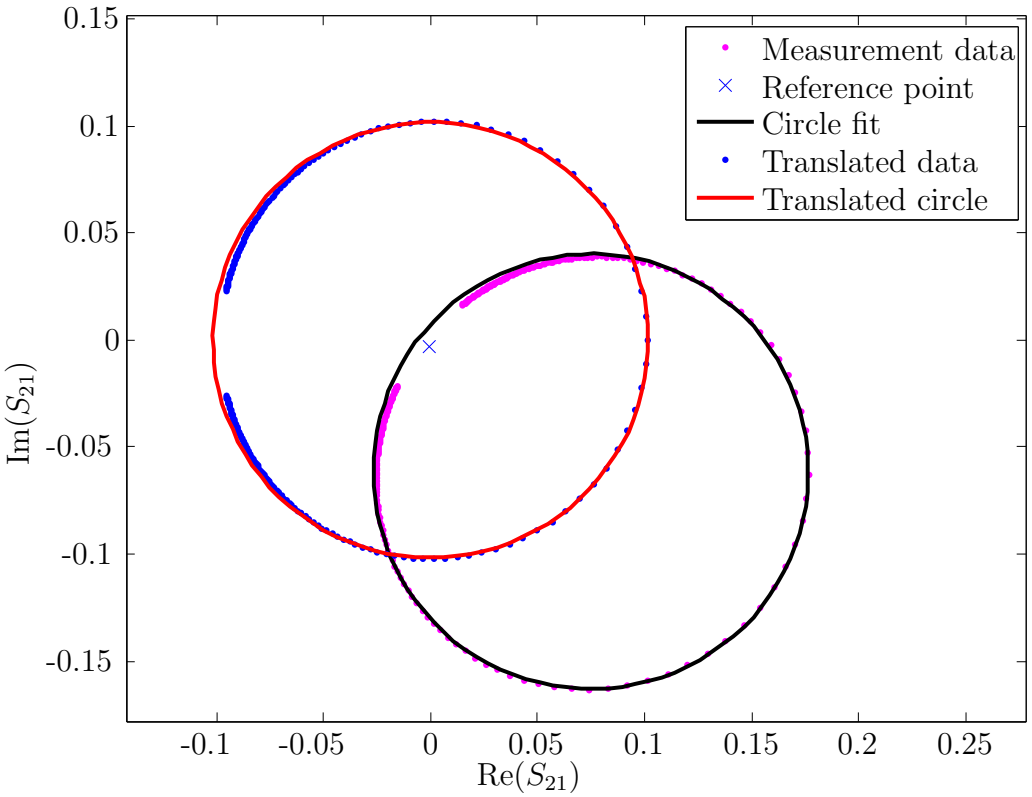

Figure 22: Scattering parameter S_{21} plotted on a complex plane. A circle is fitted to the measurement data, and the circle and the data are translated in such a way that the center of the circle is at the origin. The translated data and the circle are also rotated to align $\max(|S_{21}|)$ to the real axis. The reference point used in Eq. (162) is defined as an average of the first and the last data point.

given by [48]:

$$|S_{21}(f)|^2 = \frac{|\max(|S_{21}|)|^2}{1 + 4Q^2\left(\frac{f}{f_0} - 1\right)^2}. \tag{160}$$

The factors $\max(|S_{21}|)$, Q and f_0 are used as fitting parameters. An example of fitting a Lorentzian curve to measured data is shown in Fig. 21.

The third method is based on Eq. (159), which forms a circle in the complex plane. In an ideal case, the circle is in the canonical position with the center on the real axis and the arc intersecting the origin. The diameter of the circle in the canonical position gives directly the transmission. However, in case of a real sample, the circle is not in the canonical position due to the cross-talk

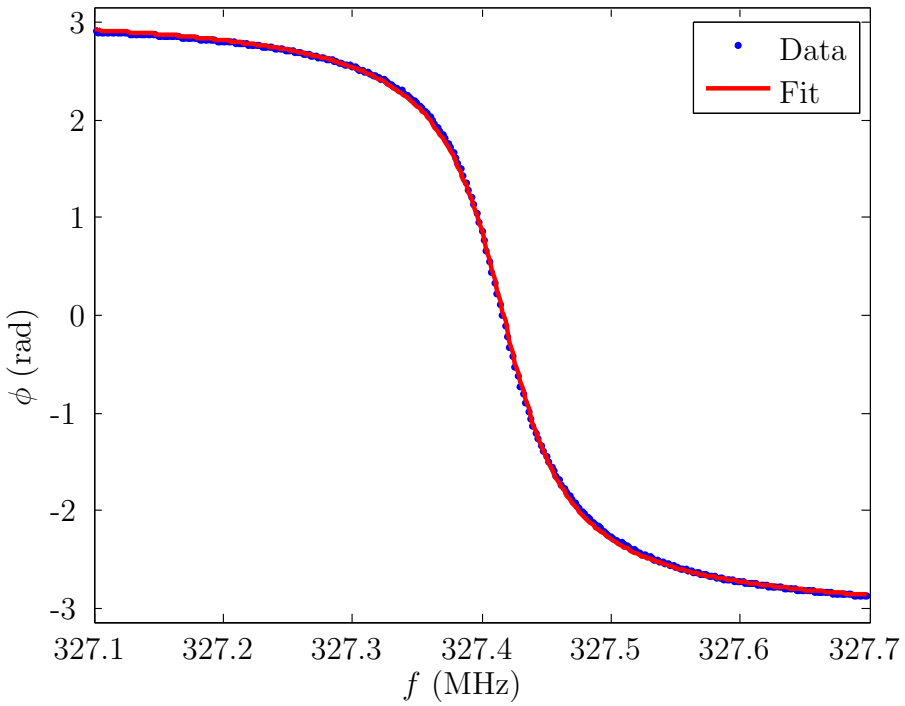

Figure 23: Phase as a function of frequency. The phase corresponds to the translated experimental data points on the complex plane obtained from the circle fit. A curve is fitted to the measurement data according to Eq. (163).

between cables, which causes a complex translation X [48]. In addition, a phase shift θ is introduced if the measurement ports do not coincide with the ports of the resonator [48]. The shifted and translated transmission coefficient has the form [48]

$$\tilde{S}_{21} = (S_{21} + X)e^{i\theta}. \tag{161}$$

A circle is fitted to the measurement data with a weight function [48]

$$W_i = [(x_{\text{ref}} - x_i)^2 + (y_{\text{ref}} - y_i)^2]^2, \tag{162}$$

where x_{ref} is defined as the average of the first and the last data point, and i denotes the point index. This weight function gives more weight to the point near the resonance. The fitted circle is first translated and rotated to the canonical position where it intersects the origin and has the center on the real axis. Then it is further translated in such a way that the center of the circle is at the origin of the complex plane. An example of the translation and the circle fit is shown in Fig. 22. The next step is to fit the phase of the translated measurement points as a function of the frequency. The complex phase of the translated circle is obtainable as an arctangent of the ratio of

the imaginary and real parts, and it can be written as [48, 49]

$$\phi(f) = 2\arctan\left[2Q\left(1 - \frac{f}{f_0}\right)\right]. \tag{163}$$

The fitting of the phase as a function of the frequency is presented in Fig. 23. This method typically gives the most reliable value for the Q factor although the Lorentzian fitting gives also very reliable results [48].

3.6 Temperature simulations

Experimentally obtained island temperatures are analysed by comparing the results with simulations. The system is described by the thermal model (see Fig. 9), and the simulations are performed with Matlab software, which is used to solve the thermal balance for the normal-metal islands from Eqs. (120) and (121), and for the additional normal-metal blocks from Eqs. (122) and (123). In the simulations, the refrigerator voltage and the temperature of the phonon bath are varied, which changes the heat flows in and out of the normal-metal islands. The parameters used in the simulations are based on the fabricated samples. No time dependence is taken into account, that is, the system is studied in the steady state.

Examples of the temperature simulation curves are shown in Fig. 24. The refrigeration voltage is swept and the temperatures of both islands are solved at various phonon bath temperatures T_0. Here, the system is studied in an ideal case with heat flows only in the form of refrigeration P_{refr}, electron–phonon coupling $P_{\mathrm{ep,i}}, i = 1, 2$, and photonic heat conduction P_Γ at the quantum limit. The backflow power P_{bf}, the constant heating powers $P_{\mathrm{const},i}$, $i = 1, 2$, and all the quasiparticle powers $P_{\mathrm{qp},i}$, $i \in \{1, 2, 1s, 2s\}$ are neglected. The parameters of the NIS junction are $\Delta = 230$ μeV, $\gamma = 5.8 \times 10^{-4}$, and $R_T = 30.7$ kΩ. The island volume is $\Omega = 3.2 \times 0.2 \times 0.02$ μm^3. These parameters are the same as in the experimental 20-cm sample in Sec. 5.2.

Since there are no constant heat leaks in this simulation, very low temperatures can be obtained. Furthermore, the island temperatures at $V = 0$ correspond to the phonon bath temperatures T_0. The temperature of the island 2 follows that of the island 1 very closely at $T_0 = 100$ mK, which shows the domination of the photonic heat conduction over the other heat currents.

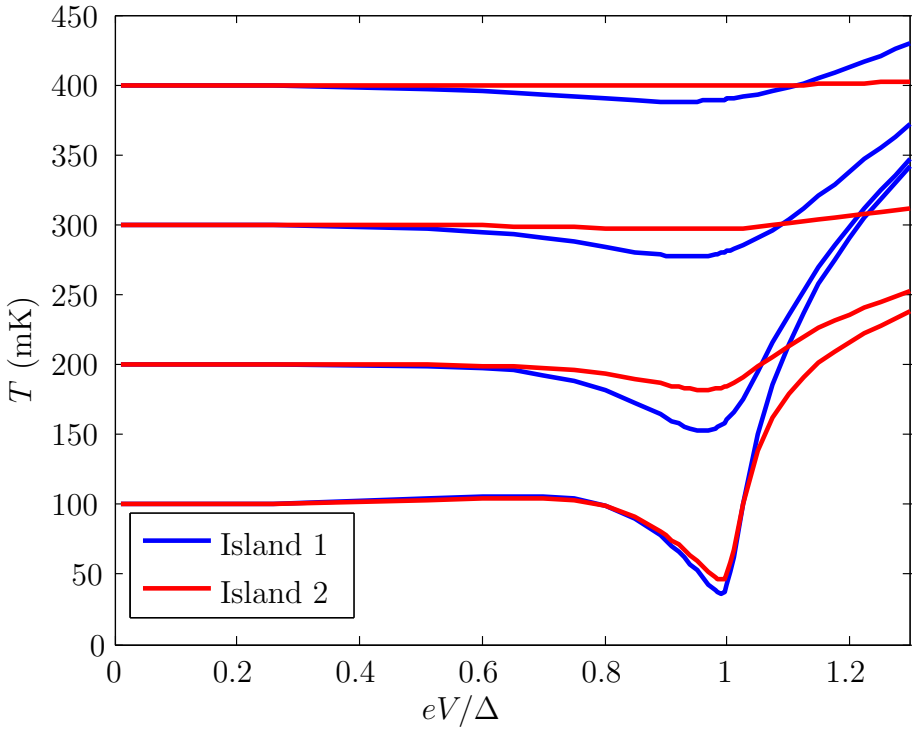

Figure 24: Examples of simulated island temperature curves in case of ideal photonic heat conduction at the quantum limit. Here, we neglect thermometer powers $P_{\mathrm{therm},i}$, $i = 1, 2$, constant heating $P_{\mathrm{const},i}$, $i = 1, 2$, all quasiparticle powers $P_{\mathrm{qp},i}$, $i \in \{1, 2, 1s, 2s\}$, and backflow power P_{bf}. The used parameters are $\Delta = 230$ μeV, $\gamma = 5.8 \times 10^{-4}$, $R_T = 30.7$ kΩ, $\Omega = 3.2 \times 0.2 \times 0.02$ μm^3.

4 Sample fabrication and measurement setups

The samples are fabricated in Micronova cleanroom facilities using processes described in this chapter. The samples for the heat conductance measurements contain NIS nanostructures whereas there are no nanostructures in the control samples. The fabrication processes consist of several steps, which can be varied in order to obtain different kind of samples. In addition, the measurement setups are presented in this chapter. The samples with the nanostructures are measured at sub-kelvin temperatures, and the control samples at 4 K.

4.1 Control samples

The control samples are fabricated on commercial 4-inch silicon wafers of a thickness of 0.6 mm. The wafer contains a silicon oxide layer of a thickness of 300 nm. The fabrication process starts with covering the silicon wafer with 200 nm of Nb. The next step is predicing. The wafer is covered with a resist layer in order to protect the Nb layer. The predicing is done by cutting the wafer half way from the back side. This enables processing several samples at the same time and afterwards dicing the wafer accurately to individual chips.

The next step is optical lithography with a mask aligner. Prior to the mask aligner the wafer is primed with hexamethyldisilazane (HMDS) chemical and covered with AZ5214E resist at 4000 rpm resulting in 1.4-μm layer thickness. We use a commercial soda lime mask in hard contact lithography. A photo resist is a material consisting of polymer chains. The solubility of the resist can be controlled by exposing it to ultraviolet (UV) light. Depending on the resist used, the exposed resist becomes either cross linked and, therefore, insoluble whereas the unexposed resist remains soluble, or the exposed resist becomes soluble if the UV light breaks the cross links of an otherwise insoluble resist. The AZ5214E resist can be used either way. After the exposure, we use image reversal bake at 120 ℃ followed by a flood exposure with the mask aligner. As a consequence, the solubility of the resist is reversed and the exposed resist is insoluble. After that the unexposed resist is removed with AZ351B developer in 40 s.

The next step is etching of Nb using reactive-ion etching (RIE). The etching time is 3 min, and the gas flows in the etching chamber are 20 standard cubic centimeters per minute (sccm) of SF_6 and 10 sccm of Ar. The bias voltage is approximately 330 V.

After the Nb etching, the rest of the resist needs to be removed and the sample cleaned. The resist is removed with remover PG, NEP, or acetone. After that the sample is cleaned with RIE where organic residues are etched with Ar (25 sccm) in 1 min with a bias voltage of 370 V.

4.2 Samples for heat conductance measurements

The samples for the heat conductance measurements are fabricated out of Al. The processing of the Al samples starts with optical lithography. The lithography process is similar to the one used for the control samples. The wafer is primed with HMDS, covered with resist, exposed with a mask aligner, and developed. After that the wafer is cleaned with RIE using oxygen descum process. The next step is evaporation of Al. The thickness of the Al layer is 200 nm. On top of the Al layer, we evaporate 3 nm of Ti and 5 nm of Au in order to prevent oxidation of the Al. Acetone is used in the lift-off after the evaporation. After that the wafer is prediced and cleaned with acetone and isopropyl alcohol (IPA).

The small structures containing NIS junctions are fabricated using electron-beam lithography (EBL). The EBL resist consists of three layers. The first two are MMA(8.5)MAA EL 11 copolymer spun at 2500 rpm. The copolymer consists of methyl methacrylate (MMA) and methacrylic acid (MAA) components in ethyl lactate (EL) solvent. The topmost layer is polymethyl methacrylate (PMMA) with 4 % of anisole (A4) spun at 2500 rpm. After each layer, the wafer is baked at 170 ℃ for 1 min. The mask for the structures is written with EBL using a 100-kV acceleration voltage, a 200-μm aperture and a 1-nA current. The dose for the patterns is 650 $\mu C/cm^2$. In addition to the actual patterns, shadow patterns are also written in order to achieve undercut. The dose for the shadow patterns is 160 $\mu C/cm^2$, and the aperture is 200 μm. The actual and shadow patterns overlap. The development is performed in three steps: first methyl isobutyl ketone (MIBK):IPA 1:3 developer, second methyl glycol:methanol 1:2, and third IPA. The development time is 20 s in the first two steps. The cleaning with IPA is also performed in 20 s.

After the development, the sample is cleaned with Ar plasma (5 min, 2×10^{-6} mbar). This allows us to obtain good electrical contacts between the large patterns produced with optical lithography and the small ones produced with EBL. The Ar plasma cleaning is performed in the same vacuum chamber as the following metal evaporation. We use three-angle evaporation in order to obtain both NIS tunnel junctions and NS contacts. The first layer is of Al (20 nm, -23°), after which it is oxidised (O_2, 9 mbar, 5 min). The second layer is of AuPd (20 nm, +24°), and the third layer of Al (100 nm, −7°). The evaporation rate is between 1 and 2 Å/s, and the pressure between 1×10^{-7} and 2×10^{-7} mbar. Lift-off is performed with acetone.

The Al samples contain two normal-metal islands with four NIS junctions which are used for dc measurements. In addition, the islands are connected to the center conductor and to the ground plane by NS contacts without an insulating oxide layer, which is the reason for using three-angle evaporation instead of two-angle evaporation. Images of a normal-metal island and NIS junctions are shown in Fig. 25.

4.3 Variations to the basic processes

Several variations to the basic processes described above are used. The first samples are fabricated using a laser writer instead of a mask aligner with a mask. The advantage of the laser writer is the fact that it is fast in fabricating a few test samples. However, if more samples are required, the mask aligner is significantly faster.

If no EBL patterns are to be made, the wafer can be diced to small chips after spinning the photo resist but before optical lithography. Here, the alignment can be carried out using the chip corners.

In addition, several changes to the fabrication parameters such as development and etching times, and the thicknesses of the metal layers are implemented. The lift off is also tested with different chemicals (PG, NEP, acetone).

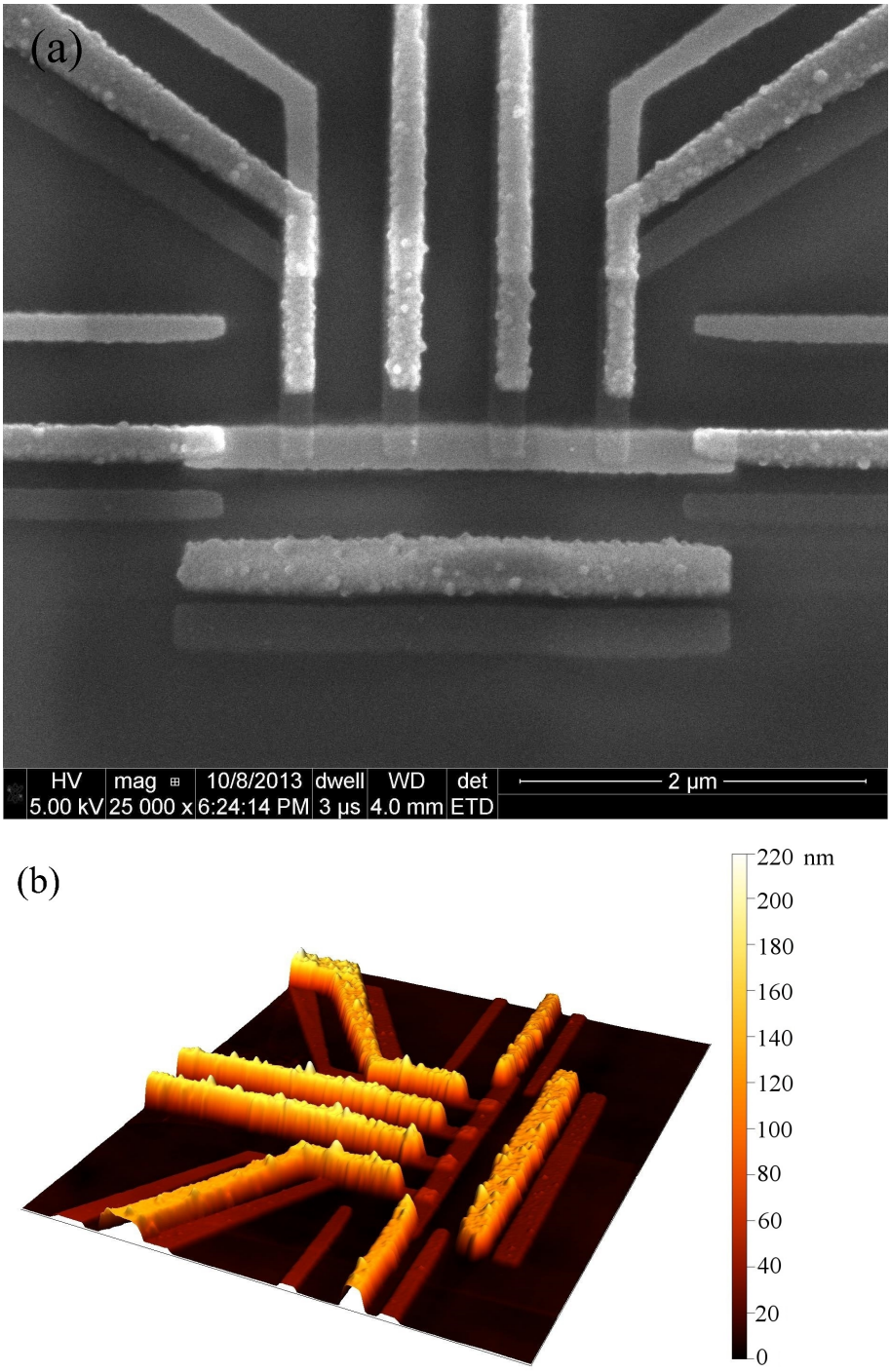

Figure 25: (a) SEM micrograph of a normal-metal island with four NIS junctions and (b) AFM micrograph of the same device. The left end of the island is connected to the center conductor and the right end to the ground plane by NS contacts. There are excess unused lines due to the three-angle evaporation.

4.4 Sample holder

The samples are placed on a copper sample holder covered with a 0.5-μm gold layer. Copper is chosen for its good thermal conductivity at low temperatures. The purpose of the gold layer is to prevent oxidation and, thus, to enable good thermal contact. The sample holder is presented in Fig. 26, and it is designed with Solid Edge software.

The sample holder also contains a printed circuit board (PCB) to which the sample is connected by aluminium bond wires. The surface of the sample and that of the PCB are at the same level. The PCB is fabricated out of glass-reinforced epoxy laminate FR4, which has a thickness of 1.6 mm. The metal leads are fabricated out of a 35-μm copper layer covered with a thin layer of silver. Both sides of the PCB are metallised, and they are connected by vias. The PCB is designed with Eagle software, and it is fabricated by a commercial company.

Surface-mount resistors can be connected to the dc lines. The RF lines are attached to the PCB with SMA connectors.

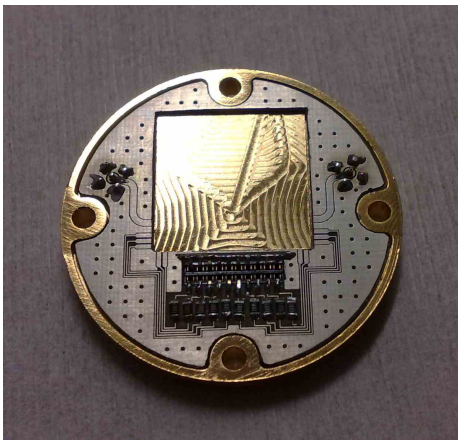

Figure 26: Sample holder contains a PCB with surface-mount resistors, and dc and rf connectors. The sample holder in this figure is designed for samples with a size of 2×2 cm^2. The sample can be placed to the square region in the middle of the sample holder.

4.5 Control measurements at 4 kelvin

Scattering parameter measurements are carried out at a 4-K bath temperature, which is achieved using liquid helium bath. The helium is in its most common isotope ^{4}He, and it is stored in a dewar shown in Fig. 27(a). The measurements are performed with a VNA to which the sample is connected by coaxial cables. Here, the VNA measures both the amplitude and the phase of the signal. No attenuators are used. The sample is mounted to a dipstick containing the necessary measurement cables, and the dipstick is dipped into the dewar. The dipstick is shown in Fig. 27(b).

The samples used in these control measurements at 4 K are fabricated out of Nb, which has a critical temperature of 9.25 K [50]. The Al samples cannot be used since the transition to the superconducting state occurs at a temperature of 1.2 K [50].

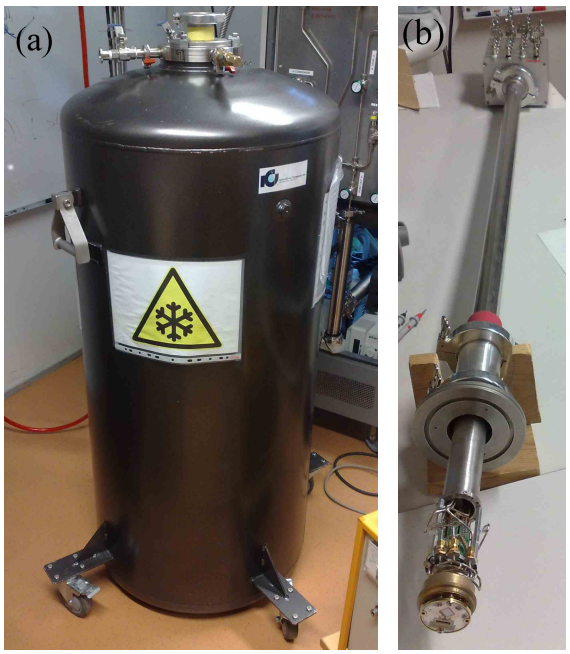

Figure 27: (a) Dewar containing liquid helium. (b) A dipstick used for measurements at 4 K. A sample holder and a sample are visible at the end of the dipstick since a protecting cover is not attached here.

4.6 Sub-kelvin measurements

A BlueFors dry dilution refrigerator is employed for all measurements at sub-kelvin phonon bath temperatures. The cooling mechanism of a dilution refrigerator is based on the finite solubility of ^{3}He in ^{4}He at zero temperature [33]. This is due to the fact that ^{3}He is fermionic and ^{4}He bosonic [33]. The dry dilution refrigerator and some measurement instruments are shown in Fig. 28(a), and the cryostat without the vacuum chamber is shown in Fig. 28(b). The dc lines are made of thermo coax cables. Furthermore, an optoisolator is used to reduce noise due to ground loops.

The principle of the measurement scheme is presented in Fig. 29. The temperatures of both normal-metal islands are measured by applying a bias current and observing the voltage across an SINIS structure. The bias current is obtained by setting the sample in series with a 12-GΩ resistor and connecting it to a voltage source. The voltage is measured with a voltage amplifier and an oscilloscope. The temperature control is obtained by sweeping a voltage across an SINIS structure. The sweeping time is 1 min. In addition, the cur-

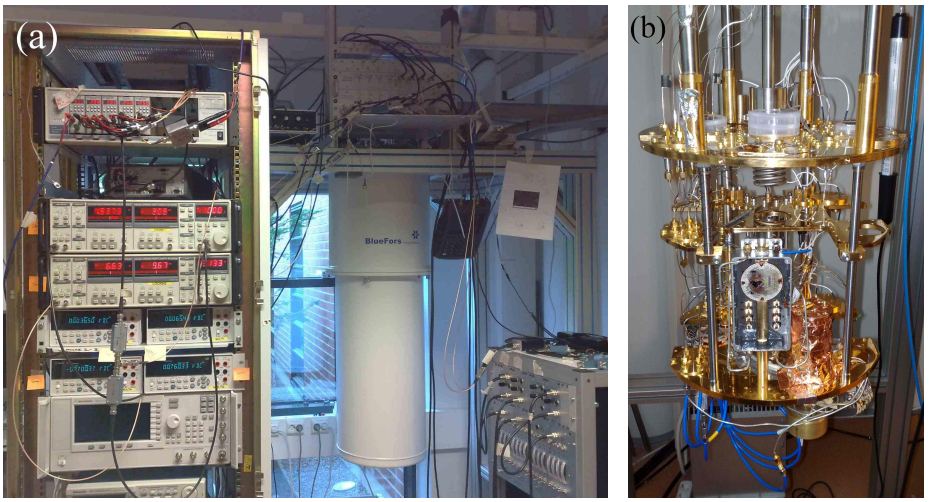

Figure 28: (a) BlueFors dry dilution refrigerator is used for sub-kelvin measurements. The sample is inside the white vacuum chamber near the center of the figure. Part of the measurement electronics is visible on the left. (b) The dry dilution refrigerator without the vacuum chamber. The sample is in the middle of the figure attached to a sample holder in an opened radiation shield. The lowest plate reaches temperatures below 10 mK. Some heat exchangers and measurement cables are also visible.

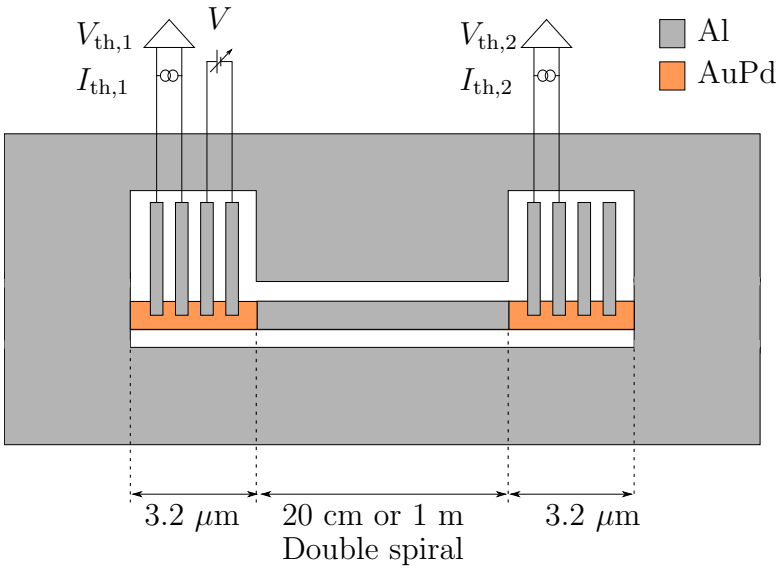

Figure 29: Measurement setup used at sub-kelvin temperatures. The island temperatures are obtained by measuring the voltages $V_{\mathrm{th,\,i}}$, $i = 1, 2$, across an SINIS structure with bias currents $I_{\mathrm{th},i}$. The temperature of the island 1 is controlled by varying the voltage V. The normal-metal islands are connected to the center conductor and to the ground by NS contacts.

rent used for temperature control is also measured. The two unused dc lines to the NIS junctions are left floating.

5 Experimental results

The experimental results on the control measurements at 4 K and on the photonic heat conduction over macroscopic distances at sub-kelvin temperatures are presented in this chapter. The measurement results are analysed and compared with the simulations. The scattering parameter measurements of the control samples characterise the quality of the CPW, and the thermometry at sub-kelvin temperatures enables the observation of heat conduction between the two normal-metal islands.

5.1 Scattering parameter

The frequency responses of the fabricated control samples are measured with a VNA. There are no resistors in the cavities, and therefore, high Q factors can be measured. The coupling capacitors allow voltages at the ends of the resonators which have a length $s \approx \lambda/2$. This relation is exact at the limit $C_\kappa \to 0$, in which case no currents can flow at the ends of the lines. Both 20-cm and 1-m resonators are measured.

The loaded Q factors of different resonance peaks are extracted from the experimental data by fitting a Lorentzian curve and by using the phase–frequency fit as shown in Sec. 3.5.3. The results for a 20-cm sample with 8+8 finger coupling capacitors of 200-μm finger length are presented in Fig. 30. The Lorentzian fit and the phase–frequency fit yield quantitatively similar results. The figure also shows a fitting curve based on the RLC model, where α and C_κ are used as fitting parameters in Eq. (158). The values extracted with the RLC model are shown in Table 2.

The scattering parameters can be calculated as a function of frequency using the ABCD matrix method as described in Sec. 3.5.1. The simulated curve is presented along with the measured data in Fig. 31. The simulation is performed using α and C_κ extracted from the RLC approximation and data in Fig. 30. The ABCD matrix simulation describes the measured scattering parameter data rather well although there are some unexplained features at 0.9, 1.2 and 1.5 GHz. In addition, the simulation and the measured data start to deviate more above 2 GHz. Nevertheless, all the features are significantly weaker than the resonance peaks.

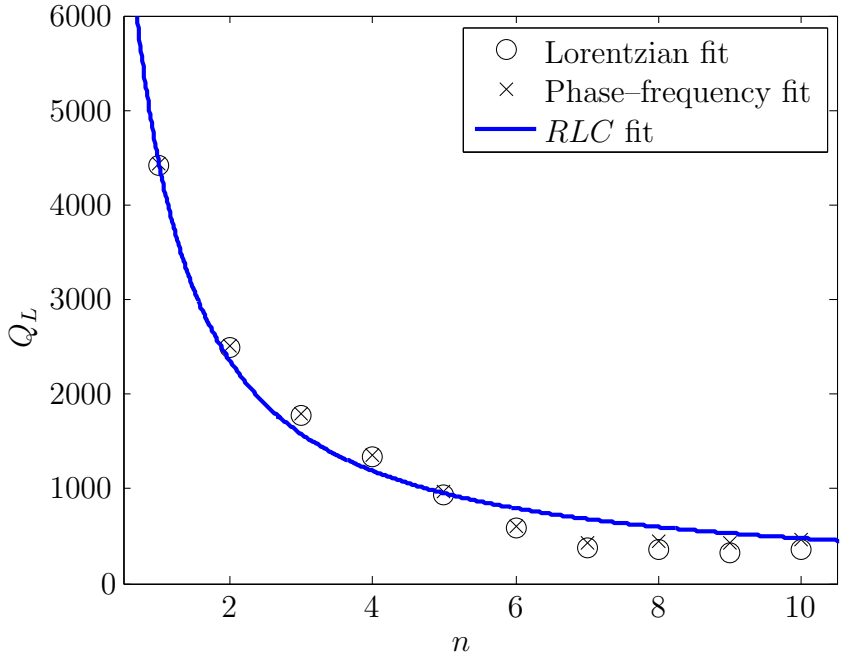

Figure 30: Loaded quality factor Q_L of a 20-cm Nb resonator as a function of the mode number n. The quality factor is determined from experimental data using two different methods: Lorentzian fit and phase–frequency fit. The simulation result (solid line) is obtained using α and C_κ as fitting parameters in Eq. (158) of the RLC model. Here, n is a continuous variable although in reality it can obtain only integer values. The device has 8+8 interdigital coupling capacitors with 200 μm fingers.

The effect of the coupling capacitances is studied by comparing two 20-cm samples with different coupling capacitors. The studied capacitors are 2+2 fingers with 100 μm length and the 8+8 fingers with 200 μm length. The resulting experimentally obtained loaded quality factors are presented in Fig. 32. Here, the Q_L values are calculated as averages of the values obtained with the Lorentzian fit and and the phase–frequency fit methods. The two methods are both considered reliable, and calculating an average of two differently determined values reduces the uncertainty. Curves fitted to the RLC model are also shown in Fig. 32, and the obtained fitting parameters and calculated internal quality factors, Q_{int}, are presented in Table 2. The fitted value for C_κ of the 8+8 sample is 120.2 fF, which is approximately 10 % less than the simulated value in Table 1. The 2+2 sample has a fitted C_κ of 26.3 fF whereas the simulated value is 13.3 fF. Both samples have Q_{int} higher than 5×10^4.

Table 2: Extracted parameters α and C_κ and internal quality factors Q_{int} for 20-cm samples with different coupling capacitors.

Capacitance structure	C_κ (fF)	α (10^{-4} m^{-1})	Q_{int}
100 μm finger, 2+2	26.3	1.15	7.09×10^4
200 μm finger, 8+8	120.2	1.51	5.38×10^4

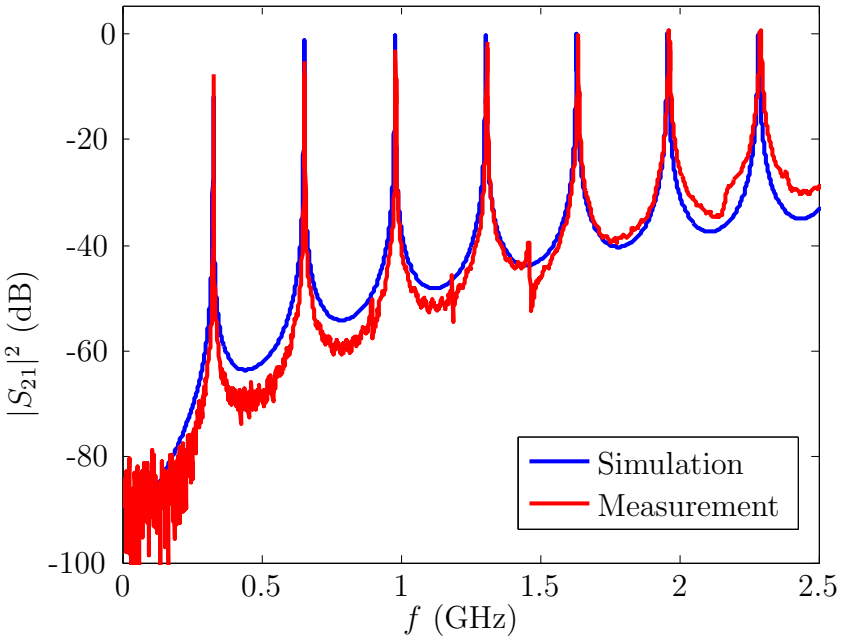

Figure 31: Transmission coefficient as a function of frequency for a 20-cm Nb resonator with 8+8 interdigital coupling capacitors. The simulation is performed using the ABCD matrix method presented in Sec. 3.5.1. The values for α and C_κ (see Table 2) are obtained from the fit shown in Fig. 30. The measured data is normalised by subtracting the scattering parameters of a transmission line which has an otherwise similar structure but no coupling capacitors.

The environment of the resonator also affects the reflection and transmission coefficients. This effect is studied by measuring a sample with and without an extra cover. The length of the resonator is 1 m, and it has 16+16 finger coupling capacitors with a finger length of 200 μm. Without the extra cover, the distance from the chip to a larger cover is more than 3 mm, and with the cover the distance is reduced to 2 mm. The extra cover is made of brass.

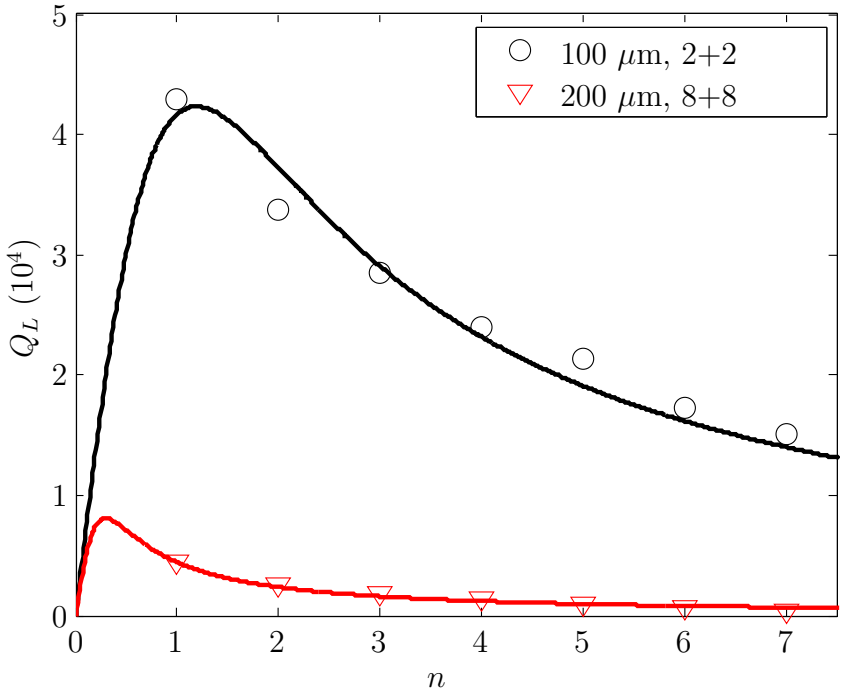

Figure 32: Loaded quality factor Q_L of a 20-cm resonator as a function of the resonance number n for two different coupling capacitors. The quality factors are obtained as averages of the Lorentzian fit and the phase–frequency fit results. The solid lines are calculated using Eq. (158), where C_κ and α are treated as fitting parameters.

The Q_L values of different modes of the 1-m sample are obtained similarly as for the 20-cm sample, and the values are presented in Fig. 33. Curves based on the *RLC* model are fitted to the measured Q_L data. Here, α and C_κ are used as fitting parameters as above, and their values are presented together with the extracted Q_{int} in Table 3. In the measurements without the cover, the fitted C_κ is 297.2 fF, which is approximately 5 % higher than the simulated value. The fitted curve follows the measured values quite well.

The same 1-m sample is measured with the extra cover, and the results are also presented in Fig. 33 and Table 3. The effect of the cover depends on the mode number n. With the extra cover, the Q_L of the first mode is reduced whereas it is increased for the other odd modes. There is only a minute difference between the Q_L values measured with and without the cover for the first few even modes, but for $n > 8$, the Q_L factor is increased. The even modes with mode number n have lower Q_L values than the odd modes with $n \pm 1$. This is assumed to be caused by the fact that the even modes have anti-nodes

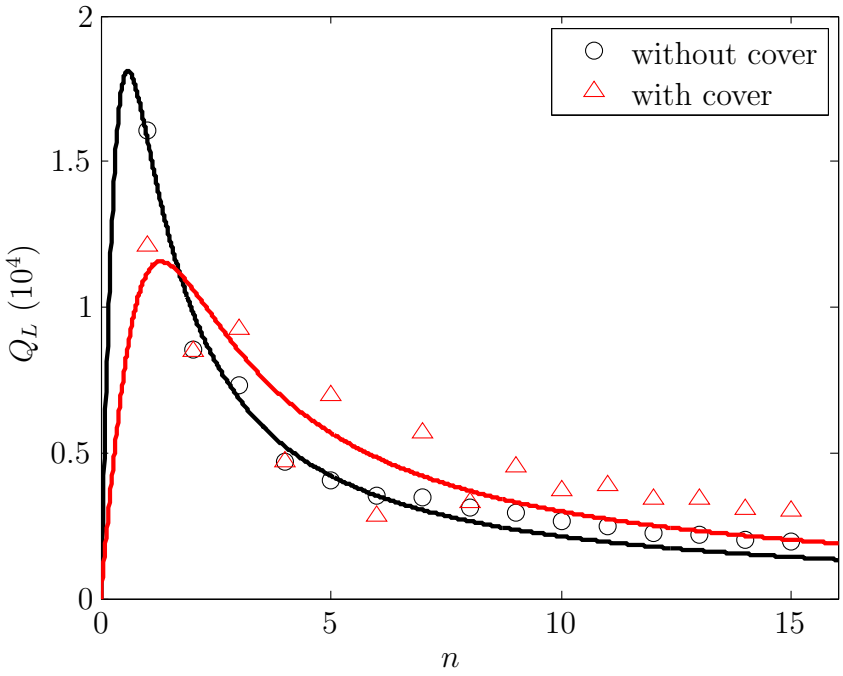

Figure 33: Loaded quality factor Q_L of a 1-m resonator as a function of the mode number n. The coupling capacitors are 16+16 finger capacitors with a length of 200 μm. The measurements are performed with and without an extra cover. The solid lines are fitted to the measurement data according to Eq. (158).

of the voltage and the odd modes nodes at the center of the resonator. However, the exact mechanism is somewhat unclear, and the analysis of it requires full simulation of the double spiral CPW system with and without the cover.

The *RLC* model does not consider the double spiral structure and cannot describe the differences between the even and odd modes. Therefore, the agreement between the fit and the measurements is not very good. The fit-

Table 3: Fitting parameters α and C_κ and internal quality factors Q_{int} for a 1-m sample with and without an extra cover. The sample has 16+16 finger coupling capacitors with a finger length of 200 μm.

Sample	C_κ (fF)	α (10^{-5} m^{-1})	Q_{int}
without cover	297.2	2.56	6.12×10^4
with cover	249.2	8.94	1.76×10^4

ted value of C_κ is 249.2 fF with the cover. However, the actual capacitance stays approximately the same as without the cover since the distance to the cover is significantly longer than the finger separation. Without the cover $Q_{\rm int} = 6.12 \times 10^4$, which is close to the values measured for the 20-cm samples. Since the simple model does not describe the system with the cover accurately, the calculated $Q_{\rm int} = 1.76 \times 10^4$ can be considered as an order of magnitude estimate.

The above-discussed samples, for which the scattering parameters are measured, are fabricated with Nb. Similar Al samples are assumed to have somewhat lower Q values due to the thin Au layer deposited on top of the Al to prevent oxidation. The Nb samples are also non-ideal since there is a native oxide layer on the surface. The actual samples used in the thermometry contain normal-metal resistors unlike the control samples discussed in this section. The samples with normal-metal resistors connecting the center conductor to the ground plane have significantly lower Q factor. In an ideal case, the transmission probability is 1, and no resonance can be observed. The high $Q_{\rm int}$ values measured in this section confirm the suitability of the sample structure for the heat conductance measurements.

5.2 Heat conduction over 20-cm distance

The temperatures of two normal-metal resistors terminating a 20-cm-long CPW transmission line are measured using the measurement setup presented in Fig. 29. The thermal model of the system is presented in Sec. 2.12. The temperatures of both normal-metal islands are measured and the temperature of the island 1 is controlled with NIS refrigeration and heating as discussed in Sec. 2.9. The heat conduction results in temperature changes on the island 2. The refrigeration is obtained by voltage biasing one pair of junctions, and the thermometry by current biasing another pair.

5.2.1 Junction properties

The properties of the NIS junctions are presented in Table 4. There are four NIS junctions in the island on the left and four on the right denoted by Li and R$i, i = 1, 2, 3, 4$, respectively. The asymptotic and gap resistances are measured pairwise with a current bias, while the other junctions are floating. The junctions have very high resistance in the gap. The asymptotic

Table 4: Measured junction properties of the 20-cm sample. The smearing parameter for the superconductor density of states, γ, is obtained as a ratio of the asymptotic resistance R_{asymp} and the resistance inside the gap R_{gap}. Here, L denotes the island on the left and R on the right in Fig. 16.

Junction	R_{asymp} (kΩ)	R_{gap} (MΩ)	γ
L1	12.3	0.022	3.1×10^{-1}
L2	3.4	–	–
L3	23.0	0.882	2.6×10^{-2}
L4	49.4	139	3.5×10^{-4}
R1	26.0	3.56	7.3×10^{-3}
R2	4.6	0.011	4.3×10^{-1}
R3	16.3	0.362	4.5×10^{-2}
R4	30.7	53.0	5.8×10^{-4}

resistances are measured at voltages above 1.5 mV, and the gap resistances at zero voltage. The junctions are not very uniform as asymptotic resistances of the functioning junctions vary between 16 and 50 kΩ. The junction R2 has a linear IV curve, and junctions R2 and L1 are of low quality as indicated by the large γ values in Table 4. These junctions show only weakly NIS features in their IV curves. A good junction has γ of the order of 10^{-4} or below. Nevertheless, junctions with $\gamma \approx 10^{-2}$ can be used for refrigeration and thermometry although the leakage current in the superconducting gap is larger.

At island 1, the temperature is controlled by NIS refrigeration. In these measurements, it is the island on the right and, consequently, the island 2 is on the left. The junction connections are presented in Table 5. The thermometer bias current is 50 pA for both islands. The current bias is obtained by applying a constant voltage over a 12-GΩ series resistance.

5.2.2 Superconducting gap

The superconducting gap Δ is extracted from measured IV curves. Examples of IV curves of NIS junctions at several phonon bath temperatures are shown in Fig. 34. These curves are measured over junctions R2 and R4 with voltage bias during the actual temperature measurements. Since the junction R2 has an almost linear IV, the figure shows essentially IV curves of a single NIS

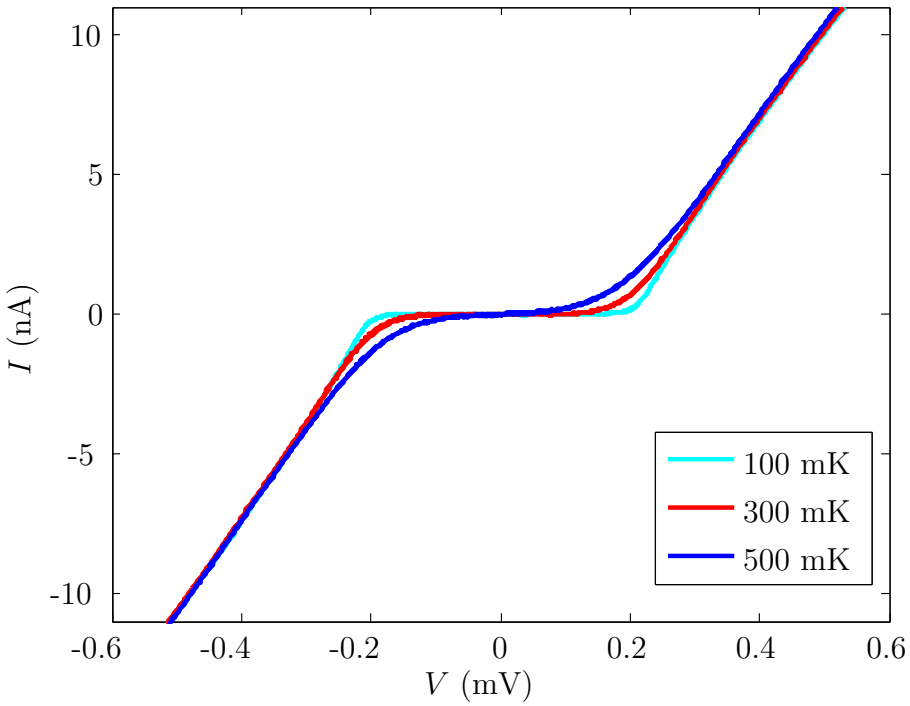

Figure 34: Measured current as a function of voltage through junctions R2 and R4 of the 20-cm sample at various phonon bath temperatures. Note that the junction R2 has an almost linear IV, and hence the measured data essentially represents the IV of junction R4. The voltage and current offsets of the measurement data have been subtracted.

junction R4. The same curves with normalised current and voltage are shown in Fig. 35. The value of the superconducting gap is used as a fitting parameter in Eq. (107), and it obtains a value $\Delta = 230$ μeV. The other parameters for R4 that are used in Eq. (107) are shown in Table 4. The electron temperature

Table 5: Connections of the pairs of junctions in the measurement of the 20-cm sample. The thermometry is performed using these connections as schematically presented in Fig. 29.

Connection	Junctions
Island 1, refrigeration	R2, R4
Island 1, thermometry	R1, R3
Island 2, thermometry	L3, L4
Island 2, floating	L1, L2

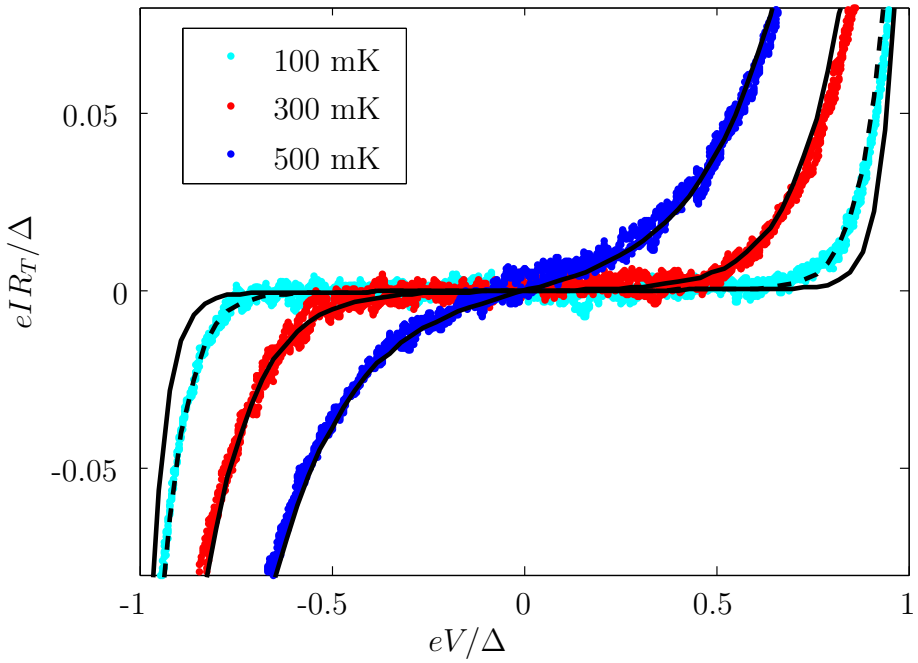

Figure 35: Measured current as a function of voltage through junctions R2 and R4 at various phonon bath temperatures. Only the junction R4 is a well-functioning NIS junction. The solid lines are calculated according to Eq. (107) at electron temperatures equal to the bath temperature using Δ as a fitting parameter. At low phonon bath temperatures, the electron temperature saturates. The dashed line is calculated for 150-mK electron temperature, and it closely follows the measured data for 100-mK bath temperature. The extracted value for the superconducting gap is $\Delta = 230$ μeV.

saturates at low phonon bath temperatures. According to the fit in Fig. 35, the electron temperature is 150 mK at $T_0 = 100$ mK. The subgap current of R4 as a function of voltage at a phonon bath temperature of 300 mK is shown in Fig. 36. The fitted curve follows the measured data reasonably well. The figure shows also the noise level of the current measurement.

5.2.3 Thermometer calibration

The thermometers based on NIS junctions need to be calibrated. The calibration is performed by measuring the voltage across a pair of junctions at various bath temperatures with a constant bias current. The calibration data for both islands is measured simultaneously.

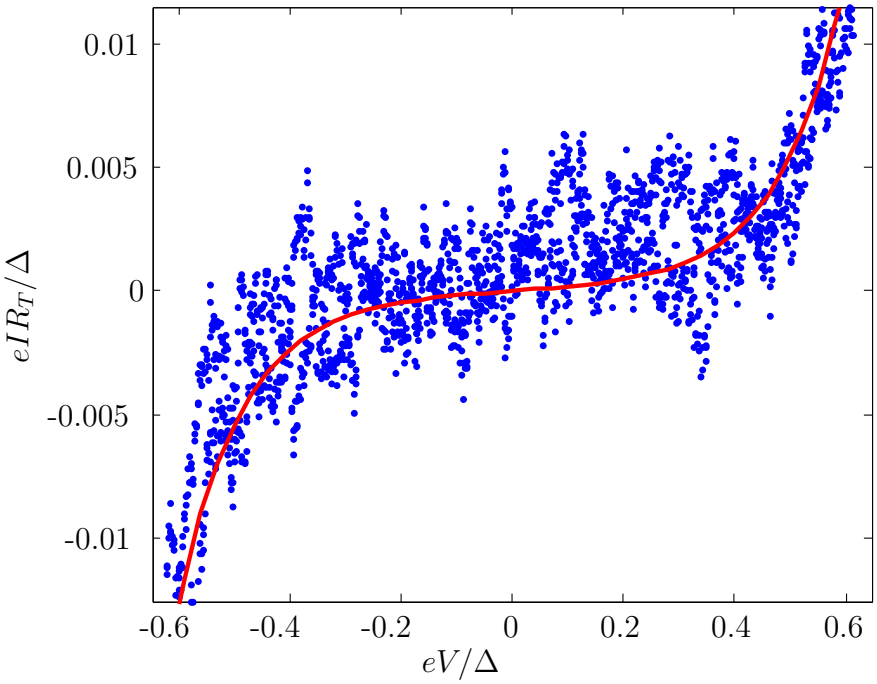

Figure 36: Measured subgap current as a function of voltage through an NIS junction R4 at a phonon bath temperature of 300 mK. The solid line is fitted using a parameter $\Delta = 230$ μeV. The current flows also through the junction R2, which is not taken into account in the curve.

The measured temperature calibration data is presented in Fig. 37 along with simulated curves and linear fits. The experimental data is plotted as a function of the phonon bath temperature, and the theoretical curves as functions of the electron temperature. The calibration is reliable at least in the region where the experimental and theoretical data agree, and the temperature response is linear. The parameters used in the simulations correspond to the measured values of the actual device. The volumes of the islands are $3.2 \times 0.25 \times 0.02$ μm^3, and the junction properties are presented in Table 4. The superconducting gap is $\Delta = 230$ μeV, as discussed above. The measured calibration points and the simulation results have a rather good agreement at temperatures above 200 mK. However, below 200 mK the measured voltages saturate due to heat leaks from a high-temperature environment and potentially due to low junction quality. The voltage saturates also in the case of an ideal NIS junction due to a finite bias current. The linear fit to the temperature calibration data is used to convert the measured voltages to temperatures.

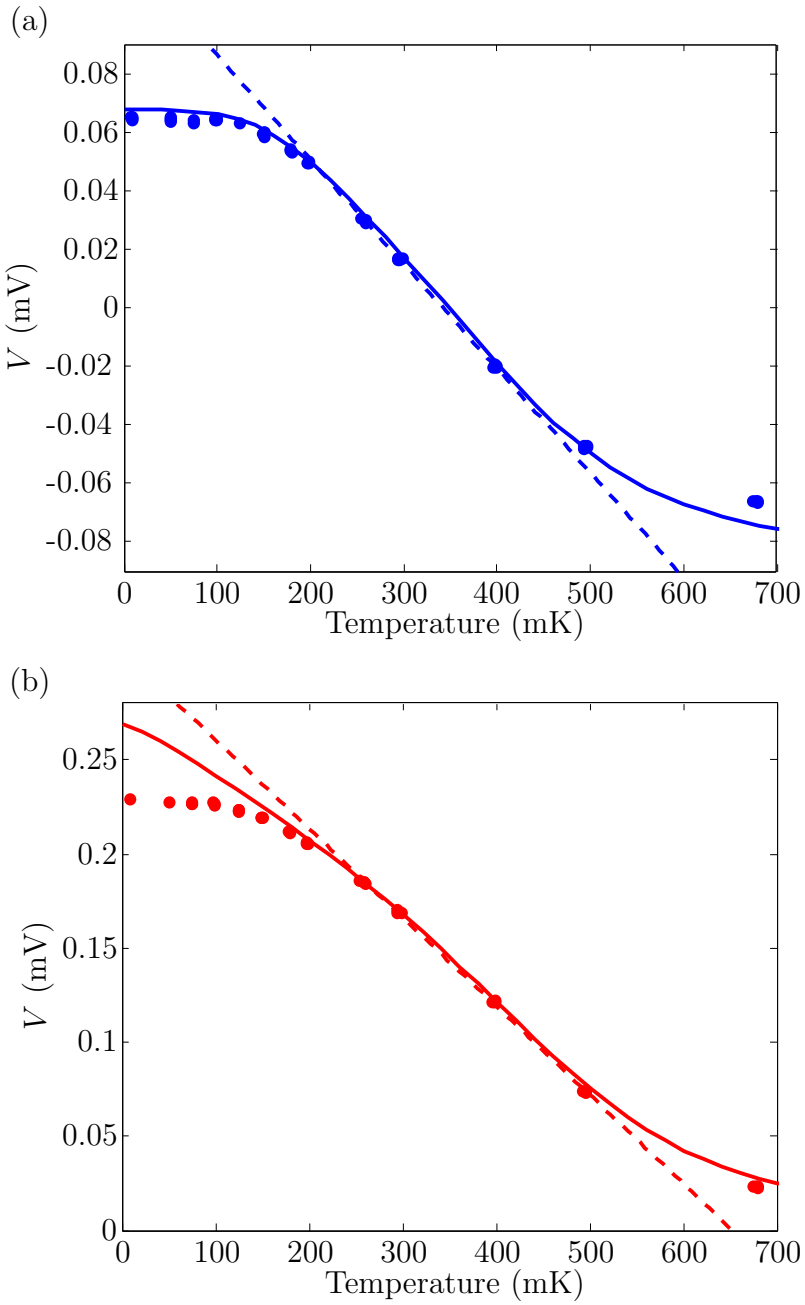

Figure 37: Measured temperature calibration voltages (dots) of (a) island 1 and (b) island 2 as functions of the bath temperature. The simulation curves (solid lines) are calculated numerically as functions of electron temperature using Eq. (107) with parameters extracted from independent experiments. The simulation curves are shifted by a constant voltage offset. The thermometer junctions for the island 1 are R1 and R3, and for the island 2 L3 and L4. Their properties are shown in Table 4. The superconducting gap is $\Delta = 230$ μeV. Dashed lines are linear fits at temperatures between 300 and 400 mK, and they are used for the temperature conversion.

5.2.4 Thermometry

Temperatures of both islands are shown in Fig. 38 as functions of the bias voltage V of the refrigerator junction pair at the island 1. The temperature minima occur at $V \approx \pm\Delta/e$. At larger absolute voltages the islands are heated, and at smaller voltages, the temperatures are nearly constant. The temperature variations are larger at low phonon bath temperatures. The data at $V = 0$ is used for the temperature calibration. The island temperatures at $V = 0$ do not reach very low values due to heat leaks and the loss of thermometer sensitivity.

We define a temperature change $\Delta T_{i,\mathrm{cool}} = \min_V[T_i(V)] - T_i(0)$, at island $i = 1, 2$, as the difference between the temperature minimised over V and the temperature at $V = 0$, as presented in Fig. 39. The minimum temperatures of both islands are obtained at the same voltage. At higher absolute voltages, the islands are heated, and we define another temperature change $\Delta T_{\mathrm{i,heat}} = T_i(V_{\mathrm{heat}}) - T_i(0)$ as the difference between the temperature at $|V_{\mathrm{heat}}| = 1.3\Delta/e$ and the temperature at $V = 0$. The definition of $\Delta T_{1,\mathrm{heat}}$ is also presented in Fig. 39. Other values of the heating voltage V_{heat} can be used as well. Since the temperature curves are symmetric with respect to voltage, the values of $\Delta T_{i,\mathrm{cool}}$ and $\Delta T_{i,\mathrm{heat}}$ are calculated as averages of the values at positive and negative voltages.

The temperature changes, $\Delta T_{i,\mathrm{cool}}$, and their ratio are presented in Fig. 40. At high temperatures, hardly any cooling is observed in either of the islands. The temperature change of island 1, $\Delta T_{1,\mathrm{cool}}$, reaches its minimum of -8 mK at $T_0 = 180$ mK, and that of island 2, $\Delta T_{2,\mathrm{cool}}$, its minimum of -2 mK at $T_0 = 130$ mK. The absolute value of the temperature change of island 1 decreases with decreasing bath temperature below $T_0 = 180$ mK, and it saturates below 80 mK bath temperatures. The temperature change of island 2 saturates as well. The temperature data is most reliable between the bath temperatures of 250 and 450 mK due to the good agreement between the linear fit and the experiments in Fig. 37.

The island temperatures are simulated according to the thermal model presented in Sec. 2.12, and fitted curves are also shown in Fig. 40. The parameters used in the simulations are shown in Table 6. We neglect the thermometer powers $P_{\mathrm{therm},i}$, $i = 1, 2$. The quasiparticle heat conduction from one island to the other is also neglected. In contrast, the quasiparticle contribution from the normal-metal shadows is taken into account. The total volume of the

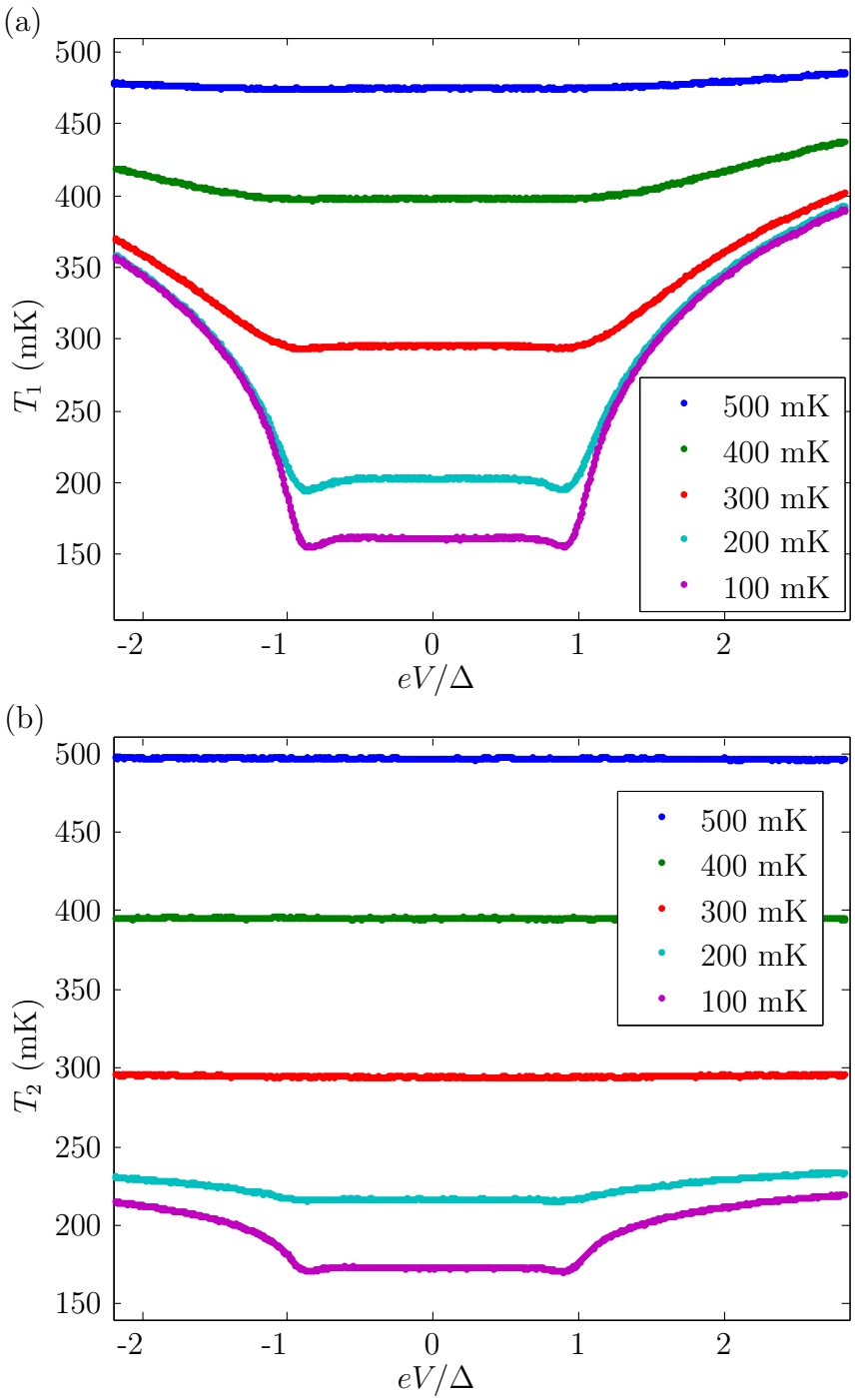

Figure 38: Measured island temperatures (a) T_1 and (b) T_2 at various phonon bath temperatures T_0 as functions of the refrigerator voltage V.

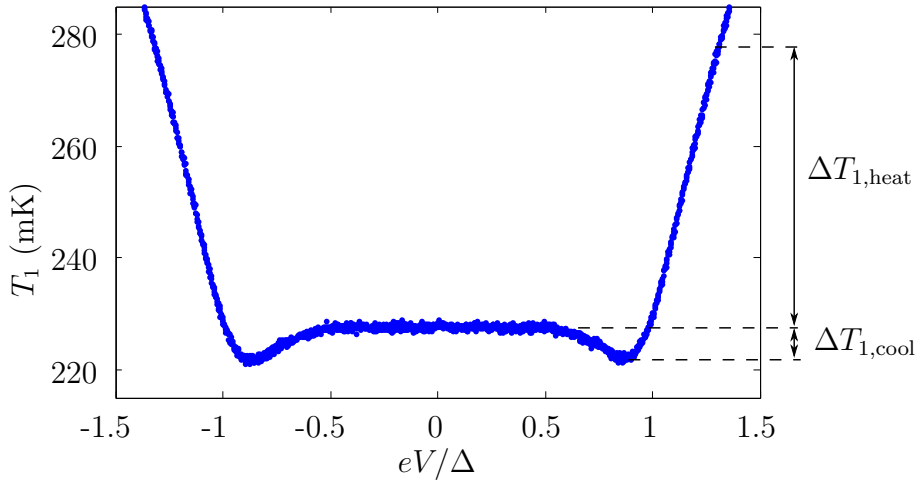

Figure 39: Definition of the island 1 temperature changes $\Delta T_{1,\mathrm{heat}}$ and $\Delta T_{1,\mathrm{cool}}$. Here, the temperature of island 1 is presented as a function of the refrigerator voltage. The voltage defining $\Delta T_{1,\mathrm{heat}}$ is chosen to $V_{\mathrm{heat}} = 1.3\Delta/e$.

evaporated AuPd within 50 μm distance from the actual normal-metal island is more than 1000 times larger than the island volume, as can be seen in Fig. 17. Nevertheless, the normal-metal forms only a thin layer on a thick superconductor, and therefore, its contribution is significantly smaller than that of a normal-metal of the same size on a silicon chip.

The simulated curves are adjusted to agree with the measurements by varying parameters $P_{\mathrm{const},i}$, ν, and β. The heating powers of the islands, $P_{\mathrm{const},i}$, are set be equal due to symmetry. The powers introduced by the thermometers $P_{\mathrm{therm},i}$ are assumed to be negligible. The fitted curves in Fig. 40 qualitatively agree with the measurements. However, there is a slight quantitative mismatch between the experiments and the simulations. The experimental temperature change of the island 1 reaches its minimum value at a higher phonon bath temperature than the simulated one, and it obtains higher values at $T_0 < 150$ mK. Quantitatively, the experimental temperature change of the island 2 is rather close to the simulated one. The temperature data may not be very reliable below the bath temperatures of 200 mK due to the thermometer voltage saturation.

The ratio of the temperature changes, $\Delta T_{2,\mathrm{cool}}/\Delta T_{1,\mathrm{cool}}$, approaches zero as the bath temperature is increased above 400 mK. However, the error of the ratio increases due to the increasing relative errors of $\Delta T_{1,\mathrm{cool}}$ and $\Delta T_{2,\mathrm{cool}}$.

Table 6: Simulation parameters for the 20-cm sample. Here, s, Ω, A_l, and l are fixed by the realised sample geometry, and γ, Δ, R_1, R_2, R_T are measured values independent of the other measurements. We obtain C_l from Comsol simulations, and calculate L_l using Eq. (133). Parameters Σ_{AuPd} and ρ are from Refs. [6] and [38], respectively. We use β, ν and $P_{\mathrm{const},1} = P_{\mathrm{const},2}$ as fitting parameters. The same value of ν is also used for the 1-m sample fitting.

Quantity	Symbol	Value	Unit
Distance	s	0.1926	m
Inductance per unit length	L_l	4.1×10^{-7}	Hm^{-1}
Capacitance per unit length	C_l	1.5×10^{-10}	Fm^{-1}
Dynes parameter	γ	5.8×10^{-4}	
Island volume	Ω	$3.2 \times 0.25 \times 0.02$	$\mu\mathrm{m}^3$
Island 1 resistance	R_1	150	Ω
Island 2 resistance	R_2	150	Ω
Tunnelling resistance, junction R4	R_T	30.7	$\mathrm{k}\Omega$
Superconducting gap	Δ	230	$\mu\mathrm{eV}$
Material parameter for AuPd	Σ_{AuPd}	3.0×10^9	$\mathrm{WK}^{-5}\mathrm{m}^{-3}$
Constant heat flow to island 1	$P_{\mathrm{const},1}$	3.5	fW
Constant heat flow to island 2	$P_{\mathrm{const},2}$	3.5	fW
Backflow coefficient	β	0.103	
Cross section of leads	A_l	200×100	nm^2
Length of leads	l	4	$\mu\mathrm{m}$
Resistivity of leads	ρ	1.5×10^{-8}	$\Omega\mathrm{m}$
Effective volume of extra blocks	ν	$6.5 \times \Omega$	

The ratio increases significantly with the temperature decreasing from 200 to 100 mK, which is a consequence of the photonic heat conduction dominating over the other thermal links. The ratio saturates below 100 mK. The fitted curve follows the experimental values rather accurately despite the quantitative mismatch in the $\Delta T_{i,\mathrm{cool}}$ results. There may be an error in both island temperatures by the same factor, which can explain the good agreement.

Heating of the islands is studied with the same methods as the cooling. The measurement results are presented in Fig. 41. Here, the temperature changes approach zero at high temperatures, and they increase with decreasing temperature. The maximum temperature change of island 1 is 110 mK, and that of island 2 is 28 mK. Since the temperature changes are significantly larger than in the cooling measurements, the signal-to-noise ratio is better

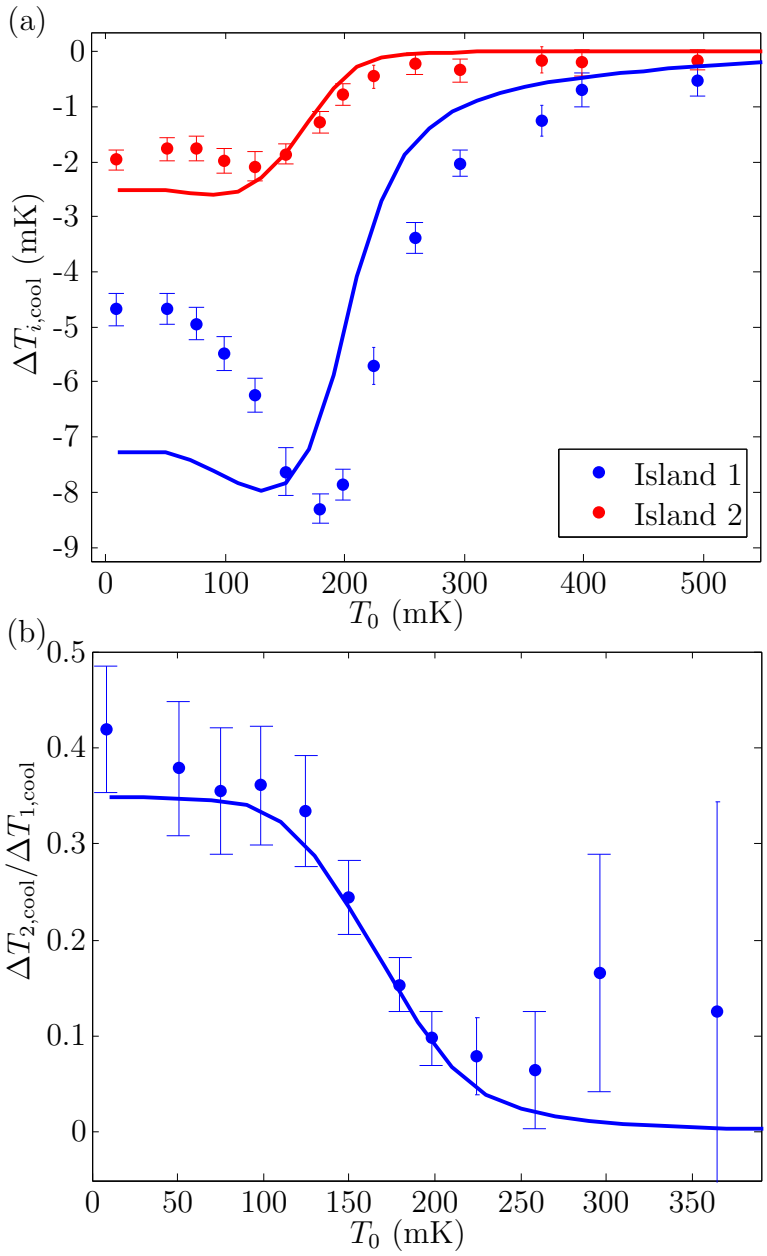

Figure 40: (a) Temperature changes $\Delta T_{i,\mathrm{cool}}$ for island $i = 1, 2$ as functions of the bath temperature T_0. (b) The ratio of the temperature changes $\Delta T_{2,\mathrm{cool}}/\Delta T_{1,\mathrm{cool}}$ as a function of T_0. The dots are experimental results with errorbars indicating the standard deviation of the measurement data, and the solid lines are fitted curves. The parameters for the fit curves are presented in Table 6.

and the results are more reliable. The ratio of the temperature changes, $\Delta T_{2,\mathrm{heat}}/\Delta T_{1,\mathrm{heat}}$, increases from 0 up to 0.25 as the bath temperature is decreased from 400 mK to 50 mK. The ratio saturates at low temperatures.

The simulated curves in Fig. 41 for the heating data are calculated using the same parameters as in the case of cooling. The parameters are presented in Table 6. The simulated and the experimental temperature changes $\Delta T_{i,\mathrm{heat}}$ are in a very good quantitative agreement. Therefore, the simulated ratio of the temperature changes is also in good agreement with the measurements. The simulated temperature changes have a significantly better agreement with the experiments in Fig. 41 than in Fig. 40 since the absolute temperature changes are larger and, therefore, they suffer less from the reduced sensitivity of the thermometry or from the inaccuracies in the simulations. A somewhat better agreement in the cooling results could be obtained if the simulation parameters were adjusted independently of the heating simulations.

The photonic heat transfer depends on the matching of the resistors and the transmission line as shown in Fig. 6. The normal-metal resistances are measured by applying a bias current through two junctions and measuring the voltage $V = RI$ from two other junctions. Here, R is the resistance of the normal metal between the junctions used in the voltage measurement, and I is the current. The total island resistances are calculated by combining the resistances of different segments of the islands and using their symmetry. The characteristic impedance is 52.4 Ω calculated from C_l and L_l given in Table 6 according to Eq. (29). The C_l value is obtained from Comsol simulations, and L_l is calculated according to Eq. (133). Thus, the ratio is $P_\Gamma/P_{\max} = 0.6$ for the 20-cm sample.

In summary, the experimental data in Figs. 40 and 41 corresponds relatively well to the thermal model. At low temperatures, the saturation of the island temperatures and the possible reduction in thermometer sensitivity limit the reliability of the experimental results. Nevertheless, the experimental data can also be explained below 200-mK bath temperatures especially in the case of heating. Therefore, the experimental data supports the theoretical model. The quantum of thermal conductance is not reached due to unmatching between the resistors and the transmission line. Nevertheless, the photonic heat conduction dominates the heat exchange between the two normal-metal islands.

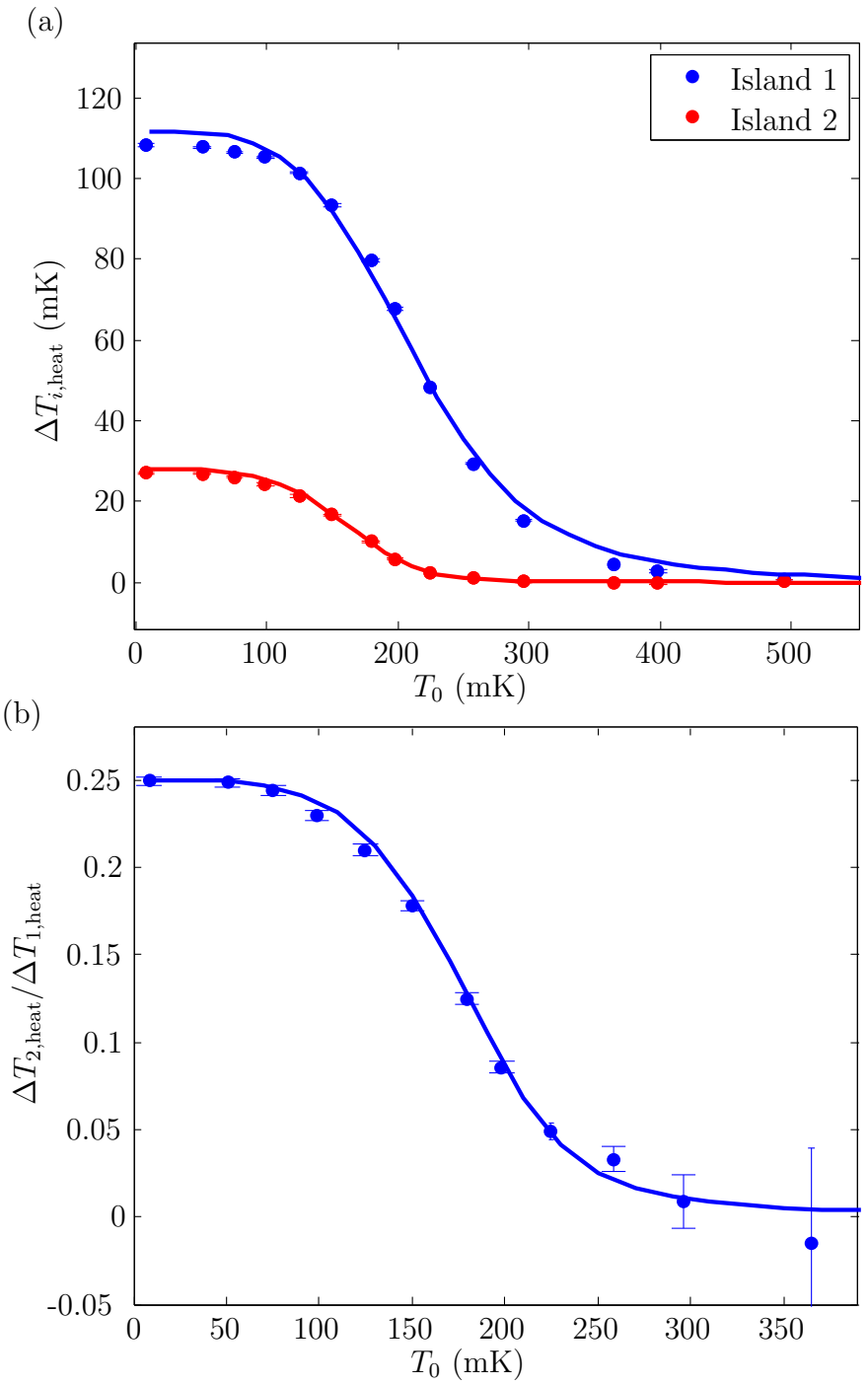

Figure 41: (a) Temperature changes $\Delta T_{i,\mathrm{heat}}$ for island $i = 1, 2$ as functions of bath temperature T_0. (b) The ratio of the temperature changes $\Delta T_{2,\mathrm{heat}}/\Delta T_{1,\mathrm{heat}}$ as a function of T_0. The dots are experimental results and the solid lines fitted curves. The errorbars indicate the standard deviation of the measurement data. The parameters for the fit curves are shown in Table 6.

5.3 Heat conduction over 1-m distance

A sample with a 1-m-long CPW is also measured according to the measurement scheme presented in Fig. 29 and analysed according to the thermal model presented in Sec. 2.12.

5.3.1 Junction properties and superconducting gap

The measured junction parameters are presented in Table 7. There is one shorted junction at the left island, L3, and one at the right island, R1. Junction R4 is of very low quality. The asymptotic resistances of the functioning junctions are significantly higher at the left island compared with the right island. At the right island, R_{asymp} ranges from 25 to 71 kΩ, and at the left from 237 to 343 kΩ. The smearing parameter γ is smaller in the left island.

The connections of the pairs of junctions are presented in Table 8. The right island is used as island 1 in the measurements, and therefore, the left island is the island 2. The measurement setup is shown in Fig. 29.

Table 7: Measured junction properties for the 1-m sample. The smearing parameter for the superconductor density of states is denoted by γ, the asymptotic resistance by R_{asymp} and the resistance inside the gap by R_{gap}. Here, L denotes the island on the left (island 2) and R on the right (island 1).

Junction	R_{asymp} (kΩ)	R_{gap} (MΩ)	γ
L1	272	389	7.0×10^{-4}
L2	237	345	6.9×10^{-4}
L3	0.6	–	–
L4	343	259	1.3×10^{-3}
R1	0.6	–	–
R2	70.5	42.4	1.7×10^{-3}
R3	37.9	1.15	3.3×10^{-2}
R4	25.0	0.14	1.8×10^{-1}

Table 8: Connections of the pairs of junctions in the 1-m sample.

Connection	Junctions
Island 1, refrigeration	R1, R2
Island 1, thermometry	R3, R4
Island 2, thermometry	L1, L2
Island 2, floating	L3, L4

The superconducting gap is extracted from the experimental data as in the case of the 20-cm sample. The current through junctions R1 and R2 is measured as a function of the bias voltage at various phonon bath temperatures as shown in Fig. 42. Theoretical curves are fitted according to Eq. (107) with a fitting parameter $\Delta = 250$ μeV. Other parameters are given in Table 7 for the junction R2. The effect of the junction R1 is neglected. There is a good agreement between the fitted curves and the experimental data at temperatures 300 mK and 500 mK. However, the experimental curve at 100 mK phonon bath temperature corresponds to a fitted curve with 180 mK electron temperature.

5.3.2 Thermometer calibration

The temperature calibration data is shown in Fig. 43. The bias current applied through the thermometer junctions is 125 pA in island 1 and 75 pA in island 2. A larger current is used in island 1 because of the elevated noise level. The voltage of the island 1 deviates from the linear fit below 250 mK whereas the voltage of the island 2 follows the linear fit down to 150 mK. The voltages saturate as the bath temperature approaches zero.

Simulated temperature calibration curves are also shown in Fig. 43. The simulated curve of the island 1 saturates at low temperatures, which indicates that the sensitivity may be significantly reduced. The simulation curve of the island 2 does not follow accurately the experimental data. The temperature conversion is again performed using the linear fit.

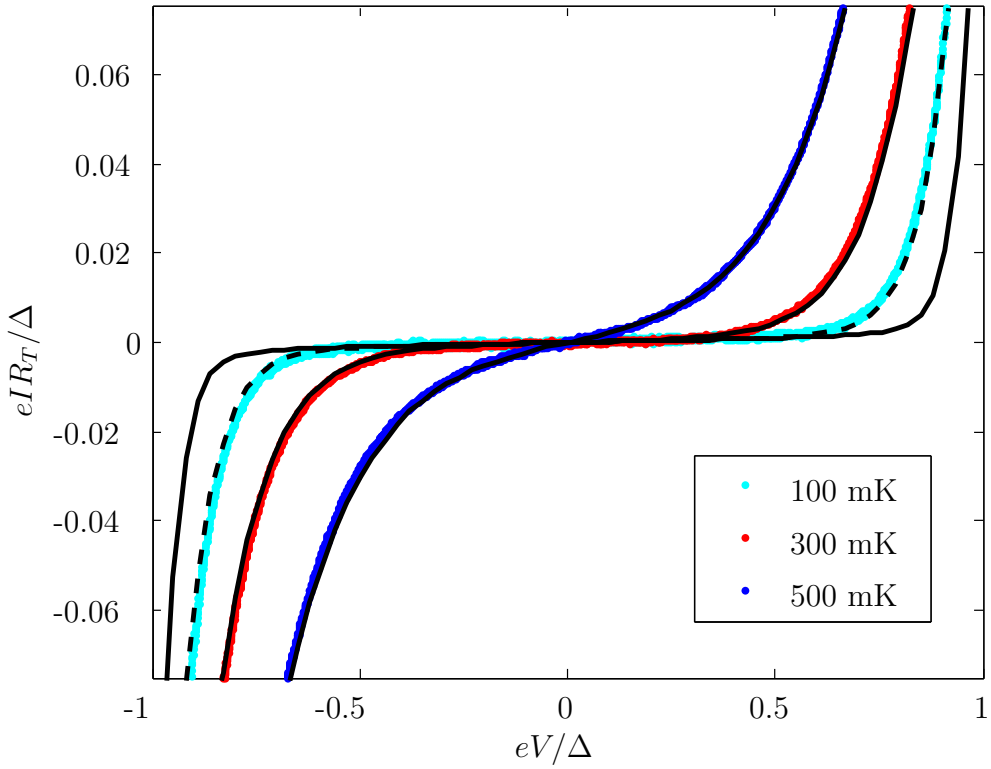

Figure 42: Measured current as a function of voltage through junctions R1 and R2 at various phonon bath temperatures. The junction R2 is a functioning NIS junction, and R1 is shorted. The black solid lines are calculated according to Eq. (107) at electron temperatures equal to the bath temperature by using Δ as a fitting parameter yielding $\Delta = 250$ μeV. At low phonon bath temperatures, the island temperatures saturate. The dashed line is calculated for 180-mK electron temperature.

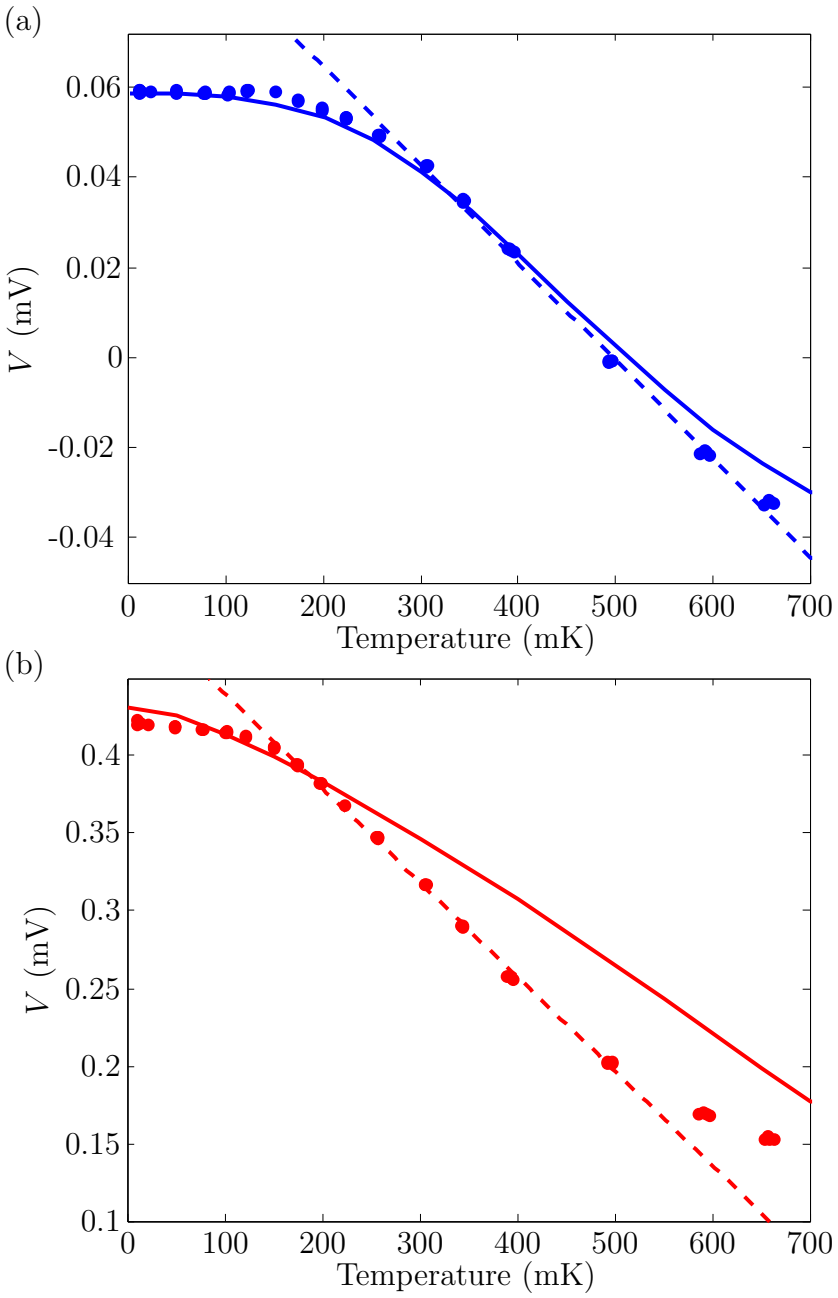

Figure 43: The measured temperature calibration voltages (dots) of (a) island 1 and (b) island 2 as functions of the bath temperature. The simulated curves (solid lines) are calculated numerically as functions of the electron temperature using Eq. (107) with parameters extracted from independent experiments and a constant voltage offset. The dashed lines present linear fits, which are used for the temperature conversion. The thermometer junctions for the island 1 are R1 and R2, and for the island 2 L1 and L2. Their properties are shown in Table 7, and the superconducting gap is $\Delta = 250$ μeV.

5.3.3 Thermometry

Electron temperatures of both islands are presented in Fig. 44 as functions of the refrigerator voltage at island 1. The curves resemble the ones of the 20-cm sample shown in Fig. 38 but the temperature changes are smaller. At high bath temperatures, the islands remain almost at a constant temperature. The temperature of the island 1 at $V = 0$ is approximately 230 mK at a phonon bath temperature of 100 mK. However, the temperature extracted from the fit in Fig. 42 is 180 mK. The difference is assumed to be a consequence of the inaccurate thermometer calibration at low bath temperatures due to the voltage saturation.

The observed temperature changes at the maximum cooling point, $\Delta T_{i,\mathrm{cool}}$, are presented in Fig. 45. The maximum absolute value of the temperature change is less than 2 mK for both islands. Hardly any cooling is observed in the island 2 above the bath temperature of 230 mK although some cooling can be observed in the island 1 up to a temperature of 300 mK. The island temperatures are simulated similarly as in the case of the 20-cm sample, and the simulation parameters are presented in Table 9. The volume of the additional normal metal, ν, is set to be the same as for the 20-cm sample due to similar geometry. The simulated temperature changes of the island 1 are in very good agreement with the experiments at $T_0 > 175$ mK. At low temperatures, the measured absolute values of the temperature changes are slightly smaller than the simulated ones. However, the simulated temperature changes of the island 2 do not follow the experimental data at low temperatures presumably due to the reduced thermometer sensitivity as discussed above.

The ratio of the temperature changes for the cooling data, $\Delta T_{2,\mathrm{cool}}/\Delta T_{1,\mathrm{cool}}$, is also presented in Fig. 45. At high temperatures, the ratio vanishes since no cooling is observed in the island 2. The ratio rises as the bath temperature is reduced below 200 mK. The maximum value of the ratio occurs at temperatures below 50 mK, where it is close to unity. However, the high values of the ratio are most likely partly due to inaccuracy in the thermometry or the calibration of island 1 at low bath temperatures. This also results in a disagreement between the simulations and the experiments.

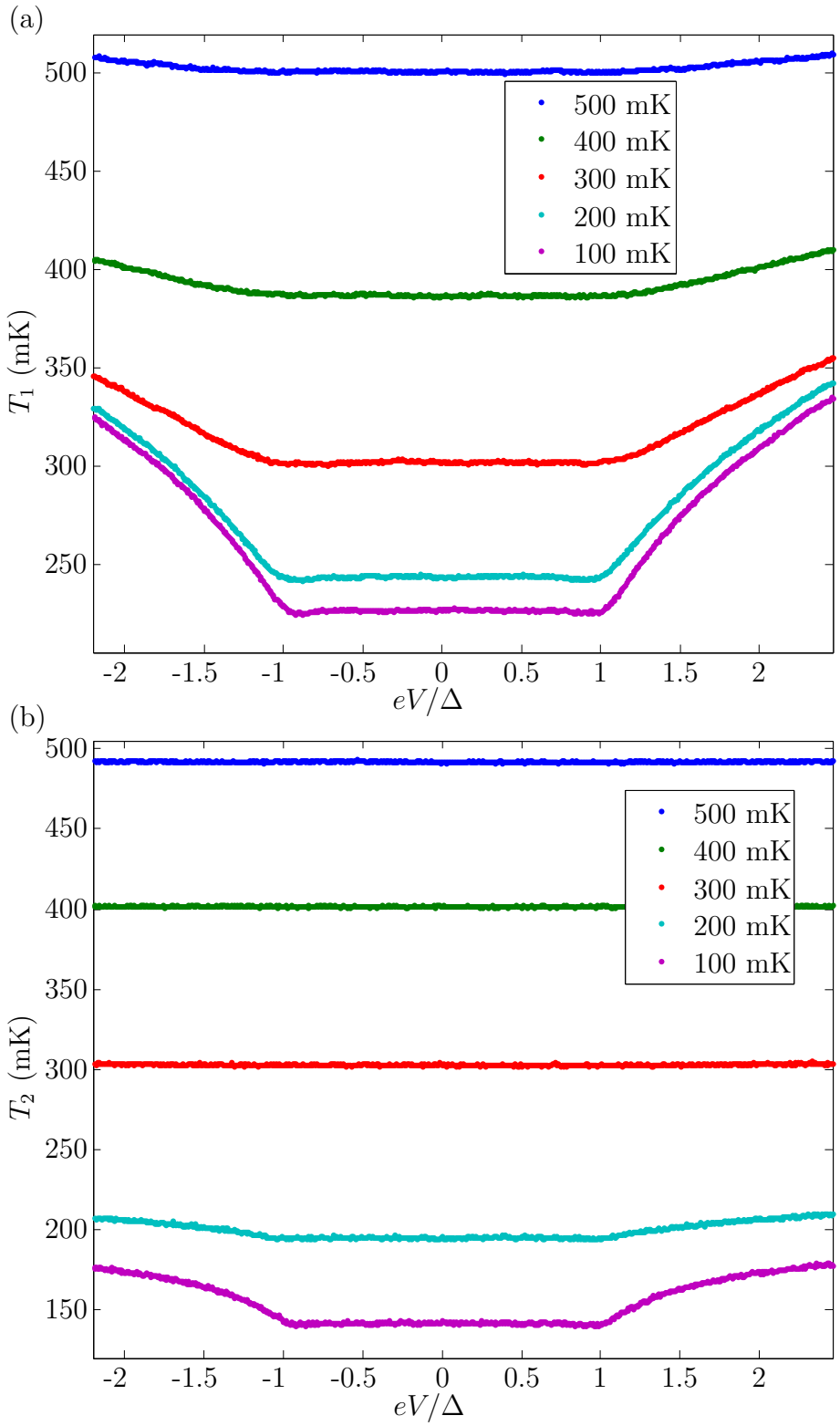

Figure 44: Measured island temperatures (a) T_1 and (b) T_2 at various phonon bath temperatures T_0 as functions of the refrigerator voltage V.

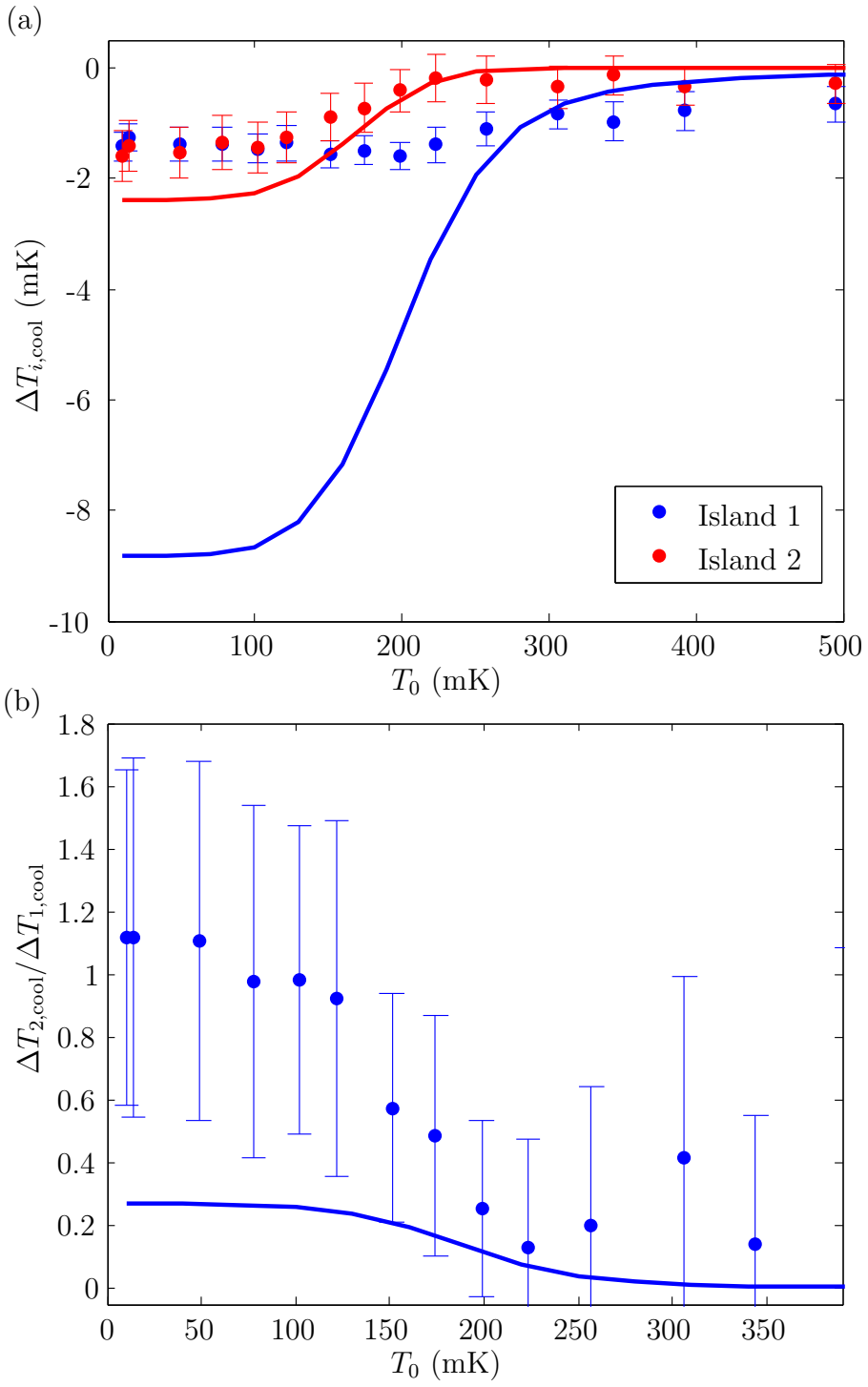

Figure 45: (a) Temperature changes $\Delta T_{1,\mathrm{cool}}$ and $\Delta T_{2,\mathrm{cool}}$ as functions of the bath temperature T_0. (b) The ratio of the temperature changes $\Delta T_{2,\mathrm{cool}}/\Delta T_{1,\mathrm{cool}}$ as a function of T_0. The dots present the experimental data with errorbars obtained from the standard deviation of the temperature data. The solid lines are calculated using the thermal model and the parameters in Table 9.

Table 9: Simulation parameters for the 1-m sample. Here, s, Ω, A_l, and l are fixed by the realised sample geometry, and γ, Δ, R_1, R_2, R_T are measured values independent of the other measurements. We obtain C_l from Comsol simulations, and calculate L_l using Eq. (133). Parameters Σ_{AuPd} and ρ are from Refs. [6] and [38], respectively. We use β, ν and $P_{\mathrm{const},1} = P_{\mathrm{const},2}$ as fitting parameters. The same value of ν is also used for the 20-cm sample fitting.

Quantity	Symbol	Value	Unit
Distance	s	1.0434	m
Inductance per unit length	L_l	4.1×10^{-7}	Hm^{-1}
Capacitance per unit length	C_l	1.5×10^{-10}	Fm^{-1}
Dynes parameter	γ	1.7×10^{-3}	
Island volume	Ω	$3.2 \times 0.25 \times 0.04$	$\mu\mathrm{m}^3$
Island 1 resistance	R_1	75	Ω
Island 2 resistance	R_2	75	Ω
Tunnelling resistance, junction R4	R_T	70.5	$\mathrm{k}\Omega$
Superconducting gap	Δ	250	$\mu\mathrm{eV}$
Material parameter for AuPd	Σ_{AuPd}	3.0×10^9	$\mathrm{WK}^{-5}\mathrm{m}^{-3}$
Constant heat flow to island 1	$P_{\mathrm{const},1}$	14	fW
Constant heat flow to island 2	$P_{\mathrm{const},2}$	14	fW
Backflow coefficient	β	0.02	
Cross section of leads	A_l	200×100	nm^2
Length of leads	l	4	$\mu\mathrm{m}$
Resistivity of leads	ρ	1.5×10^{-8}	$\Omega\mathrm{m}$
Effective volume of extra blocks	ν	$6.5 \times \Omega$	

The island temperatures are also studied in the case of heating, which provides higher signal-to-noise ratios. The temperature changes $\Delta T_{1,\mathrm{heat}}$ and $\Delta T_{2,\mathrm{heat}}$ and their ratio $\Delta T_{2,\mathrm{heat}}/\Delta T_{1,\mathrm{heat}}$ are presented in Fig. 46, where the heater voltage is set to $V_{\mathrm{heat}} = 1.3\Delta/e$. The temperature change of the island 2 vanishes above 250 mK. For $T_0 < 250$ mK, the temperature change starts to increase and it saturates to 18 mK below the bath temperature of 100 mK. The temperature change of island 1 vanishes at $T_0 = 500$ mK. At low bath temperatures, it saturates to 32 mK. The ratio of the temperature changes, $\Delta T_{2,\mathrm{heat}}/\Delta T_{1,\mathrm{heat}}$, obtains its maximum value of 0.55 at low temperatures. The simulated temperature changes of the island 1 follow the experimental results at temperatures above 300 mK. Below that, there is a clear difference between the simulation and the experiments. This is most likely due to

the temperature calibration. The real temperature of the island 1 may be approximately 50 mK lower than the value given by the thermometer calibration at zero voltage as discussed above. There may also be some error in the temperature value at $V = 1.3\Delta/e$. Nevertheless, this error is smaller than the zero voltage value due to the higher temperature. Consequently, $\Delta T_{1,\mathrm{heat}}$ is assumed to obtain higher values than the experimental data in Fig. 46. Therefore, the disagreement between the simulation and the experiments is reasonable.

The island resistance of 75 Ω yields a photonic heat transfer of 94 % of the theoretical maximum according to Fig. 6. The island resistance is calculated using the same normal-metal resistivity as in the 20-cm sample. Unfortunately, the inaccuracies in the thermometry prevent a reliable verification of the high photonic heat conduction. Nevertheless, the results support the model according to which the heat transfer between the islands is mostly photon mediated, and the heat conduction is close to the fundamental upper limit given by quantum mechanics.

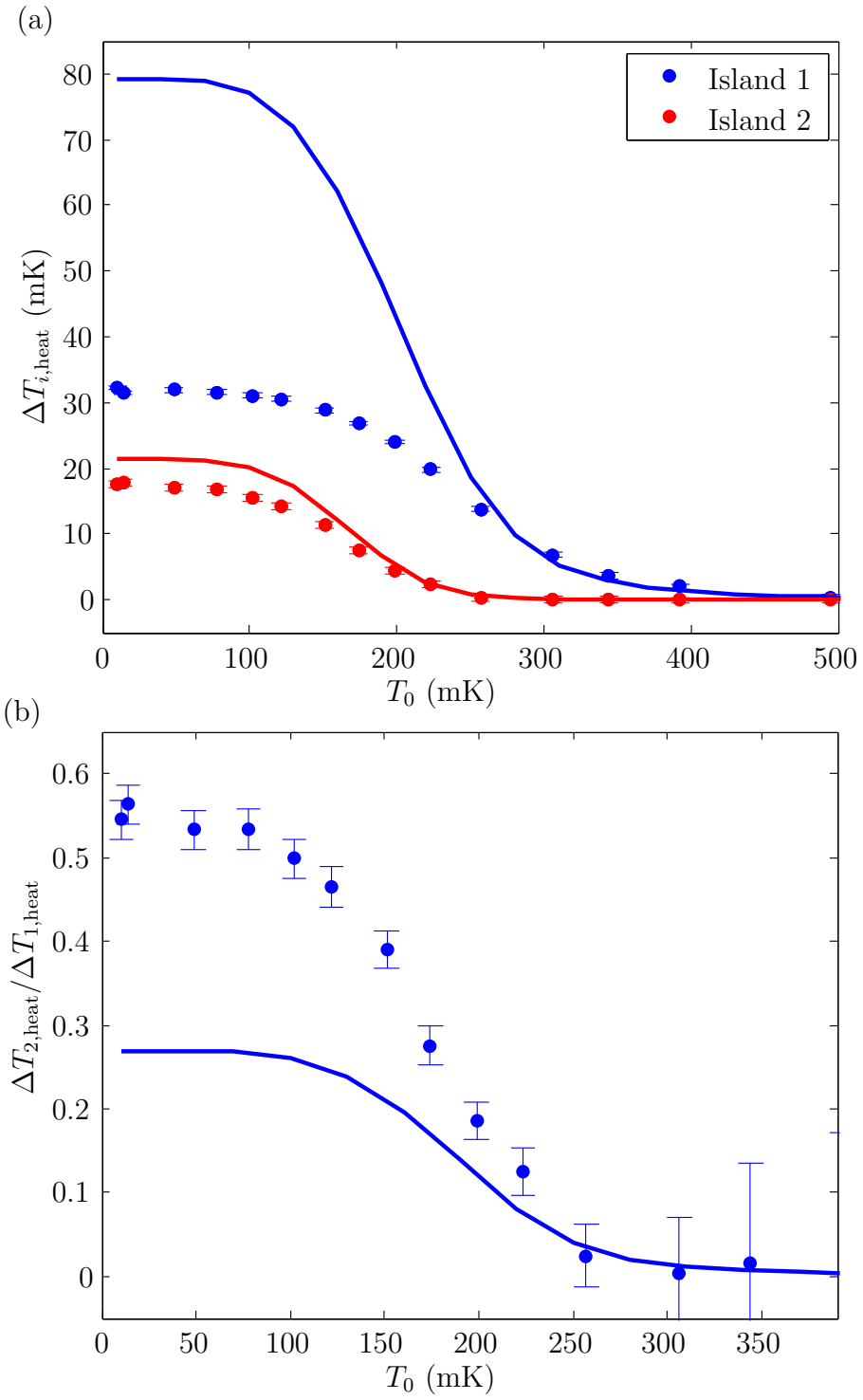

Figure 46: (a) Temperature changes $\Delta T_{1,\mathrm{heat}}$ and $\Delta T_{2,\mathrm{heat}}$ as functions of the bath temperature T_0. (b) The ratio of the temperature changes $\Delta T_{2,\mathrm{heat}}/\Delta T_{1,\mathrm{heat}}$ as a function of T_0. Experimental data is presented by dots, and the solid lines are fitted curves. The errorbars are obtained from the standard deviation of the temperature data. The parameters of the fitted curves are presented in Table 9.

6 Conclusions

The heat conduction through a single channel is fundamentally limited by quantum mechanics [1]. In this thesis, the heat conduction between two normal-metal resistors terminating a superconducting microwave transmission line at different ends was studied experimentally. For the first time, the quantum-limited heat conduction was studied at macroscopic length scales. The theoretical basis for the heat conduction experiments was also reviewed.

Control samples without the resistors were fabricated out of Nb and measured at a temperature of 4 K. The quality factors of these resonators were observed to be of the order of 10^4 implying weak energy dissipation. The observed high intrinsic quality factor of the transmission line enables effective photonic heat transfer between the resistors it connects in the actual sample. Furthermore, different loaded quality factors were obtained by varying the coupling capacitance. In addition, the environment of the resonator was observed to affect the quality factor. Nevertheless, even the lowest quality factors observed were high enough for the dissipation in the transmission line to be negligible in the heat conduction experiments.

The samples for the heat conduction experiments were fabricated out of Al and measured at sub-kelvin temperatures in a dilution refrigerator. The heat conduction between two normal-metal islands was measured with the help of NIS thermometry and temperature control. The temperatures of the normal-metal islands saturated at low temperatures due to heat leaks, which prevented reliable measurements below 150 mK. In addition, the accuracy of the thermometry was reduced due to saturation. Despite these sources of uncertainty, the experimental results support the theoretical model. Our conclusion is that photon-dominated heat conduction between the normal-metal islands was observed over distances of 20 cm and 1 m. Furthermore, the photonic heat conductance was close to the fundamental upper limit, the quantum of thermal conductance, according to the theoretical model.

The experimental results confirm the opportunity to realise temperature control of superconducting qubits over large distances. Both cooling and heating are feasible. The temperature control of the superconducting qubits is vital for their ultimate operation. In addition, the studied system may find other applications in remote cooling of very sensitive devices, such as measurement instruments operating at sub-kelvin temperatures.

This thesis contributed to further understanding the heat transfer mechanisms at sub-kelvin temperatures. However, more research is needed in studying the thermal conductance at the quantum limit in order to realise the full potential of the heat transfer applications in quantum nanoelectronics. The results presented in this thesis need to be verified with more accurate measurements at very low temperatures.

References

[1] J. B. Pendry, "Quantum limits to the flow of information and entropy," Journal of Physics A: Mathematical and General 16, 2161 (1983)

[2] K. Schwab, E. A. Henriksen, J. M. Worlock, M. L. Roukes, "Measurement of the quantum of thermal conductance," Nature 404, 974 (2000)

[3] M. Meschke, W. Guichard, J. P. Pekola, "Single-mode heat conduction by photons." Nature 444, 187 (2006)

[4] A. V. Timofeev, M. Helle, M. Meschke, M. Möttönen, J. P. Pekola, "Electronic Refrigeration at the Quantum Limit," Physical Review Letters 102, 200801 (2009)

[5] S. Jezouin, F. D. Parmentier, A. Anthore, U. Gennser, A. Cavanna, Y. Jin, F. Pierre, "Quantum Limit of Heat Flow Across a Single Electronic Channel," Science 342, 601 (2013)

[6] F. Giazotto, T. T. Heikkilä, A. Luukanen, A. M. Savin, J. P. Pekola, "Opportunities for mesoscopics in thermometry and refrigeration: Physics and applications," Reviews of Modern Physics 78, 217 (2006)

[7] M. H. Devoret, R. J. Schoelkopf, "Superconducting Circuits for Quantum Information: An Outlook," Science 339, 1169 (2013)

[8] E. L. Wolf, *Quantum Nanoelectronics: An Introduction to Electronic Nanotechnology and Quantum Computing*, Wiley-VCH, Weinheim (2009)

[9] T. D. Ladd, F. Jelezko, R. Laflamme, Y. Nakamura, C. Monroe, J. L. O'Brien, "Quantum computers," Nature 464, 45 (2010)

[10] P. W. Shor, "Algorithms for Quantum Computation: Discrete Logarithms and Factoring," in "Proceedings of the 35th Annual Symposium on Foundations of Computer Science," SFCS '94, IEEE Computer Society, Washington, DC, USA, 124–134 (1994)

[11] J. Clarke, F. K. Wilhelm, "Superconducting quantum bits," Nature 453, 1031 (2008)

[12] R. J. Schoelkopf, S. M. Girvin, "Wiring up quantum systems," Nature 451, 664 (2008)

[13] P. J. Jones, J. A. M. Huhtamäki, K. Y. Tan, M. Möttönen, "Single-photon heat conduction in electrical circuits," Physical Review B 85, 075413 (2012)

[14] P. J. Jones, J. A. M. Huhtamäki, M. Partanen, K. Y. Tan, M. Möttönen, "Tunable single-photon heat conduction in electrical circuits," Physical Review B 86, 035313 (2012)

[15] P. J. Jones, J. A. M. Huhtamäki, J. Salmilehto, K. Y. Tan, M. Möttönen, "Tunable electromagnetic environment for superconducting quantum bits," Scientific Reports 3 (2013)

[16] P. J. Jones, J. Salmilehto, M. Möttönen, "Highly Controllable Qubit-Bath Coupling Based on a Sequence of Resonators," Journal of Low Temperature Physics 173, 152 (2013)

[17] J. Kokkala, *Quantum computing with itinerant microwave photons*, Master's thesis, Aalto University (2013)

[18] L. G. C. Rego, G. Kirczenow, "Fractional exclusion statistics and the universal quantum of thermal conductance: A unifying approach," Physical Review B 59, 13080 (1999)

[19] I. Bahl, *Lumped Elements for RF and Microwave Circuits*, Artech House, Norwood (2003)

[20] D. Pozar, *Microwave Engineering*, 4th ed., John Wiley & Sons, Hoboken (2011)

[21] B. Yurke, J. S. Denker, "Quantum network theory," Physical Review A 29, 1419 (1984)

[22] J. B. Johnson, "Thermal Agitation of Electricity in Conductors," Physical Review 32, 97 (1928)

[23] H. Nyquist, "Thermal Agitation of Electric Charge in Conductors," Physical Review 32, 110 (1928)

[24] D. R. Schmidt, R. J. Schoelkopf, A. N. Cleland, "Photon-Mediated Thermal Relaxation of Electrons in Nanostructures," Physical Review Letters 93, 045901 (2004)

[25] J. Bardeen, L. N. Cooper, J. R. Schrieffer, "Theory of Superconductivity," Physical Review 108, 1175 (1957)

[26] M. Tinkham, *Introduction to superconductivity*, 2nd ed., Dover Publications, Mineola (2004)

[27] R. C. Dynes, J. P. Garno, G. B. Hertel, T. P. Orlando, "Tunneling Study of Superconductivity near the Metal-Insulator Transition," Physical Review Letters 53, 2437 (1984)

[28] M. M. Leivo, J. P. Pekola, "Efficient Peltier refrigeration by a pair of normal metal/insulator/superconductor junctions," Applied Physics Letters 68, 1996 (1996)

[29] A. Kemppinen, *Tunnel junction devices for quantum metrology*, Ph.D. thesis, Helsinki University of Technology (2009)

[30] H. Grabert, M. H. Devoret, eds., *Single Charge Tunneling: Coulomb Blockade Phenomena In Nanostructures*, Plenum Press, New York (1992)

[31] J. P. Pekola, V. F. Maisi, Kafanov, N. Chekurov, A. Kemppinen, Y. A. Pashkin, O.-P. Saira, M. Möttönen, J. S. Tsai, "Environment-Assisted Tunneling as an Origin of the Dynes Density of States," Physical Review Letters 105, 026803 (2010)

[32] F. Giazotto, F. S. Bergeret, "Thermal rectification of electrons in hybrid normal metal-superconductor nanojunctions," Applied Physics Letters 103 (2013)

[33] F. Pobell, *Matter and Methods at Low Temperatures*, Springer, Berlin (2007)

[34] E. V. Bezuglyi, V. Vinokur, "Heat Transport in Proximity Structures," Physical Review Letters 91, 137002 (2003)

[35] A. V. Timofeev, C. P. García, N. B. Kopnin, A. M. Savin, M. Meschke, F. Giazotto, J. P. Pekola, "Recombination-Limited Energy Relaxation in a Bardeen-Cooper-Schrieffer Superconductor," Physical Review Letters 102, 017003 (2009)

[36] J. T. Muhonen, M. Meschke, J. P. Pekola, "Micrometre-scale refrigerators," Reports on Progress in Physics 75, 046501 (2012)

[37] J. Muhonen, *Cooling and heat transport in low dimensional phonon systems, superconductors and silicon*, Ph.D. thesis, Aalto University (2012)

[38] A. V. Timofeev, *Tunnel junctions as detectors of noise and energy relaxation in superconducting circuits*, Ph.D. thesis, Helsinki University of Technology (2009)

[39] M. Göppl, A. Fragner, M. Baur, R. Bianchetti, S. Filipp, J. M. Fink, P. J. Leek, G. Puebla, L. Steffen, A. Wallraff, "Coplanar waveguide resonators for circuit quantum electrodynamics," Journal of Applied Physics 104, 113904 (2008)

[40] I. Wolff, *Coplanar Microwave Integrated Circuits*, John Wiley & Sons, Hoboken (2006)

[41] R. N. Simons, *Coplanar Waveguide Circuits, Components, and Systems*, John Wiley & Sons, New York (2001)

[42] S. Gevorgian, L. J. P. Linnér, E. L. Kollberg, "CAD Models for Shielded Multilayered CPW," IEEE Transactions on Microwave Theory and Techniques 43, 772 (1995)

[43] K. Watanabe, K. Yoshida, T. Aoki, S. Kohjiro, "Kinetic Inductance of Superconducting Coplanar Waveguides," Japanese Journal of Applied Physics 33, 5708 (1994)

[44] W. Rauch, E. Gornik, G. Sölkner, A. A. Valenzuela, F. Fox, H. Behner, "Microwave properties of thin films studied with coplanar transmission line resonators," Journal of Applied Physics 73, 1866 (1993)

[45] J. Gao, J. Zmuidzinas, B. Mazin, P. Day, H. Leduc, "Experimental study of $YBa_2Cu_3O_{7-x}$ the kinetic inductance fraction of superconducting coplanar waveguide," Nuclear Instruments and Methods in Physics Research Section A: Accelerators, Spectrometers, Detectors and Associated Equipment 559, 585 (2006)

[46] B. Ho Eom, P. K. Day, H. G. LeDuc, J. Zmuidzinas, "A wideband, low-noise superconducting amplifier with high dynamic range," Nature Physics 8, 623 (2012)

[47] H. Su, Y. Wang, F. Huang, M. Lancaster, "Superconducting Delay Lines," Journal of Superconductivity and Novel Magnetism 21, 7 (2008)

[48] P. J. Petersan, S. M. Anlage, "Measurement of resonant frequency and quality factor of microwave resonators: Comparison of methods," Journal of Applied Physics 84 (1998)

[49] Z. Ma, *RF properties of high-temperature superconducting materials*, Ph.D. thesis, Stanford University (1995)

[50] D. R. Lide, ed., *CRC Handbook of Chemistry and Physics*, 84th ed., CRC Press, Boca Raton (2004)

A Classical reflection and transmission coefficients

In this appendix, classical reflection and transmission coefficients are derived for two different systems. The systems are analogous and, therefore, the results are similar. An alternative method for calculating the coefficients is presented in Sec. 2.6.

Two connected transmission lines

When two transmission lines with different characteristic impedances are connected, only part of the incoming wave is transmitted while the rest is reflected. The incoming voltage and current waves with a single frequency ω are denoted by $V_{1,R}$ and $I_{1,R}$, the reflected waves by $V_{1,L}$ and $I_{1,L}$, and the transmitted waves by $V_{2,R}$ and $I_{2,R}$. There are no waves moving to the left in transmission line 2, $V_{2,L} = 0, I_{2,L} = 0$. We set the coordinates such that the junction is at position $x = 0$. A schematic presentation of the system is shown in Fig. A.1.

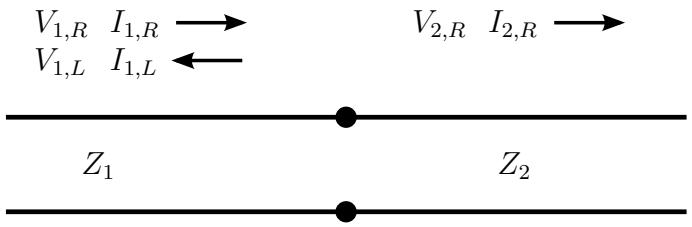

Figure A.1: Two connected transmission lines with different characteristic impedances Z_1 and Z_2. The voltage and current wave directions are indicated with arrows.

The voltage must be equal on both sides of the junction. In addition, the current must be conserved. Therefore, we obtain two equations:

$$V_{1,L} + V_{1,R} = V_{2,R}, \tag{A.1}$$

$$-I_{1,L} + I_{1,R} = I_{2,R}. \tag{A.2}$$

Since the current and voltage are related by $I_{\alpha,\beta} = V_{\alpha,\beta}/Z_\alpha$, where $\alpha = 1, 2$,

and $\beta = L, R$, we obtain the voltage reflection coefficient

$$\Gamma_V = \frac{V_{1,L}}{V_{1,R}} = \frac{Z_2 - Z_1}{Z_2 + Z_1}. \tag{A.3}$$

Similarly, we obtain the voltage transmission coefficient

$$T_V = \frac{V_{2,R}}{V_{1,R}} = \frac{2Z_2}{Z_2 + Z_1}. \tag{A.4}$$

These coefficients are related by

$$T_V = 1 + \Gamma_V. \tag{A.5}$$

The average in-coming power can be calculated from the voltage amplitude as [20]

$$P_{1,R} = \frac{1}{2}\mathrm{Re}(V_{1,R} I_{1,R}^*) = \frac{1}{2}\frac{|V_{1,R}|^2}{Z_1}. \tag{A.6}$$

Here, we have assumed that the line is lossless, and hence Z_1 is real. The transmitted and reflected powers are calculate similarly. Thus, the power reflection and transmission coefficients can be obtained

$$\Gamma_P = \frac{P_{1,L}}{P_{1,R}} = \left(\frac{Z_2 - Z_1}{Z_2 + Z_1}\right)^2 = \Gamma_V^2, \tag{A.7}$$

$$T_P = \frac{P_{2,R}}{P_{1,R}} = \frac{4Z_2 Z_1}{(Z_2 + Z_1)^2} = \frac{Z_1}{Z_2} T_V^2. \tag{A.8}$$

Due to the energy conservation, we have

$$\Gamma_P + T_P = 1. \tag{A.9}$$

Transmission line terminated by an impedance

Let us study the reflection caused by an impedance at the end of a transmission line. The system is shown in Fig. A.2. We set the impedance to position $x = 0$.

The voltage and current at the impedance are given by

$$V = V_L + V_R, \tag{A.10}$$

$$I = I_R - I_L = \frac{V_R - V_L}{Z_0}. \tag{A.11}$$

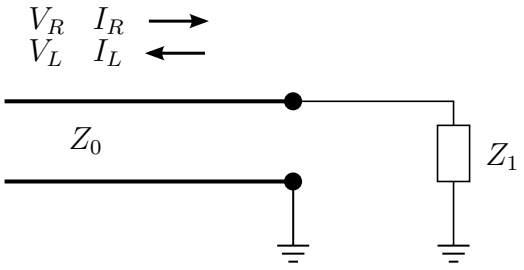

Figure A.2: Transmission line terminated by an impedance Z_1.

These are related to impedance Z_1 by

$$Z_1 = \frac{V}{I} = \frac{V_L + V_R}{V_R - V_L} Z_0. \tag{A.12}$$

From this we obtain the voltage reflection coefficient

$$\Gamma_V = \frac{V_L}{V_R} = \frac{Z_1 - Z_0}{Z_1 + Z_0}, \tag{A.13}$$

which agrees with Eq. (A.3). The power reflection coefficient is again given by

$$\Gamma_P = \Gamma_V^2. \tag{A.14}$$